Università degli Studi di Padova
Dipartimento di Ingegneria Industriale

Corso di Laurea Magistrale in Ingegneria dell'Energia Elettrica

Tesi di laurea magistrale

Analysis of the integration of two DFIGs with rotating power electronics for wind energy application

Analisi sull'integrazione di due generatori DFIG con elettronica di potenza su rotore per generazione eolica

Candidato:
Federico Mizzon
Matricola 1081492

Relatore:
Prof. Nicola Bianchi

Correlatore:
Ph.D. Ing. Luca Peretti

Anno Accademico 2015/2016

Abstract

This thesis describes the analysis of a new topology of double-fed induction generator for wind power applications, where two generators are connected in parallel sharing the same mechanical shaft, and both contributing to the power generation towards the grid.

This thesis topic is form KTH of Stockholm and it is part of Elforsk project V-308 "Brushless Wind Power Generator for Limited Speed Range". Responsable for this project is Prof. Chandur Sadarangani. The analysis work was carried out at ABB Corporate Research Center of Västerås (Sweden). Supervisor of this thesis work in ABB is Ph.D. Ing. Luca Peretti.

Since the analyzed topology is rather unknown, a preliminary study on the basic machine design rules is performed. For example, the optimal number of pole pairs for the two machines is sought. As a consequence, the electrical and mechanical power flows from the two machines is analyzed, considering the available range of slip. After the selection of a reasonable machine size and pole pairs number, the dynamic model of the system is built and a control strategy is defined. Simulation results prove that the system can generate power in a controlled way.

Sommario

Questa tesi descrive l'analisi effettuata su una nuova topologia di doubly-fed-induction-generator per la generazione di potenza elettrica da eolico, nella quale due generatori sono connessi in parallelo condividendo lo stesso albero, entrambi contribuendo alla generazione di potenza verso la rete elettrica.

Tale argomento di tesi provene dal KTH di Stoccolma ed è parte del progetto Elforsk V-308 "Brushless Wind Power Generator for Limited Speed Range". Responsabile di tale progetto è il Prof. Chandur Sadarangani. Il lavoro di analisi è stato svolto presso l'ABB Corporate Research Center di Västerås (Svezia). Supervisore e correlatore a questa tesi presso ABB è il Dott. Ing. Luca Peretti.

Uno studio preliminare sulle regole di dimensionamento è stato effettuato in quanto tale topologia risulta essere ancora abbastanza sconosciuta. È stato ricercato il numero ottimale di coppie polari per le due macchine e di conseguanza sono stati valutati i flussi di potenza elettrica e meccanica, tenendo conto dei valori di scorrimento utilizzabili. Dopo la definizione di valori plausibili di coppie polari e dimensioni di macchina, è stato costruito un modello dinamico della machina stessa ed è stata definita una strategia di controllo. Le simulazioni provano che tale sistema può generare potenza elettrica in maniera controllata.

Acknowledgment

"IO HO
QUEL CHE
HO DONATO."
G. D'Annunzio

The present Master Thesis is about my job I conducted to ABB Corporate Research Center of Västerås, in Sweden. I have successfully finished my job thanks to lots of people who helped me. I would thank Prof. Nicola Bianchi for helping me to find out the thesis topic and teaching electric machine. I am grateful to my supervisor in ABB CRC, Ph.D. Ing. Luca Peretti for giving me the chance to face an interesting topic about electric machine and drives and for his valuable and constant scientific guidance while i was there at CRC of Västerås. I would thank all the people of ABB Corporate Research Center of Västerås who shared their time whit me; I felt like as I was at home. Especially I would like to thank Ing. Giovanni Zanuso for his advices and for lending me one of his bicycles and Ph.D. Pedro Rodriguez for suggesting me the proper machine parameters. I even would thank Giulia who helped me to improve my English before my leaving for Sweden.

Ora i ringraziamenti in Italiano...
Un enorme grazie alla mia famiglia per il sostegno che mi ha dato durante il percorso di studi: a mia madre, mio padre e mia nonna per il sostegno e gli insegnamenti, e specialmente ai miei genitori per il "pane" quotidiano di tutti questi anni. "Germoglia un grazie" per il fondamentale supporto dell'Ing. Francesco Longato e della sua famiglia, per avermi aiutato a capire qual'era il percorso più adatto a me. Infine un profondo e sentito ringraziemento va alla Scuola delle Nove Armonie di Conselve a cui sarò sempre grato; al Maestro Nicola e agli Istruttori Marco, Lara e Simone. La Scuola è sempre stata fonte di grandi insegnamenti ed è un orgoglio ed uno onore farvi parte.

Ringrazio inoltre tutti i miei amici da Conselve, chi è ancora a Conselve e anche chi è migrato altrove, per il loro supporto e per il tempo passato assieme. Un grande grazie anche agli amici conosciuti durante il percorso in università, specialmente alla compagnia di Rubbio. Infine un grazie a tutti gli altri amici che non cito per non dilungare troppo i ringraziamenti.

Federico Mizzon
Conselve (Padova), Italy
September 2016

Contents

List of Figures

List of Tables

Chapter 1

INTRODUCTION

1.1 Purpose and scope

The purpose of this work is to analyze a special topology for wind power generation which is known as Brushless Doubly-Fed Induction Generator (BDFIG) with rotating power electronic converters. The topology consists of two doubly-fed induction machines whose rotors are electrically connected with each other through two power electronic converters, while the stators of the two machines are connected to the grid in a parallel fashion. The two stators are therefore operating at the same frequency. The rotors of the machines are also mechanically connected through the same shaft, therefore rotating at a common mechanical speed. However, the two rotors can have different slip frequency if different pole pair combinations are chosen for the machines.

A second purpose of this work is to employ the control principles of a conventional doubly-fed induction machine (DFIG) with slip rings to this topology case. In the conventional DFIG case, the majority of the power flows through the stator terminals of the machine, while the remaining power flows through the power electronic converter connected to the rotor. However, in this topology, the converter is not connected to the grid, but to a second converter which shares the DC bus with the first. The second converter is then connected to the rotor of a second DFIG, which handles the slip power from the first machine. The slip power is then fed to the grid in an electrical manner via stator of the second DFIG.

Depending on the number of pole-pairs, one of the two DFIGs will handle most of the active power while the second DFIG will handle the remaining slip power. Power electronics is used to control the speed and the power factor of the machine at the stator terminals.

The scope of the report then is to describe the operating regions of the proposed topology. A theoretical analysis is firstly carried out, and conditions and considerations on the machine design are described. The relation between the dimensioning parameters and the power through the different sections of the machine are analyzed, and the most convenient dimensions are computed. It is worth underlining that the aim of the analysis is to find two feasible machine dimensions. Therefore, the chosen design criteria uses information of already-available DFIG machines in order to define a feasible system. This brings some limitations in the analysis.

On a second stage, the description of the Simulink model of the system with its full closed-loop control is performed. The simulations are carried out for a wind generator of 5 MW, which is a standard value used for the analysis of wind generation cases in offshore plants. The interest in offshore plants is due to the fact that they allow the exploitation of

stronger and regular winds and have a lower visual impact [1].

The analysis in this report has been performed using Matlab® and its dynamic simulation tool Simulink®. A Matlab® code is used for the evaluation explained in the chapter 3. Simulink is used for the machine modelling described in chapter 4, and it is used for the control simulations shown in Chapter 5.

1.2 Abbreviations and definitions

The abbreviations, the definitions, the subscripts and the superscripts are reported in Tab. 1.1, Tab. 1.2, Tab. 1.3 and Tab. 1.4.

Tab. 1.1: General abbreviations.

FOC	field-oriented control
PWM	pulse-width modulation
DFIG	doubly-fed induction generator
D-DFIG	double-doubly-fed induction generator
A/D	analog to digital converter
PLL	phase-locked loop

Tab. 1.2: General definitions.

abc, $\alpha\beta$	stator-fixed reference frames
dq	rotating reference frame
xy	rotating reference frame used by the control algorithm
$\boldsymbol{T}_{abc\rightarrow\alpha\beta}$, $\boldsymbol{T}_{\alpha\beta\rightarrow abc}$	transformation from the abc to the $\alpha\beta$ reference frame and viceversa
$\boldsymbol{T}_{\alpha\beta\rightarrow xy}$, $\boldsymbol{T}_{xy\rightarrow\alpha\beta}$	transformation from the $\alpha\beta$ to the xy reference frame and viceversa
v	voltage, V
i	current, A
φ	flux linkage, Wb/m^2
r	resistance, Ω
L	inductance, H
M	mutual inductance between rotor and stator, H
ω	angular speed of the voltage applied to the stator, $\frac{rad}{s}$
ω_m	angular speed of the rotor, $\frac{rad}{s}$
p	pole pairs
rp	pole ratio
s	slip
N	rotor speed
V	magnitude of the voltage applied to the stator, V
P	active power, W
Q	reactive power, Var

Tab. 1.3: General subscripts.

d	d-component in dq form
q	q-component in dq form
x	x-component in xy form
y	y-component in xy form
l	leakage component of the inductance
s	stator of the induction machine
r	rotor of the induction machine
0	reference to the synchronous operating point
n	nominal value
1,2	reference to the induction machine in the topology
dc	direct current or voltage
$cut-in$	values for the cut-in speed

Tab. 1.4: General superscripts.

r	rated values
x	generic reference
$'$	rotor quantities referred to the stator side

1.3 Structure

This report has the following structure.

Chapter 1 (this chapter) describes the report topic, the report structure and the abbreviations and definitions used in the further text.

Chapter 2 describes the standard topology of a DFIG, its advantages and drawbacks and some alternative topologies proposed in order to solve the conventional topology issues.

Chapter 3 performs the analytical evaluation of the D-DFIG topology. The aim of the theoretical evaluation is to reach an understanding of the parameter ranges for a good machine dimensioning.

Chapter 4 describes the Simulink model of the D-DFIG and how its blocks are composed, starting from the blocks of a standard DFIG model. Eventually, the control strategy for the proposed topology is defined.

Chapter 5 shows and discusses some simulation results of the Simulink model.

Chapter 6 reports some conclusive remarks on the work.

Chapter 7 describes the possible future works related the proposed topology, and possible variations of the original idea.

Chapter 2

INTRODUCTION ON THE DFIG CONFIGURATION

The topology of D-DFIG presented in this work is developed to improve the conventional DFIG systems used in the wind generation business. For this purpose, a short introduction of the DFIG is hereby reported, describing the electro-magnetic interaction between stator and rotor, reaching a formulation that describe the exchange of power in the stator and rotor. From this starting point, a list of the advantages and drawbacks of such solutions is given.

2.1 Analysis of the DFIG

In a conventional DFIG installation for wind power generation, the rotor windings are connected by some carbon brushes to an external inverter, which uses the grid as power supply. The aim of the inverter is the control of the current in the rotor windings, and thus the rotor flux control. A schematic of such topology is shown in Fig. 2.1. In this configuration, the rotor control uses the rotor currents (their frequency and magnitude) in order to control the active and reactive power delivered to the grid.

Starting from the voltage balance equations of a wound rotor induction machine in the rotating dq reference frame (using the Park-Clark transformations [2], [3]), it is possible to extract a relation between the stator active power P_s and the rotor active power P_r. The voltage stator equations in the dq reference frame are the following:

$$\begin{aligned} v_{ds} &= r_s i_{ds} + \frac{d}{dt}\varphi_{ds} - \omega\varphi_{qs} \\ v_{qs} &= r_s i_{qs} + \frac{d}{dt}\varphi_{qs} + \omega\varphi_{ds} \end{aligned} \tag{2.1}$$

The voltage rotor equations in the dq reference frame are the following:

$$\begin{aligned} v'_{dr} &= r'_r i'_{dr} + \frac{d}{dt}\varphi'_{dr} - s\omega\varphi'_{qr} \\ v'_{qr} &= r'_r i'_{qr} + \frac{d}{dt}\varphi'_{qr} + s\omega\varphi'_{dr} \end{aligned} \tag{2.2}$$

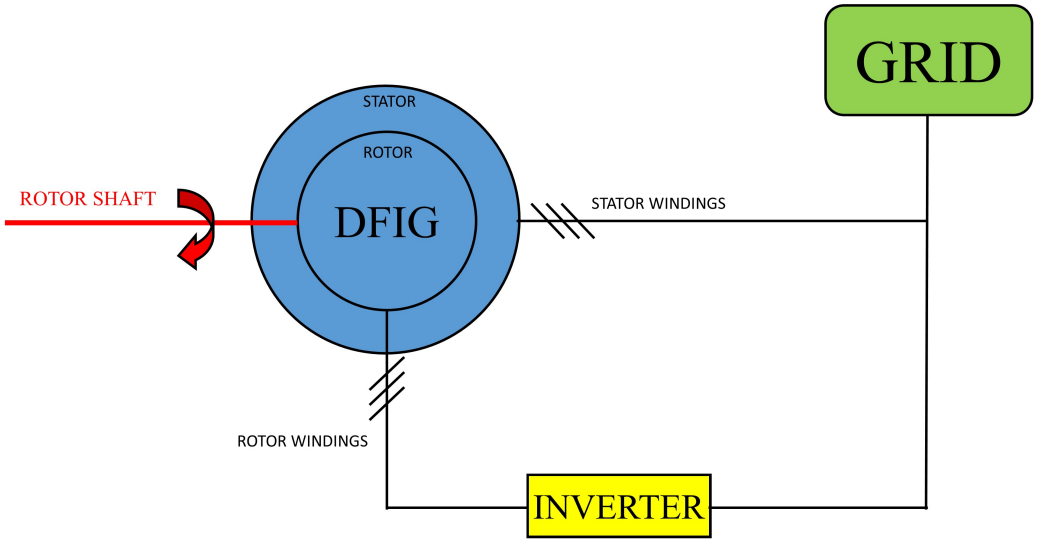

Fig. 2.1: Schematic representation of the standard DFIG configuration.

The equations describing the flux linkage as function of the currents are:

$$\begin{array}{rcl} \varphi_{ds} & = & L_s i_{ds} + M' i'_{dr} \\ \varphi_{qs} & = & L_s i_{qs} + M' i'_{qr} \\ \varphi'_{dr} & = & L'_r i'_{dr} + M' i_{ds} \\ \varphi'_{qr} & = & L'_r i'_{qr} + M' i_{qs} \end{array} \tag{2.3}$$

The slip of the machine, with p being the pole pair number of a machine, is defined as:

$$s = \frac{\omega - p\omega_m}{\omega} \tag{2.4}$$

with ω_m the mechanical angular speed of the rotor. The stator and rotor inductances are defined as:

$$\begin{array}{rcl} L_s & = & L_{ls} + M' \\ L'_r & = & L'_{lr} + M' \end{array} \tag{2.5}$$

with L'_{lr} and L_{ls} being the leakage inductances of the DFIG stator and rotor windings.

Considering a steady-state condition in a lossless system, the voltage equations are simplified in according with (2.1), (2.2), (2.3) and (2.4):

$$\begin{array}{rcl} v_{ds} & = & -\omega\varphi_{qs} = -\omega L_s i_{qs} - \omega M' i'_{qr} \\ v_{qs} & = & \omega\varphi_{ds} = \omega L_s i_{ds} + \omega M' i'_{dr} \end{array} \tag{2.6}$$

and

$$\begin{array}{rcl} v'_{dr} & = & -s\omega\varphi'_{qr} = -s\omega L'_r i'_{qr} - s\omega M' i_{qs} \\ v'_{qr} & = & s\omega\varphi'_{dr} = s\omega L'_r i'_{dr} + s\omega M' i_{ds} \end{array} \tag{2.7}$$

The convention for the stator power that flows out of the stator is:

$$P_s + jQ_s = (v_{ds} + jv_{qs})(-i_{ds} + ji_{qs}) \tag{2.8}$$

while the equation for the rotor power flowing in the rotor is:

$$P_r + jQ_r = (v'_{dr} + jv'_{qr})(i'_{dr} - ji'_{qr}) \tag{2.9}$$

Through the equations (2.6), (2.7), (2.8) and (2.9), it is possible define the relation between P_s and P_r [3]:

$$P_r = sP_s \tag{2.10}$$

Introducing the shaft input power P_m, for the energy conservation principle in lossless condition (and in agreement with the rotor electric power sign, which is positive if it flows inside the rotor winding), it follows:

$$P_r + P_m = P_s \tag{2.11}$$

Therefore, it is possible to write the equations of P_s and P_r starting from P_m and s, in according to the power flow of Fig. 2.2):

$$P_s = \frac{P_m}{1-s} \tag{2.12}$$

$$P_r = \frac{sP_m}{1-s} \tag{2.13}$$

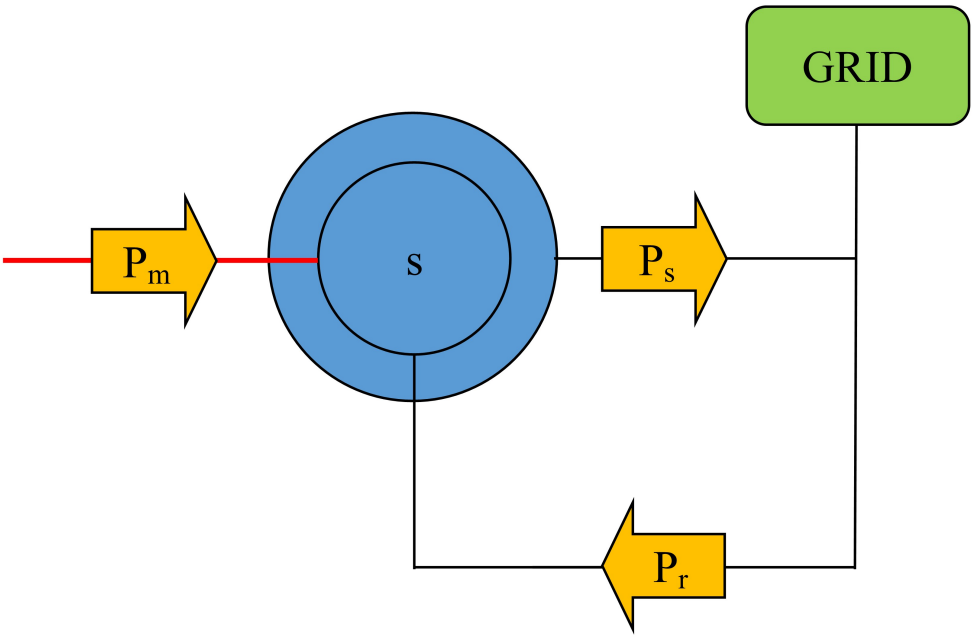

Fig. 2.2: Power flows in the standard DFIG configuration.

2.2 Advantages and drawbacks of the conventional DFIG configuration

A clear advantage of the DFIG configuration is the possibility to operate at variable speed with a direct connection of the stator windings to the grid. Thanks to the range of available slips in the machine, it is possible to operate at different speed values and avoid the use of power electronics between the stator connection and the grid. The range of the slips is usually located in an interval of ± 0.3: this means that a DFIG connected to a $50Hz$ grid, with a number of pole pairs $p = 3$ and a range of slips of ± 0.3 is able to operate in the range of mechanical speeds of $700 : 1300$ rpm.

Another importance advantage resides in the size of the power electronic devices in the converter. In accordance to the equation (2.10), with a typical slip range of ± 0.3, the power through the rotor is approximately 30% of the nominal power of the machine. Thus, the converter is designed for a reduced power range, leading to a lower cost and a lower size/weight of the installation.

One of the largest drawbacks of the DFIG is the need of a set of carbon brushes in order to connect the rotating part to the stationary power electronics. In order to keep the machine in operation for a long time, these mechanical parts need maintenance due to wear of the carbon material as a consequence of the friction between the brushes and the rings.

2.2.1 Possible alternative topologies

In order to solve the brush issue without removing the advantages of a DFIG configuration, some solutions have been proposed in the literature.

Brushless DFIG with external power electronics

The first possible solution is a brushless configuration of a DFIG with the power electronic converter connected to the rotor windings through a wound exciter (Fig. 2.3). The currents for controlling the magnetic field in the rotor windings are regulated by the power electronics, but they are induced in the rotor windings from the stator of the wound exciter. This configuration does not need brushes and rings, but the main drawback is the impossibility of generating a DC current in the rotor winding, which is necessary when the rotor is rotating at synchronous speed.

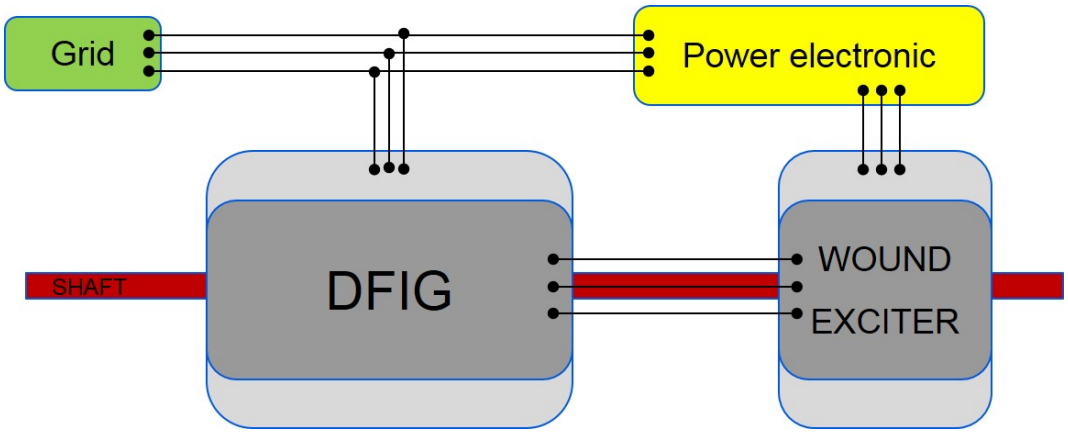

Fig. 2.3: Schematic of a brushless DFIG with external power electronics and a wound exciter.

Brushless with a rotary permanent magnets exciter and rotary power electronics

Another solution which avoids the use of brushes and rings is proposed in [4]. In this configuration, the power for the rotor excitation is generated directly in the rotor. This is obtained by using a permanent magnet generator on the same shaft of the DFIG: this auxiliary machine has magnets on the stator and the windings on the rotor. The rotor winding of the permanent-magnet machine are connected to the rotor windings of the DFIG through a power electronics converters, which controls the power flow between the two rotors. In the sub-synchronous mode, the DFIG needs power flowing ins the rotor winding: in this condition the permanent-magnet machine works as a generator and delivers the exciting energy to the DFIG, extracted from the mechanical energy of the shaft. In the super-synchronous mode, the DFIG delivers energy from the rotor windings, which is converted into mechanical energy on the shaft by the permanent-magnet machine. In this condition, the mechanical energy can be re-used by the DFIG as additional torque on the shaft.

A schematic of this topology is shown in Fig. 2.4. This technical solution solves the issue of the brushes, and the size of the power electronics is coupled with the maximum range of slip of the DFIG. Moreover, the permanent-magnet machine needs the same nominal power range of the of the power electronics.

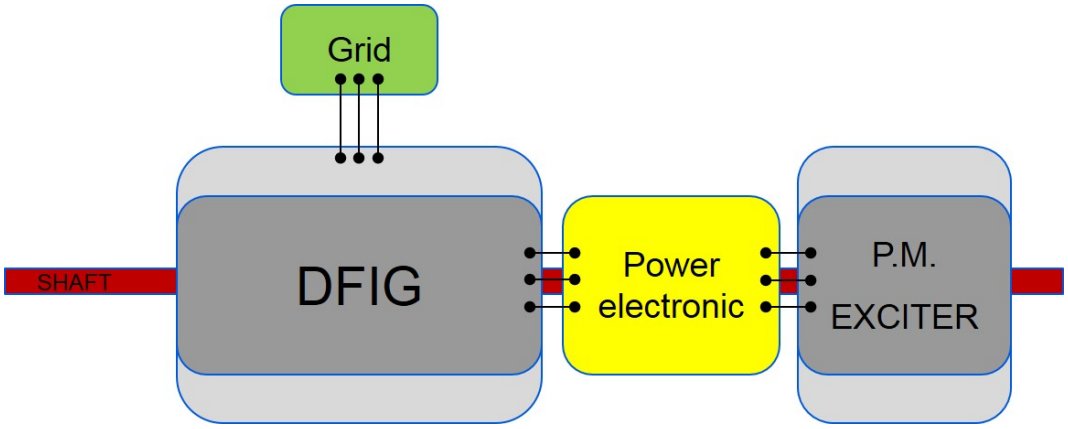

Fig. 2.4: Schematic of a brushless DFIG with a rotary permanent magnets exciter and rotary power electronics.

The Double-Doubly-Fed Induction Generator

The topology analysed in this report is shown in Fig. 2.5. Two DFIGs are coupled mechanically by sharing the same shaft, and electrically by the connecting the rotor windings through two inverters sharing the same DC bus. The stator windings of the two DFIGs are connected to the grid in parallel.

In this configuration, both machines are connected to the grid and both can convert mechanical energy into electric energy delivered to the grid. Taking in account the formulation (2.10), the number of pole pairs of the two machines must be different in order to obtain different slips and different synchronous speeds. This is a consequence of the application of the same voltage frequency (from the grid) to the stator windings of the two DFIGs. With the same synchronous speed for both DFIGs, the converter would not be able to exchange any excitation power because the power flow from one DFIG to the other would never happen.

This configuration does not need brushes when the power electronics is realised with a rotating converter. In order to define the relation between the nominal power of the power electronics and the slip range of the DFIGS, the analysis of this topology is carried out in the following chapters.

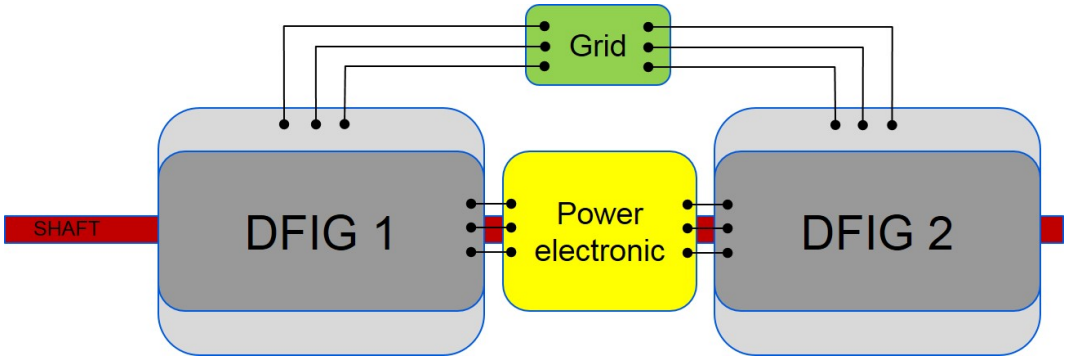

Fig. 2.5: Schematic of the Double-DFIG topology.

Chapter 3

ANALYSIS of the D-DFIG TOPOLOGY

The D-DFIG topology described in the Sect. 2.2.1 at page 10 needs to be analyzed in more details in order to understand how the power flows in the different sections of the machines.

The first analysis is carried out considering the equations of the machines in a lossless condition, in order to have a starting point on the possible dimension of the D-DFIG solution. Further machine simulations take in account the losses in the copper windings of the machine. The analytical formulation of the single DFIG is exploited to describe the topology under analysis. The results are obtained through the use of the software Matlab®.

Since the literature reported only one paper on the brushless DFIG topology [3], it was important to understand whether the calculations performed in [3] were correct. Therefore, the starting conditions of this analysis for the definition of the optimal design parameters are the same as in [3]. Only after a deeper understanding of this topology, other conditions were applied in order to considered aspects that were not investigated in the original paper.

3.1 Determination of the D-DFIG power equations

The maximum power that can flow in the different sections of the D-DFIG defines the machine dimensions and the power electronics dimension. The section below explains how the formulation of the power as function of the slips can be defined. It is important underlining that the power flows have the signs defined by the arrows in Fig. 3.1.

Topology equations The main point is the understanding of the equations that rule the flow of power between the machines at the same rotor speed. Several observations about the topology are required first. They are derived from the direction of the electrical and mechanic power that is depicted in Fig. 3.1, from which it is possible to determine new formulations with the help of the equations (2.12) and (2.13):

- the value of the rotor power flowing in the first machine is equal to the rotor power flowing from the second machine (with s_1 and s_2 indicating the respective machines slips):

$$P_r = \frac{s_1 P_{m1}}{1 - s_1} = -\frac{s_2 P_{m2}}{1 - s_2} \tag{3.1}$$

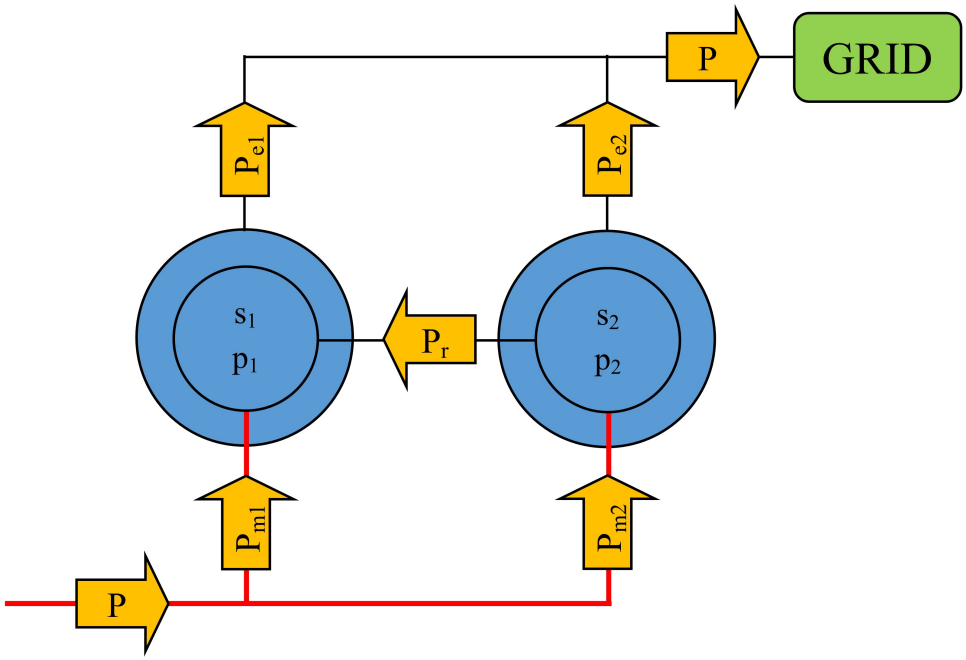

Fig. 3.1: Power flows in the D-DFIG configuration.

This formulation considers the power that flows inside the first rotor as positive, while the power that flows in the second rotor as negative;

- the mechanical power that flows inside the D-DFIG (called P in Fig. 3.1) is shared by the two machines: (P_{m1} is the mechanical power of the first machine, P_{m2} is that of the second machine):

$$P = P_{m1} + P_{m2} \tag{3.2}$$

- if the system is composed by two lossless machines and a lossless power electronics, the sum of the electric powers that flow from the first machine (P_{e1}) and the second machine (P_{e2}) is equal to the mechanical power that flows in the two machines:

$$P = P_{e1} + P_{e2} = \frac{P_{m1}}{1 - s_1} + \frac{P_{m2}}{1 - s_2} \tag{3.3}$$

The formulations (3.1), (3.2) and (3.3) are a valid description of the topology, but they take as input variables both the slips s_1 and s_2. A relation between the slips is now necessary to further relate the sizes of the two DFIGs.

Slips and poles pairs In order to generate the rotor power for excitation and controlling the machines, the number of poles pairs of the two DFIGs should be different ($p_1 \neq p_2$). In this way, while the mechanical speed of the two rotors is the same, the slips are different and consequently the field generated by the rotor currents in also different, even with opposite sign in certain operating conditions.

The slips are defined by [3]:

$$\begin{array}{rcll} s_1 & = & \dfrac{N_{01} - N_m}{N_{01}} & N_{01} = \dfrac{\omega_N}{p_1} \\ s_2 & = & \dfrac{N_{02} - N_m}{N_{02}} & N_{02} = \dfrac{\omega_N}{p_2} \end{array} \tag{3.4}$$

from which it is possible to define the relation between the slips:

$$s_2 = 1 + \frac{p_2}{p_1}(s_1 - 1) \tag{3.5}$$

A new variable is defined and called *Poles Ratio*, in order to simplify the formulation:

$$rp = \frac{p_2}{p_1} \tag{3.6}$$

Fig. 3.2 shows how s_2 changes according to (3.5) in the ranges $s_1 = [-1, 1]$ and $rp = [0, 1]$. The rp range considers always $p_2 < p_1$, but it is just a matter of notation. An increase of rp and increases the variation of s_2, with the possibility achieving negative values of s_2, while low rp values induce little variations of s_2.

In the following analysis, the rp values are considered as continuous in the whole range. However, it is necessary to underline that this is only a theoretical hypothesis in order to simplify the graphical analysis. In reality, the machines can accept only a discrete and limited number of poles pairs in order to correctly work in the typical ranges of wind application cases. The possible rp values are also limited by a physical realizability of the pole pair, which must be an integer number.

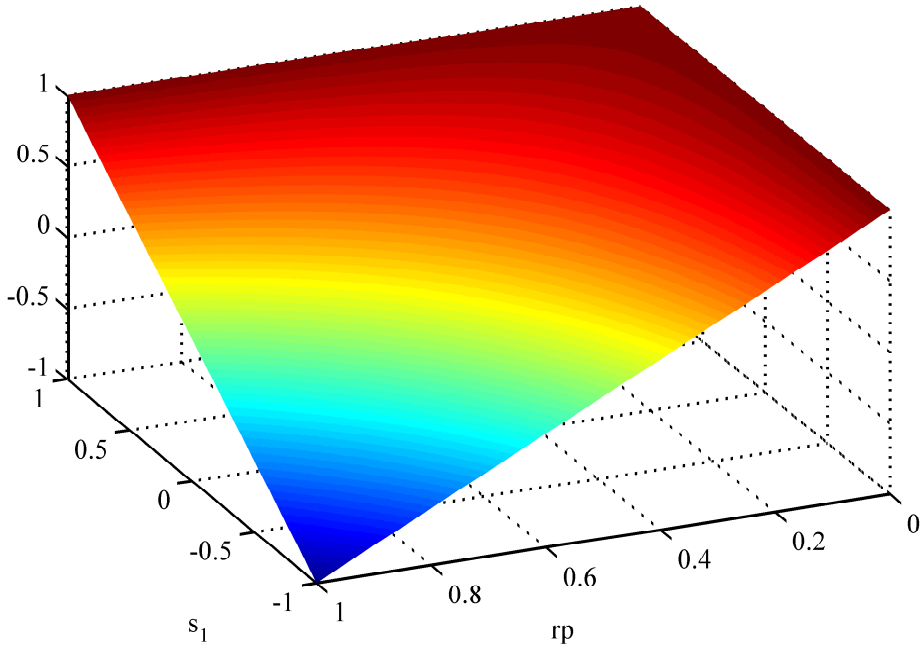

Fig. 3.2: s_2 in function of rp and s_1

3.1.1 The D-DFIG equations

Substituting the expressions (3.5) and (3.6) in the (3.1), (3.2) and (3.3), the powers in the D-DFIG system are described by the input variables P and s_1, with a fixed choice of rp. The formulation is the following, in agreement with Fig. 3.1:

$$P_r = \left\{ \frac{rp\, s_1}{rp-1} - \frac{s_1}{(1-s_1)(rp-1)} \right\} P \tag{3.7}$$

$$P_{e1} = \left\{ 1 - \frac{s_1}{(1-s_1)(rp-1)} \right\} P \tag{3.8}$$

$$P_{e2} = \left\{ \frac{s_1}{(1-s_1)(rp-1)} \right\} P \tag{3.9}$$

$$P_{m1} = \left\{ 1 - \frac{rp\, s_1}{rp-1} \right\} P \tag{3.10}$$

$$P_{m2} = \left\{ \frac{rp\, s_1}{rp-1} \right\} P \tag{3.11}$$

3.2 The analysis with constant input power

An analysis of the power flow in the different system sections by considering a constant input mechanical power P, and using as variables rp and s_1, is able to give an overview of the D-DFIG operation. The evaluation is performed under the assumption of lossless DFIGs and lossless power electronics.

Power through the rotors

The evaluation of the power flows through the rotary back-to-back converter is important to understand how to size the inverter. This is easily achieved by implementing the equation (3.7) in Matlab®, with $P = 1\ [p.u.]$ and a chosen range of $rp = [0.1, 0.9]$ and $s_1 = [-0.6, 0.6]$.

Fig. 3.3 shows that P_r has a parabolic trend for a constant rp, and that P_r is null for $s_1 = 0$. This is caused by the fact that the *machine 1* works at synchronous speed, which means that no excitation power is required in a lossless system.

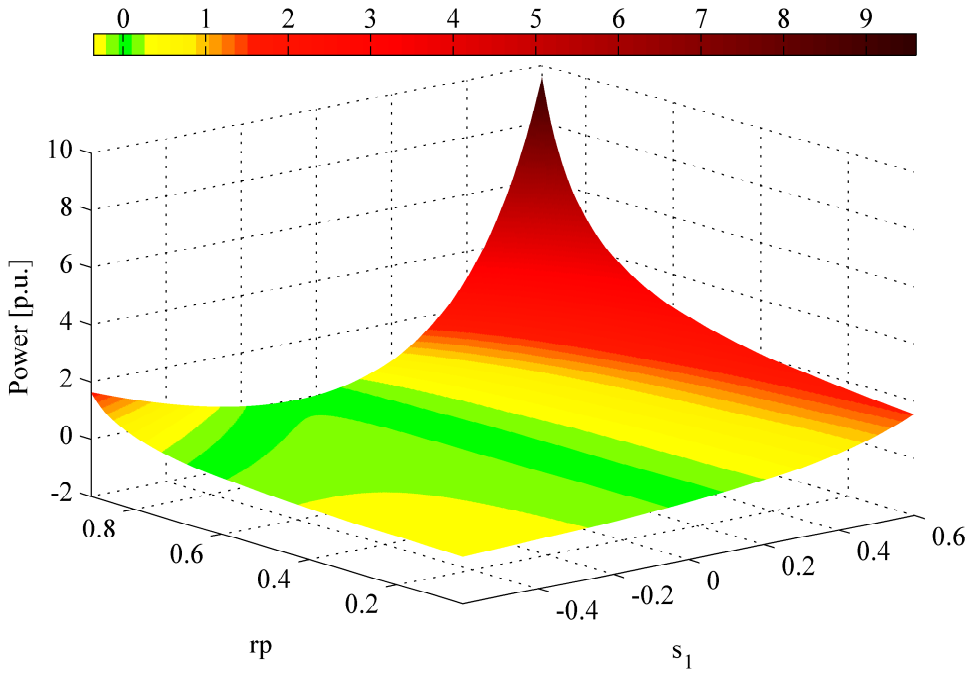

Fig. 3.3: Power P_r through the rotary power electronic (in p.u.), as function of rp and s_1.

There exists a great range of parameters which result in a low power flowing through the rotors, in particular for low values of rp: in this area, the parabolic trends are flatter and close to the zero-surface. The zones where rp is near one, instead, show significantly higher rotor powers, with a steep gradient.

Fig. 3.3 highlights the area of lowest rotor power in green colour, while the yellow colour is used for rotor powers below $1[p.u.]$. Red colours are used instead for rotor powers over $1[p.u.]$. Obviously, for $s_1 = 0$ the surface is all green. What is more insteresting, however, is the green area with values of rp between 0.4 and 0.7.

Power curves with constant input power

Since the D-DFIG configuration and interaction between the machines is more complex than a conventional DFIG installation, a graphical representation of the equations (3.5), (3.7), (3.8), (3.9), (3.10) and (3.11), as function of s_1 domain in $[p.u.]$ unit, might help in understanding the trends of the power curves. It is assumed $P = 1\ p.u.$, and the nominal power P_N is used

as the base value for the graphs in *p.u.* scale. The power curves are computed for two values of rp in Fig. 3.4 and Fig. 3.5, for $rp = 0,5$ and $rp = 0,75$ respectively[1].

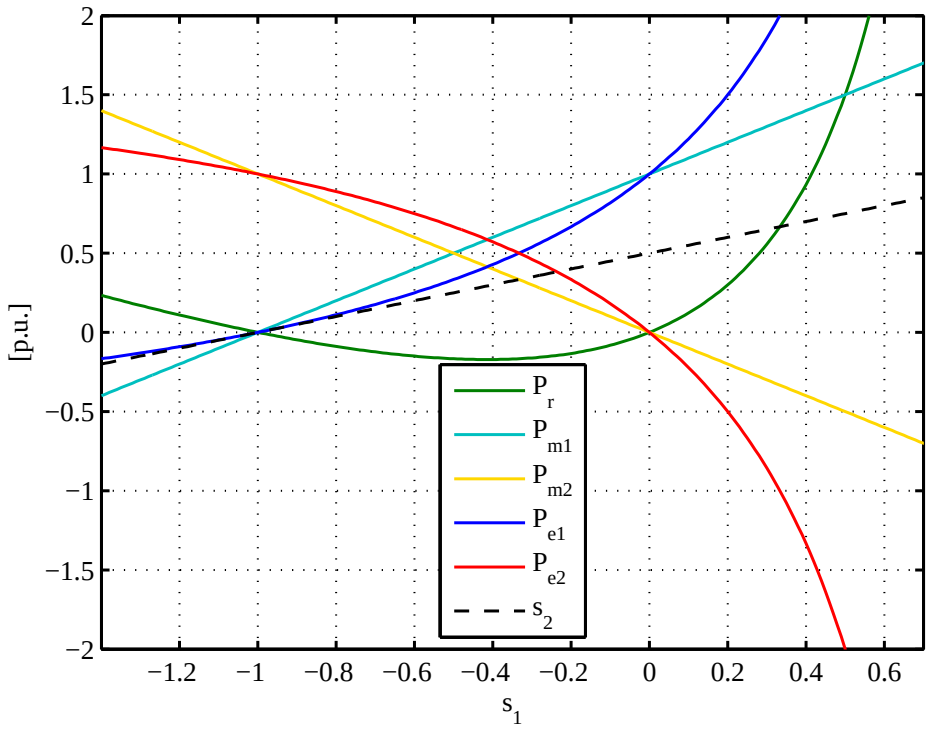

Fig. 3.4: Power flow and s_2 with constant mechanical input power $P = 1$ [*p.u.*] and with $rp = 0,5$.

In both figures, three operating ranges are distinguishable based on the points where s_1 and s_2 are equal to zero. The behavior of the machine is the same for the two different rp values, and it can be described in the same way for all other values of pole rates. The ranges are defined as follows:

- $s_1 > 0$ and $s_2 > 0 \quad \Rightarrow \quad P_{e1}, P_{m1} > 0; \quad P_{e2}, P_{m2} < 0; \quad P_r > 0$, depicted in Fig. 3.6 a);
- $s_1 < 0$ and $s_2 > 0 \quad \Rightarrow \quad P_{e1}, P_{m1} > 0; \quad P_{e2}, P_{m2} > 0; \quad P_r < 0$, depicted in Fig. 3.6 b);
- $s_1 < 0$ and $s_2 < 0 \quad \Rightarrow \quad P_{e1}, P_{m1} < 0; \quad P_{e2}, P_{m2} < 0; \quad P_r > 0$, depicted in Fig. 3.6 c).

Furthermore, there are two points where one of the machines does not operate and P_r is null. These points correspond to the synchronous speeds of the machines:

- $s_1 = 0$: all the power flows through the machine 1, and the machine 2 does not operate;

[1] Again, the system is considered lossless.

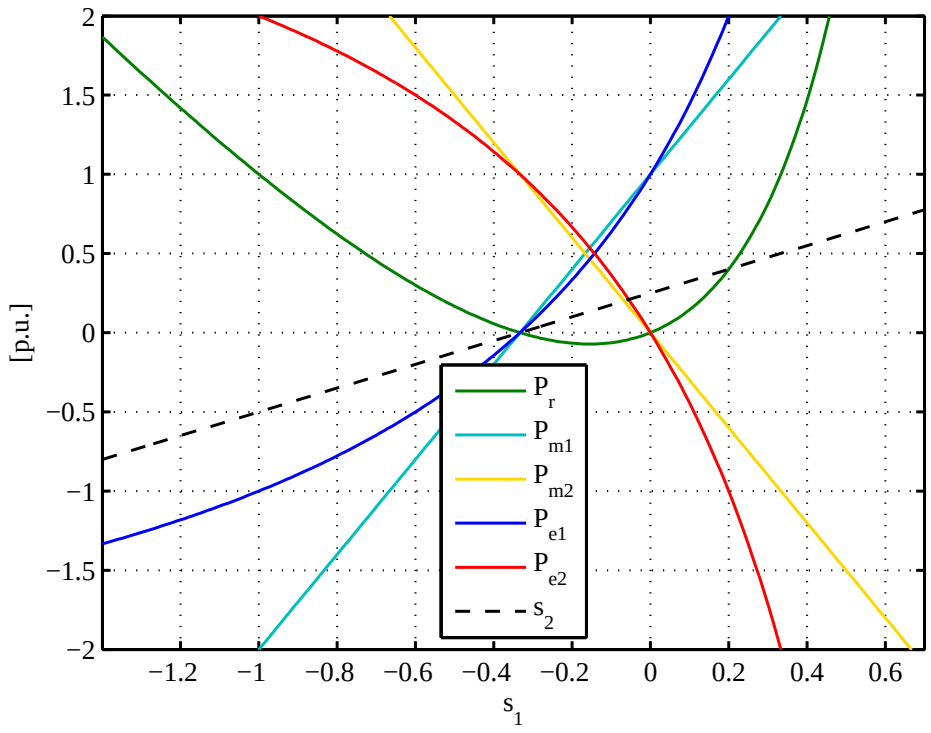

Fig. 3.5: Power flow and s_2 with constant mechanical input power $P = 1$ $[p.u.]$ and with $rp = 0,75$.

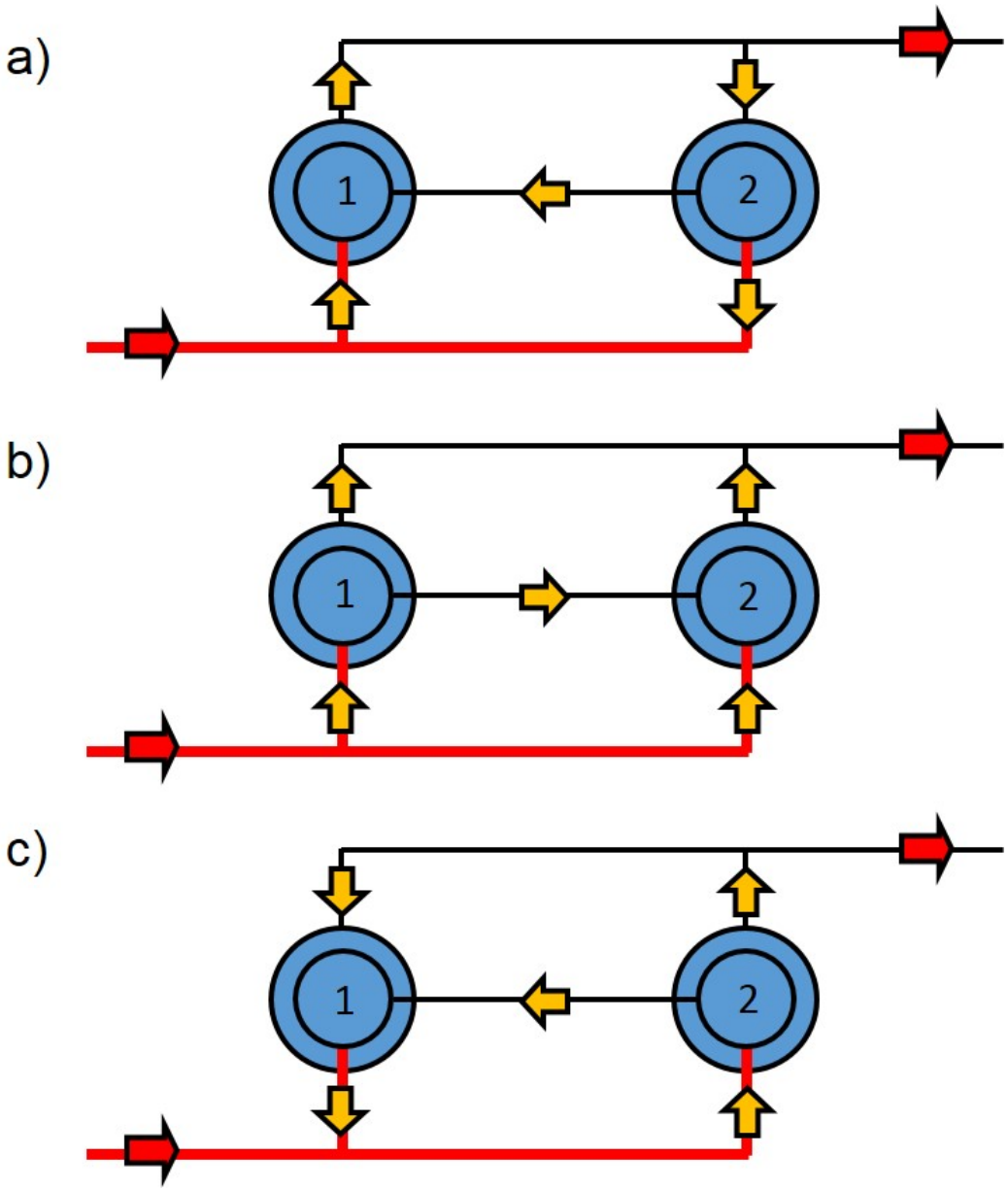

Fig. 3.6: Power paths in the machines for the different operating ranges.

- $s_2 = 0$: all the power flows through the machine 2, and the machine 1 does not operate.

From the above considerations, it is possible to observe that for the slips ranges $s_1 > 0, s_2 > 0$ and $s_1 < 0, s_2 < 0$ there is a loop of energy between the two machines in the D-DFIG configuration. These conditions are not convenient as there is a (useless) flow of energy between the machines that produces unwanted losses.

3.3 Analysis of D-DFIG for wind generator application

The starting condition of the previous analysis (constant input power) is advantageous to understand the behavior of an ideal D-DFIG system, but it is not useful for wind power applications. This is because a variation of slip means a variation of rotor speed, which in a wind turbine implies a consequent variation of the incoming mechanical power that the wind can deliver to the rotor. The relation between the wind speed and the power is typically described by a relation that take in account parameters of the turbine geometry. The following paragraph describes the considerations made in order to simplify a relation between wind speed and mechanical rotor power in the D-DFIG analysis.

The application of a variable input power in the formulation (3.8), (3.9), (3.10), (3.11) and (3.7) is relatively straightforward, as the equations only need to be updated by substituting a new equation for P.

Representation of the wind power profile on a wind rotor

The wind power is well approximated by a cubic function as shown in Fig. 3.7. The function starts at V_{in}, the cut-in speed of the rotor. At the rated speed V_r and beyond, the power remains constant for a range of rotor speed, till a cut-out speed V_{out} is reached. At cut-out speed, the power has a rapid decrease to zero.

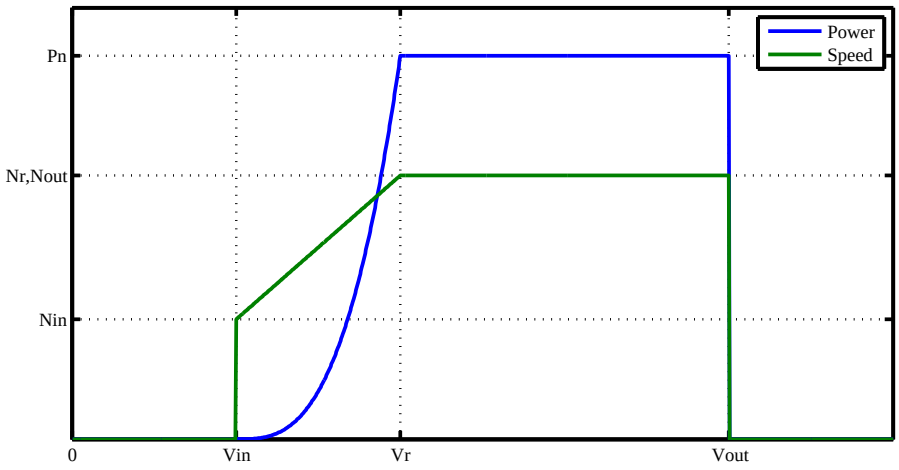

Fig. 3.7: Power of the wind, by variables wind speed.

Fig. 3.7 shows also the rotor speed as function of the wind speed. The rotor speed start

from a value N_{in} and has a proportional increase to N_r, after which is maintained constant by the blade control, or by the geometry of the blade.

As elaborated in [5], the definition of a wind power curve as a cubic curve with respect the wind speed is a theoretical simplification, but it is a good approximation in order to carry out a first analysis of a new wind generator.

3.3.1 Wind power characteristic in D-DFIG computation

The first choice is the definition of the rotational speed when $s_1 = 0$, and the working range of slip. The paper [3] suggests to use the following simplifying assumptions:

1. the shaft input power is set to zero at cut-in wind speed ($P_{cut-in} = 0\,[W]$);
2. the shaft input power is proportional to the cube of the wind, and the shaft rotating speed is directly proportional to wind speed in the wind speed region from cut-in to rated wind speed;
3. the rotor speed is kept constant beyond the rated speed point by controlling the pitch of the blades in order to maintain it constant from V_r to V_{out};
4. the synchronous rotor speed, N_0, is set between the cut-in rotational speed (N_{in}) and rated rotational speed (N_r).

The assumption 4 requires the definition of several design rules. It is necessary to define the rated slip of the machine, $-s_1^r$, the slip corresponding to the rated rotational speed, and consequently the slip corresponding to the cut-in speed, which is named s_1^r. This will define the maximum range of slip in the machine 1, and with the chosen value for rp in 3.2, one can find the range of slip for the machine 2.

The wind-power characteristic is then described by (with N_m mechanical speed):

$$P = \left(\frac{N_m - N_{in}}{N_r - N_{in}} \right)^3_{N_{in}=2N_0-N_r} \qquad [p.u.] \tag{3.12}$$

This equation has N_{in} and N_r as constant values, while N_m is variable. In order to use te slip as a variable, it is necessary to use the equations (3.4), and the relation becomes:

$$P = \left(\frac{s_1^r - s_1}{2\, s_1^r} \right)^3 \qquad [p.u.] \tag{3.13}$$

Several graphs useful to describe the power flows in the D-DFIG can now be obtained. Obviously, the use of a slip range of $\pm s_1^r$ allows a speed range that starts from $N_{in} = \frac{\omega_N}{p_1}(1-s_1^r)$ to $N_r = \frac{\omega_N}{p_1}(1 + s_1^r)$. This implies that the speed range is:

$$\Delta N = 2\, \frac{\omega_N}{p_1}\, s_1^r \qquad [rpm] \tag{3.14}$$

The above mentioned assumptions are used for a starting evaluation on the machine power trend in the power paths. The first part of the evaluation follows all the simplifying assumptions, while the second deeper evaluation argues about the variation of some assumptions and the investigation of the results in the new condition. All the following graphs and evaluations are computed with the power in $[p.u.]$ with respect to the nominal power P_N as base value.

The first analysis made with the cubic wind power characteristic as input is developed with all the above mentioned assumptions, as suggested in the bibliography [3]. In order to find the optimum design of the machine, it is necessary evaluate $|s_1^r|$ and rp.

An example of the power trend as function of the slip variation with random starting values of machines pole pairs and maximum slip is shown in Fig. 3.8, where $rp = 0.75$ (it means that if the first machine has $p_1 = 4$ pole pairs, the second machine has $p_2 = 3$ pole pairs), and a maximum slip of the first machine $|s_1^r| = 0.8$. The slip ranges are refereed to the machine 1, which works symmetrically respect $s_1 = 0$, while the second machine works only with positive slips in this case. This condition depends on the values of rp and $|s_1^r|$.

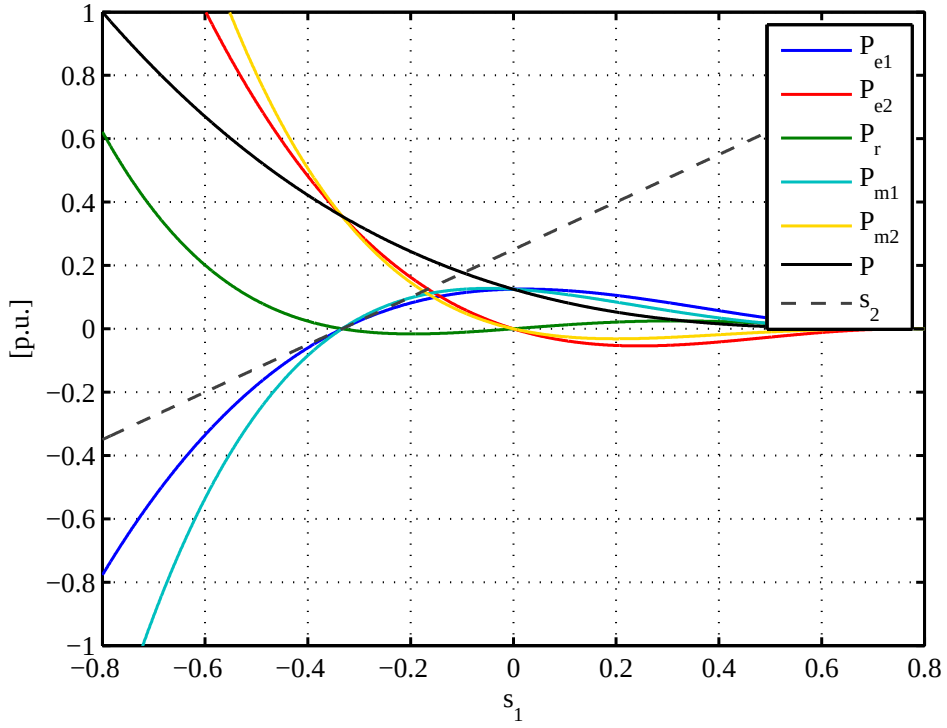

Fig. 3.8: Powers flows and s_2 for $|s_1^r| = 0.8$ and $rp = 0.75$.

Fig. 3.8 shows that the second machine needs an oversizing, as its mechanical and electrical (stator) powers increase over 1 $[p.u.]$. At the same time, the mechanical and electrical (stator) powers of the first machine become negative, creating a power loop circulation between the two machines that incresed the total power circulating in the D-DFIG configuration. Since this loop will only create unnecessary losses, the chosen values of rp and $|s_1^r|$ are not recommended and a deeper analysis is required.

This phenomenon was already visible in the simplified analysis of Fig. 3.4 and Fig. 3.5:, where the slips had the same sign and a power loop was generated. This phenomenon is not so evident with positive s_1 and with a cubic wind power curve, because when the first machine works in super-synchronous mode the input power is very low. Therefore the power loop is not avoided but it is only less evident. In the following analysis, a more complete evaluation of the loop impact on the system in relation to the input/output power is performed.

Maximum power graphs

In order to evaluate the maximum power flowing in the system with different combinations of rp and $|s_1^r|$, an automatic Matlab® code was developed in order to save the maximum power value obtained for selected ranges of s_1^r (for easiness, in the following text $s_1^r = |s_1^r|$) and rp as input variables.

The first graph in Fig. 3.9 shows the maximum value of the power (in $[p.u.]$) flowing through the power electronic. for s_1^r from $s_1^r = 0.1$ to $s_1^r = 1$, with intervals of $\Delta s_1^r = 0.1$.

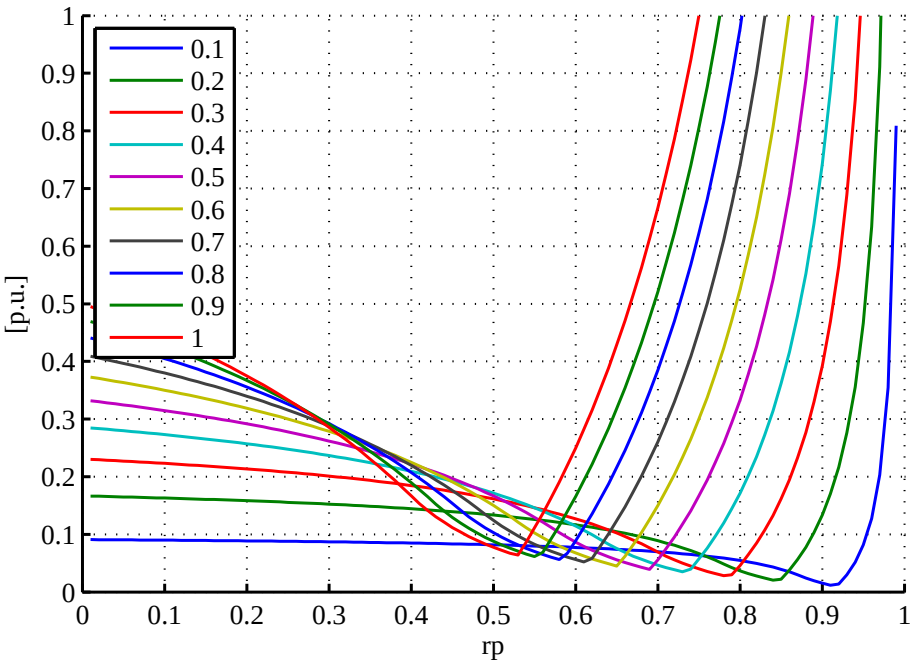

Fig. 3.9: Maximum power value in the power electronics (the chosen s_1^r values are in the legend).

It is possible to see that for low values of s_1^r (between $0.2 < s_1^r < 0.1$) and $rp < 0.8$, the rotor power is always under $0.2\,[p.u.]$. For values of $s_1^r > 0.3$, the low power region decreases and for the value $s_1^r = 1$ the only values under $0.2\,[p.u.]$ are approximately located in the interval $rp = 0.5 \pm 0.1$. This evaluation is important to show how the dimension of the power electronics can be achieved through a proper selection of pole pairs. We can conclude that:

1. with rp values very close to 1, the rotor power is quite large;
2. if s_1^r is close to 0.1, low rp values allow rotor powers under $0.2\,[p.u.]$.

Other types of analysis are possible, as shown in Fig. 3.10, Fig. 3.11, Fig. 3.12 and Fig. 3.13. Fig. 3.10 shows the highest mechanical power in the DFIG 1, while Fig. 3.11 shows the highest electrical power in the DFIG 1. Fig. 3.12 shows the highest mechanical power in the DFIG 2, while Fig. 3.13 shows the highest electrical stator power in the DFIG 2.

Fig. 3.11 and Fig. 3.10 reveal that the trend of the maximum powers is similar and differs only for the maximum rotor power value. The same applies for Fig. 3.12 and Fig. 3.13, where

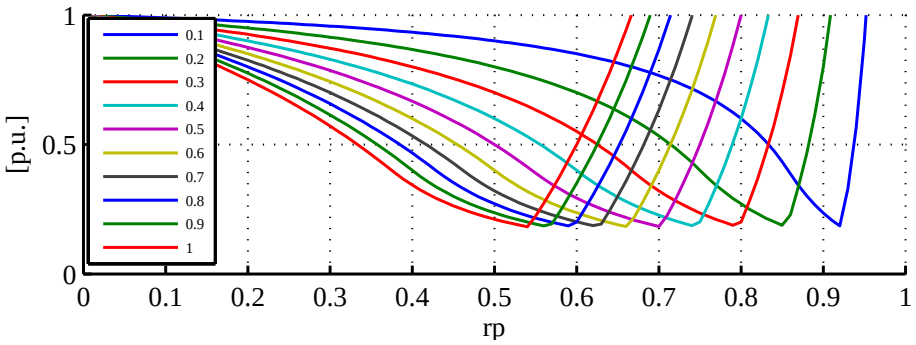

Fig. 3.10: Maximum mechanical power in the DFIG 1, in the legend the s_1^r values of the curves.

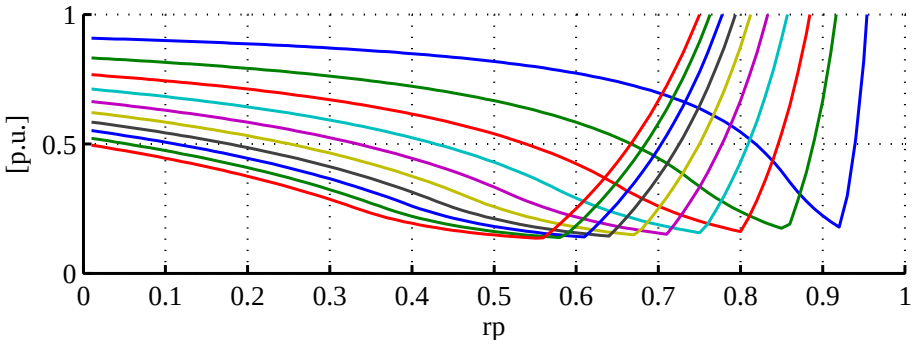

Fig. 3.11: Maximum electrical power in the DFIG 1.

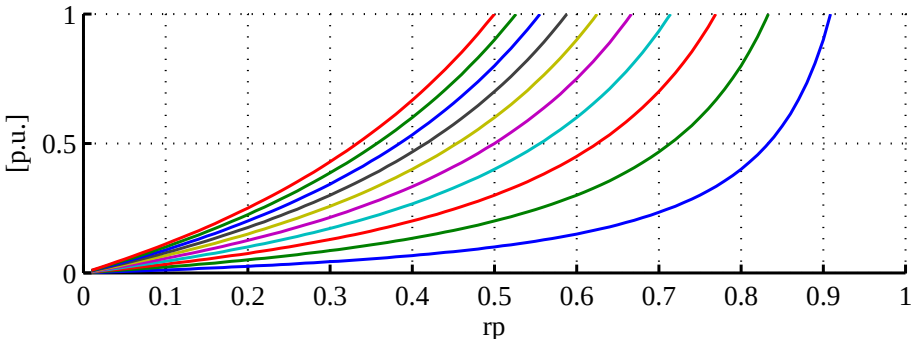

Fig. 3.12: Maximum mechanical power in the DFIG 2.

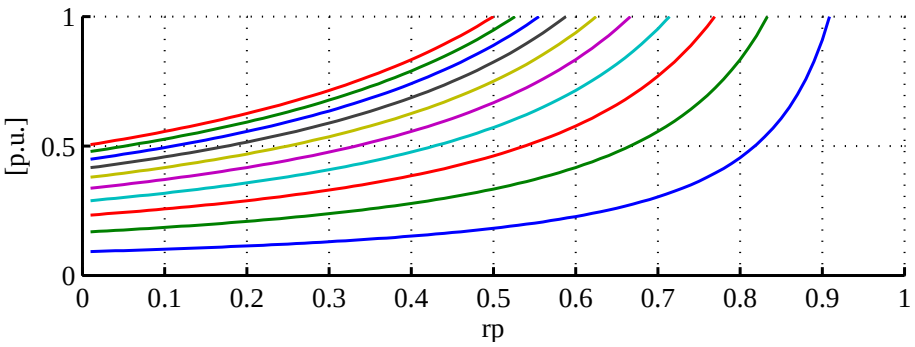

Fig. 3.13: Maximum electrical power in the DFIG 2.

only the sign changes with respect to the maximum rotor power. This case is interesting in order to observe the range of rp that allow a powers flow under 1 $[p.u.]$, because any choice of rp and s_1^r allowing a power greater than 1 will follow the same case described in Fig. 3.8 where the power flowing in second machine rises over 1 $[p.u.]$ in order to compensate for the undesired power loop between the machines. It can also be observed that a lower value of rp means a lower power size for the second machine.

Graph of the optimal rp and s_1^r

In order easily evaluate the optimum values of rp and s_1^r for the D-DFIG configuration, a fine mesh for both parameters was created with $rp = [0, 2]$, $s_1^r = [0, 1]$. The following conditions were evaluated for each combination of parameters, giving a certain number of points for the fulfilment of each of them:

- the maximum rotor power must be under 20% of the nominal power P_N: 1 point is added to the combination if not fulfilled;
- the maximum power flowing inside the machine 1, P_{m1}, must be under P_N: 2 points are added to the combination if not fulfilled;
- the maximum power flowing inside the machine 2, P_{m2}, must be under P_N: 4 points are added to the combination if not fulfilled;
- the sum of the maximum power flowing out the machine 1 and the maximum power flowing out the machine 2 (P_e^{sum}) must be under P_N: 8 points are added to the combination if not fulfilled.

The choice $P_r > 0.2P$ is performed as a first evaluation case and will be re-discussed later. The last condition is imposed to avoid the rp and the s_1^r values to oversize the nominal power, which is a possible configuration case. The result of this analysis is shown in Fig. 3.14.

The results show that the available range of values is located below the point $rp = 1$ and it has a maximum value of s_1^r between 0.4 and 0.6. This graph explains also the preliminary analysis of page 21, confirming that the choice was not optimal.

An example of D-DFIG dimensioning

The rp must be a realizable value, thus the pole pairs number must be an integer number. A possible value is $rp = 0.5$ (which means that $p_1 = 2p_2$) and $s_1^r = 0.5$; these parameters are

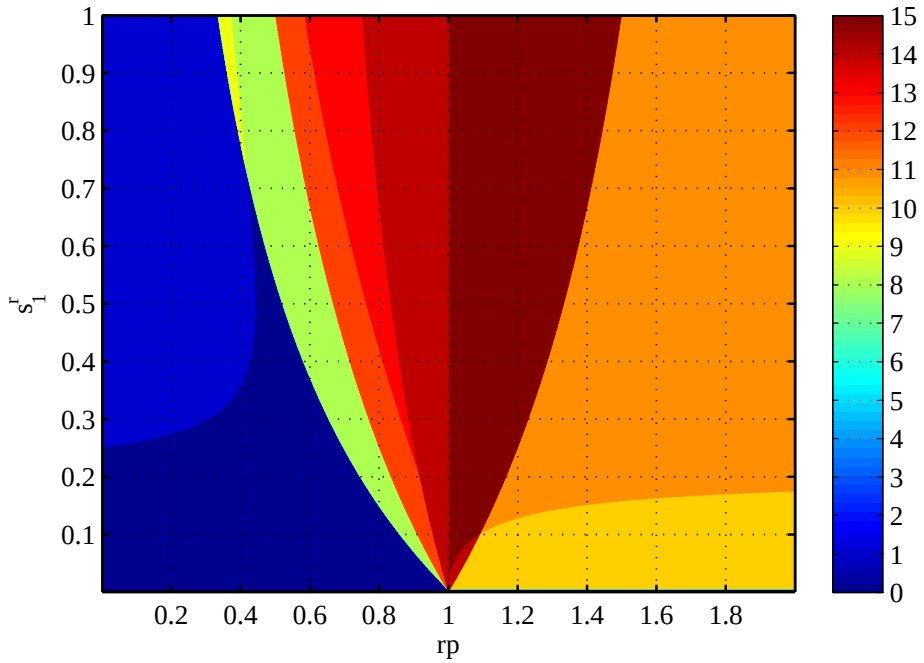

Fig. 3.14: Map of the allowed rp and s_1^r at the chosen conditions. The values in the graph mean: **0** allowed area, **1** $P_r > 0.2P_N$, **2** $P_{m1} > P_N$, **3** $P_{m1} > P_N$ and $P_r > 0.2P_N$, **4** $P_{m2} > P_N$, **5** $P_{m2} > P_N$ and $P_r > 0.2P_N$, **6** $P_{m1} > P_N$ and $P_{m2} > Pv$, **7** $P_r > 0.2P_N$ and $P_{m1} > P_N$ and $P_{m2} > P_N$, **8** $P_e^{sum} > P_N$, **9** $P_e^{sum} > P_N$ and $P_r > 0.2P_N$, **10** $P_e^{sum} > P_N$ and $P_{m1} > P_N$, **11** $P_e^{sum} > P_N$ and $P_{m1} > P_N$ and $P_r > 0.2P_N$, **12** $P_e^{summ} > P_N$ and $P_{m2} > P_N$, **13** $P_e^{sum} > P_N$ and $P_{m2} > P_N$ and $P_r > 0.2P_N$, **14** $P_e^{sum} > P_N$ and $P_{m1} > P_N$ and $P_{m2} > P_N$, **15** $P_e^{sum} > P_N$ and $P_{m1} > P_N$ and $P_{m2} > P_N$ and $P_r > 0.2P_N$.

taken from Fig. 3.14. A possible example may be a D-DFIG with $p_1 = 2$ and $p_2 = 1$; the speed is defined by the first machine, and with $f = 50Hz$ grid frequency the synchronous speed is (by the (3.4)) $N_0 = 1500$ rpm, with a range from $N_{min} = 750$ rpm to $N_{max} = 2250$ rpm (with $\Delta N = 1500$ rpm).

Fig. 3.15 show the power flows. The slip of the second machine, s_2, remains always in the positive range and at the minimum slip the machines share the same mechanical power (half of the total one). It is useful to observe that P_r remains limited under 20% of P_N ($P_r = 16.7\%P$ in the best case). P_r remain positive in the positive s_1 range, but becomes negative in the negative range of s_1; for $s_1 = 0$ the first machine works in its synchronous point and works alone, while the second machine is switched off. This agrees with the assumption of a lossless system.

Power loops of the dimensioning example

As mentioned at page 21, when s_1 and s_2 are equal in sign there is a power loop between the machines. A zoom of Fig. 3.15 where both slips are positive is reported in Fig. 3.16.

The following loops are identified:

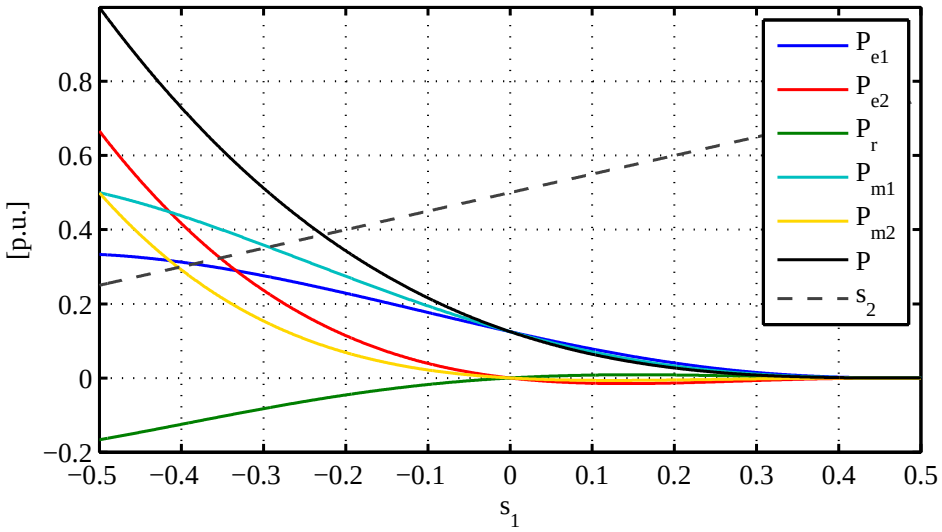

Fig. 3.15: Powers flows and s_2 for $s_1^r = 0.5$ and $rp = 0.5$.

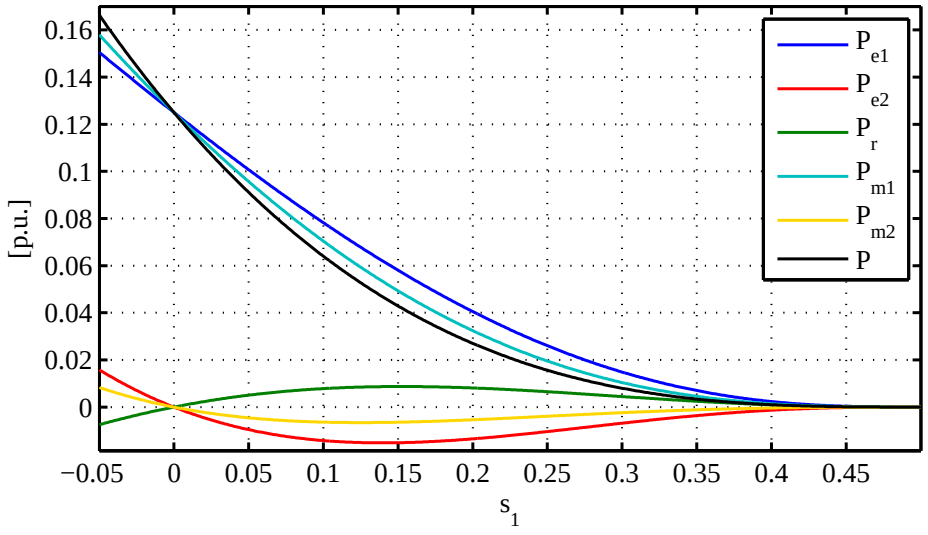

Fig. 3.16: Zoom of Fig. 3.15 for the positive slips.

- a loop through the rotary power electronics, called P^r_{loop}: this loop is due do the excitation needs and it is not delivered to the grid by the D-DFIG, but it remains in the electrical circuit (out from the stator of the first machine, and into the stator of the second machine);
- a loop through the shaft, called P^m_{loop}: in this region, the mechanical power of the second machine is negative, indicating that the second DFIG is working as a motor. This mechanical contribution is converted into electrical power by the first machine working as a generator, and then goes in back again into the second machine as electrical power. It is curious to observe how the power in this loop involves both the mechanical and the electrical conversion processes.

The loops have the same direction and start from the grid to the stator of the second machine. The total loop power that flows through the second machine stator is named P^{tot}_{loop}:

$$P^{tot}_{loop} = P^r_{loop} + P^m_{loop} \tag{3.15}$$

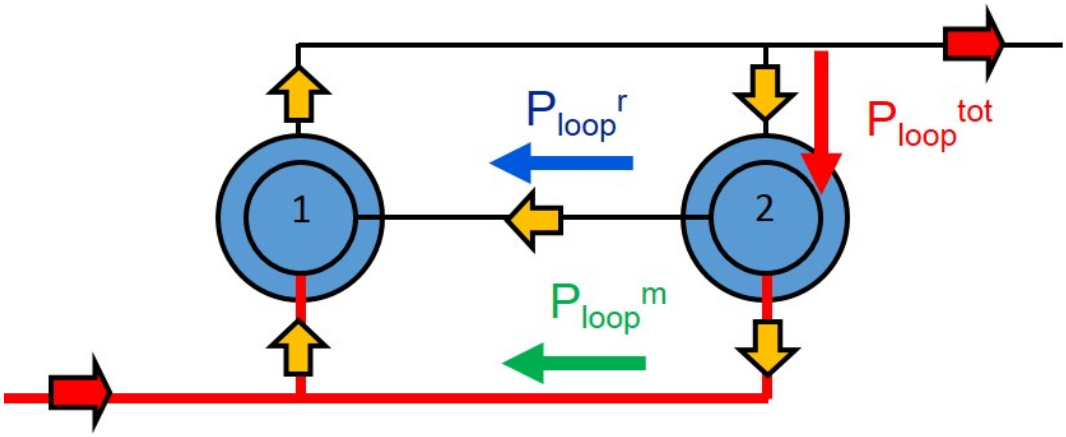

Fig. 3.17: The loop paths in the D-DFIG.

These power loops, using the parameters at page 24, are not large with respect to the nominal power P_N, but they affect the system because they appear for slip ranges where the output power is already low (as visible in Fig. 3.15). It is possible to evaluate their impact by calculating the power ratio R between the loop power and the nominal power, as below:

$$R^r_{loop} = \frac{P^r_{loop}}{P}, \quad R^m_{loop} = \frac{P^m_{loop}}{P}, \quad R^{tot}_{loop} = \frac{P^r_{loop}}{P} = \frac{P^r_{loop} + P^m_{loop}}{P} \tag{3.16}$$

These ratio values, calculated with $rp = 0.5$ and $s^r_1 = 0.5$, are shown in Fig. 3.18, plotting only the region with non-zero loop power.

The loops have a rapid increase, with R^m_{loop} growing linearly and R^r_{loop} growing with a parabolic trend. P^m_{loop} remain always under $50\%P$, but P^r_{loop} grows over the input/output power to the $150\%P$ and obviously the sum P^{tot}_{loop} is twice the value of P in input/output. This analysis does not take in account the losses, but in a real system these loops are a source of other additional losses.

In order to take into account the effect of power loops, two additional conditions on the top of those used for tracing Fig. 3.19 can be added for searching the optimal values of s^r_1

!htbp

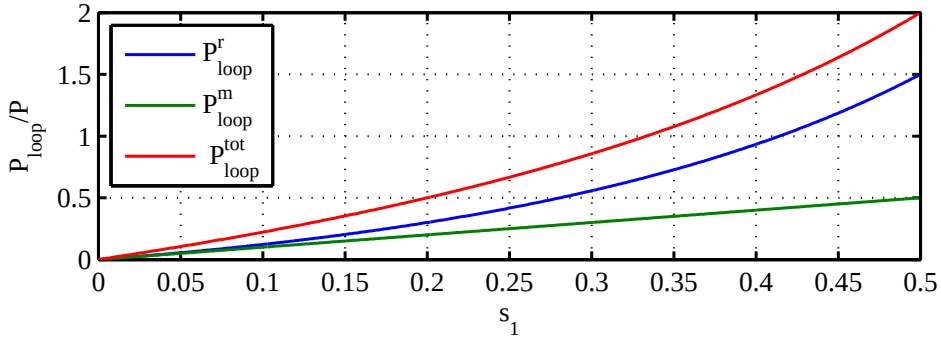

Fig. 3.18: Power loop ratios in the D-DFIG with $s_1^r = 0.5$ and $rp = 0.5$.

and rp (the results are shown in Fig. 3.19 and Fig. 3.20 where the gray area is the allowed one):

- the maximum R^r_{loop} must be under 0.5 in Fig. 3.19 ($P^r_{loop} < 50\%P$) and under 0.25 in Fig. 3.20 ($P^r_{loop} < 25\%P$);
- the maximum R^m_{loop} must be under 0.5 in Fig. 3.19 ($P^m_{loop} < 50\%P$) and under 0.25 in Fig. 3.20 ($P^m_{loop} < 25\%P$);
- the maximum R^{tot}_{loop} must be under 1 in Fig. 3.19 ($P^{tot}_{loop} < P$) and under 0.5 in Fig. 3.20 ($P^{tot}_{loop} < 50\%P$).

It is evident that the lower is the loop power, the loser is the limit for allowed s_1^r, which leads to a reduction of the speed variation. Fig. 3.19 shows also that the allowed region is located under $s_1^r = 0.3$, with a peak around $0.3 < rp < 0.4$. The situation in Fig. 3.20, instead, is such that the allowed region is located under $s_1^r = 0.2$ without peaks, decreasing with the increasing value of rp. A possible design choice from Fig. 3.19 is $rp = \frac{1}{3}$ and $s_1^r = 0.3$. These design values of design lead to the results shown in Fig. 3.21 and Fig. 3.22.

In Fig. 3.21, the power in the second DFIG remains lower then the first DFIG one for all slips, while the maximum power on the rotary converter increases up to 20% of the nominal (and maximum) power P_N. For positive values of s_1, the power in the second machine is very low and it is difficult understand the trend by the graphic in Fig. 3.21: in this region the second machine works as an exciter as the slip of this machine is very different from zero.

While $s_1 > 0$, the power loops remain under the limits imposed in the precedent analysis. It is possible see that the maximum value of the loop power in the rotor circuit is 50% of the input/output power P, and the loop closed through the shaft is lower than 15% of P.

Wind power characteristic with an initial power step

A further analysis, in order to get closer to real condition, is performed by introducing a non-zero starting power to simulate the cut-in condition in a wind turbine. This condition modifies the assumption 1 at page 20, by introducing a power step P_{cut-in} in the cubic function of the wind power. This test was performed in order to understand the effects on the power loops when the slips are both positive.

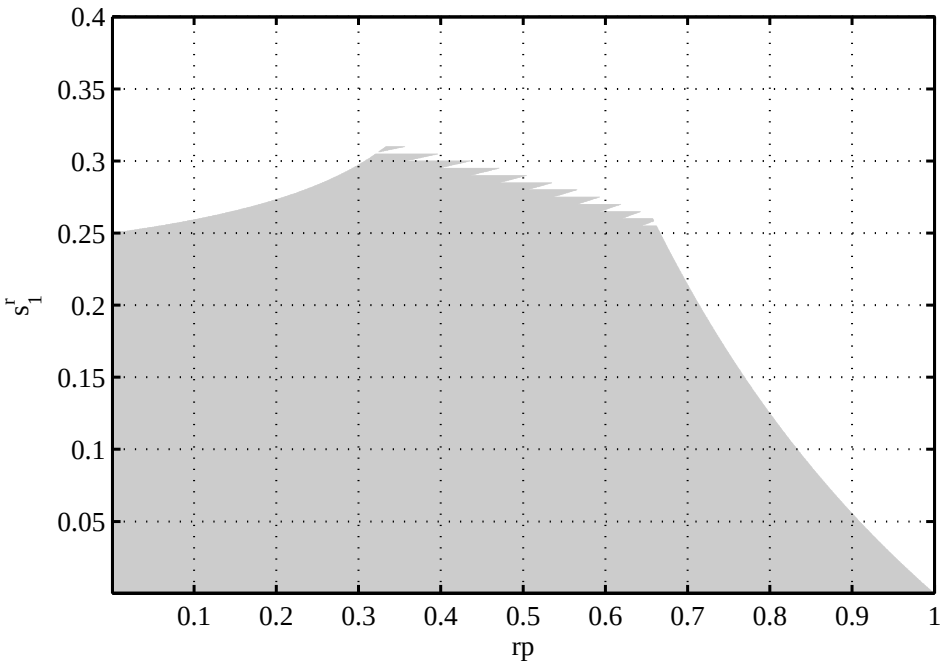

Fig. 3.19: Allowed region of rp and s_1^r for loop powers lower than 0.5 times the nominal power.

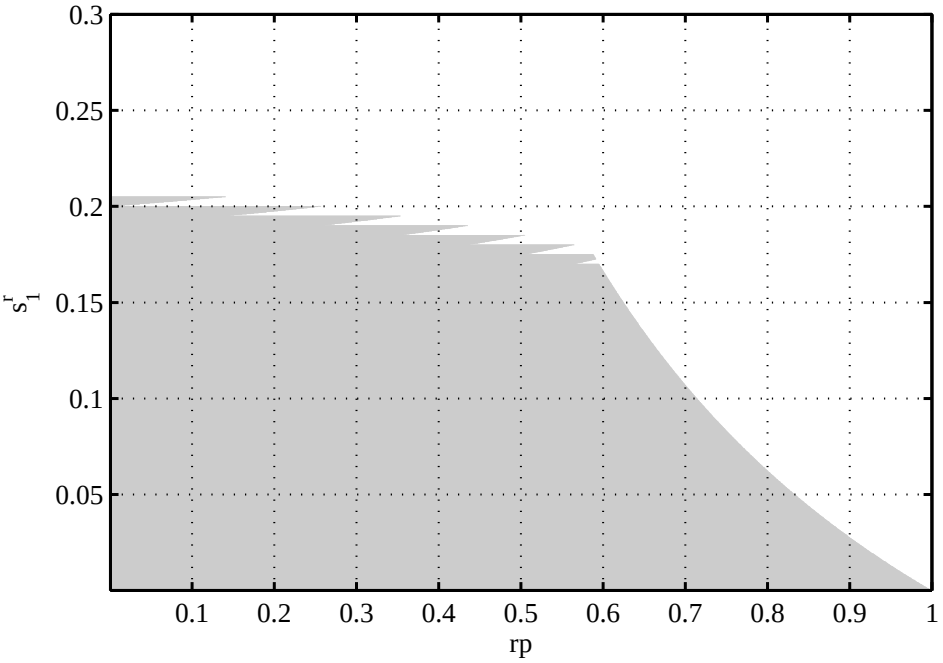

Fig. 3.20: Allowed region of rp and s_1^r for loop powers lower than 0.25 times the nominal power.

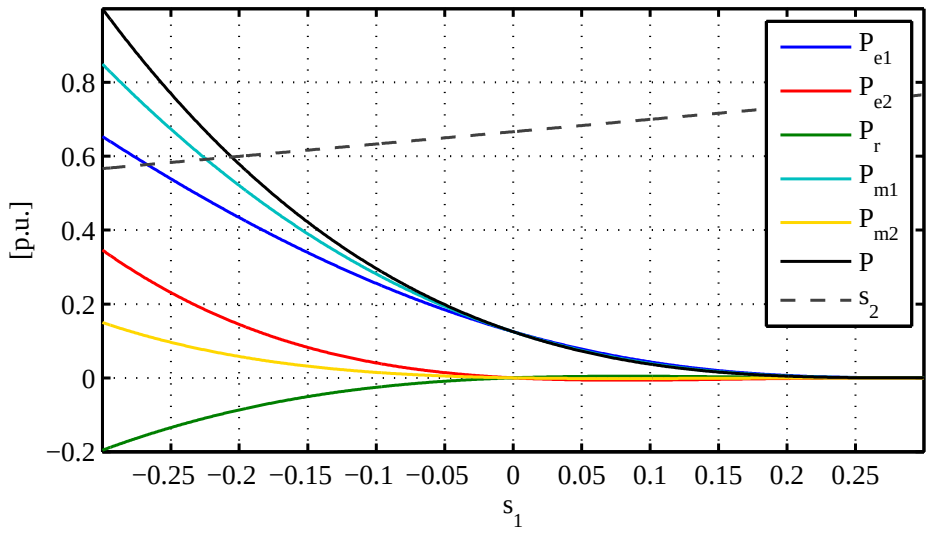

Fig. 3.21: Power flows in the machines for $s_1^r = 0.3$ and $rp = \frac{1}{3}$.

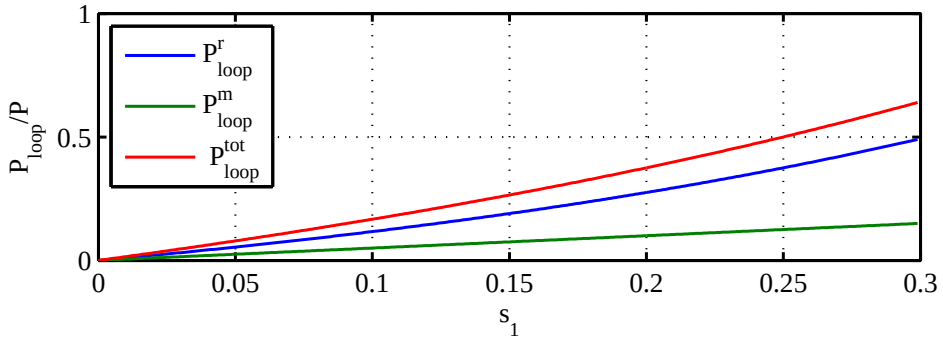

Fig. 3.22: Power loops in the machines for $s_1^r = 0.3$ and $rp = \frac{1}{3}$.

Fig. 3.23 shows the trend of the power with the inclusion of the initial step, where the parameters are $rp = \frac{1}{3}$, $s_1^r = 0.3$ and $P_{cut-in} = 10\%P_N$ (so the power starts from $0,1[p.u.]$). The power loops for the same conditions are shown in Fig. 3.24.

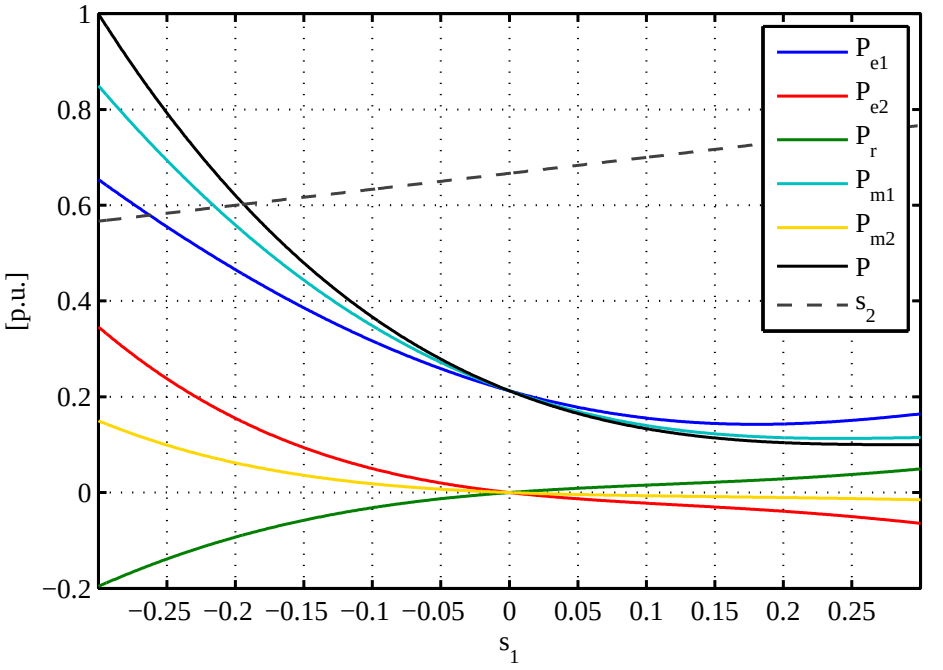

Fig. 3.23: Powers flows of the machine with $s_1^r = 0.3$ and $rp = \frac{1}{3}$ and an initial step, at $s_1 = 0.3$, of the $10\%P_N$.

The loops remain at the same ratio on P as the case without an initial power step.

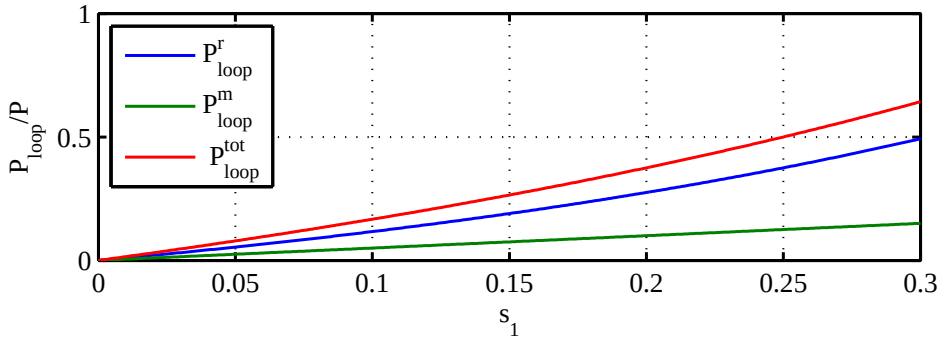

Fig. 3.24: Power Loops of the machine with $s_1^r = 0.3$ and $rp = \frac{1}{3}$ and an initial step, at $s_1 = 0.3$, of the $10\%P_N$.

Design choices with $s_1 < 0$ in the whole speed range

Another assumption that can be modified in order to search the optimal values of rp and s_1^r is the assumption 4 at page 20. As mentioned earlier, an issue at low wind speeds is represented by the power loops which could contribute to higher losses and an overall efficiency reduction of the D-DFIG system. In order to avoid this situation, it could be possible to move the position of the zero slip speed N_0 on the cut-in speed V_{in}. In this way the first machine will work only in supersynchronous mode, with a rated speed N_r calculated from the synchronous speed and the maximum slip $-s_1^r$. The range of possible speed is between N_0 and $N = \frac{60\,\omega}{p_1}\,(1 + s_1^r)$, equal to:

$$\Delta N = \frac{60\,\omega_N}{p_1}\,s_1^r \qquad [rpm] \tag{3.17}$$

The formulation remains the same as in (3.7), (3.8), (3.9), (3.10) and (3.11). Only the (3.12) and (3.13) need to be changed. The equation (3.13) becomes:

$$P = \left(\frac{-s_1}{s_1^r}\right)^3 \qquad [p.u.] \tag{3.18}$$

With this design choice, the power loops are avoided because the machines works always with different slip signs, the rotor powers flowing out the rotors can not have different sign and, in agreement with (2.10), both machines can work as generators. During the complete slip range P_r remains negative, and only for $s_1 = 0$ the excitation power exchanged between the rotors is null, but also the input and output power P is null.

In order to find the optimal values of rp an s_1^r, the same analysis of page 24 is performed, with the same conditions. A maximum power in the rotor circuits of $20\%P_N$ is set. The result is shown in Fig. 3.25.

Fig. 3.25 shows a large range of possible rp and s_1^r values: the areas are similar to those in Fig. 3.14, with all combinations beyond $rp = 1$ not allowed for a D-DFIG system. The values when $P_e^{summ} > P$ (the number 8) are reduced and consequently the allowed values are increased.

It is interesting to observe that the allowed area presents a peak between $rp = 0.4$ and $rp = 0.6$. This peak reaches $s_1^r = 1$ and therefore, by this analysis, the value $rp = 0.4, s_1^r$ could be usable. The possible values for $rp = 0.4$ could be $p_1 = 5$ and $p_2 = 2$. A possible analysis can be performed with these values.

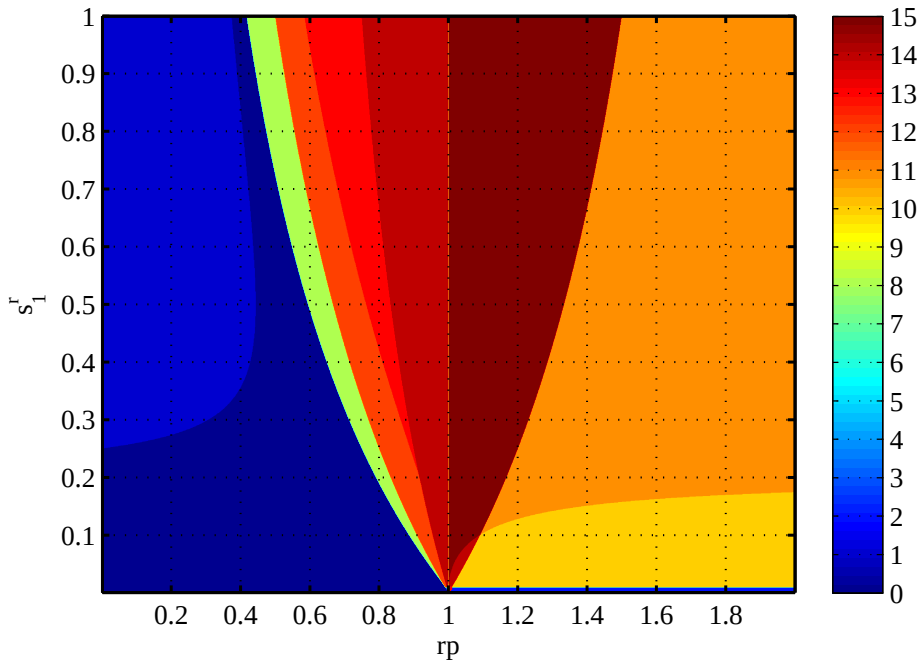

Fig. 3.25: Map of the allowed rp and s_1^r at the chosen conditions, with s_1^r always negative by design. The values in the graph mean: **0** allowed area, **1** $P_r > 0.2P_N$, **2** $P_{m1} > P_N$, **3** $P_{m1} > P_N$ and $P_r > 0.2P_N$, **4** $P_{m2} > P_N$, **5** $P_{m2} > P_N$ and $P_r > 0.2P_N$, **6** $P_{m1} > P_N$ and $P_{m2} > Pv$, **7** $P_r > 0.2P_N$ and $P_{m1} > P_N$ and $P_{m2} > P_N$, **8** $P_e^{sum} > P_N$, **9** $P_e^{sum} > P_N$ and $P_r > 0.2P_N$, **10** $P_e^{sum} > P_N$ and $P_{m1} > P_N$, **11** $P_e^{sum} > P_N$ and $P_{m1} > P_N$ and $P_r > 0.2P_N$, **12** $P_e^{summ} > P_N$ and $P_{m2} > P_N$, **13** $P_e^{sum} > P_N$ and $P_{m2} > P_N$ and $P_r > 0.2P_N$, **14** $P_e^{sum} > P_N$ and $P_{m1} > P_N$ and $P_{m2} > P_N$, **15** $P_e^{sum} > P_N$ and $P_{m1} > P_N$ and $P_{m2} > P_N$ and $P_r > 0.2P_N$.

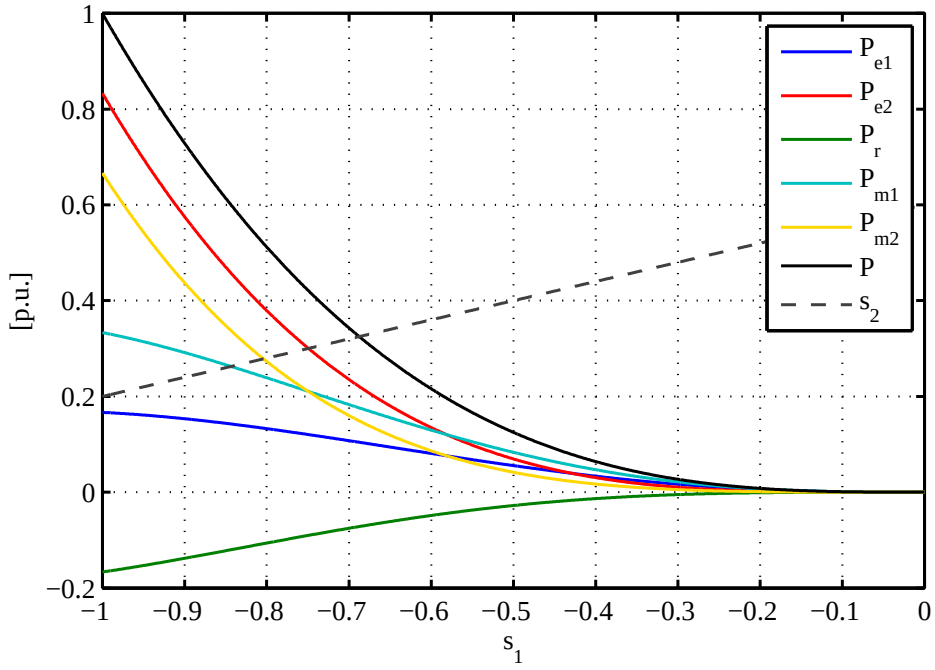

Fig. 3.26: Power flows with $s_1^r = 1$ and $rp = 0.4$, for the negative range of s_1.

Fig. 3.26 shows the power trends with these values as parameters. As expected, s_2 remains positive for all values of s_1. The power of the second machine increases near the nominal value of the input/output power P and the power flowing in the first machine remains low. The power trend are conditioned by the (2.10); this equation means that if $s = 1$ the power flowing inside the rotor must be equal to the power flowing off the stator windings (without considering the contribution of the losses). These conditions are impossible to design.

Optimal values for rp and $\mathbf{s_1^r}$, with rotor power lower than 30%$\mathbf{P_{e1}}, \mathbf{P_{e2}}$

A deeper evaluation of the P_r is now necessary. With the conditions at page 24 the rotor power is imposed to be lower than $20\%P_N$ in order to reduce the rating of the power electronics of the D-DFIG. This condition does not account for the relation between the rotor power, the stator power and the losses in the winding. In a standard DFIG machine, the power of the rotor does not usually increase over the 30% of the nominal power on the machine. Alternatively, it is possible to write this condition as if the range of slip is never outside $\pm s = 0.3$.

For a calculation of the optimal rp and s_1^r that takes in account this latest observation, the following new conditions are created:

- the rotor power must be, respect the fist machine, $P_r < 30\%P_{e1}$;
- the rotor power must be, respect the second machine, $P_r < 30\%P_{e2}$.

These conditions are added to the other conditions of page 24. The analysis is performed in the same way as for that showed in Fig. 3.14, with the same assumptions of page 20. The condition 4 at page 20 is also respected.

In these conditions, the system can work with same sign of slips in both the machines: this means that there are powers loops inside the D-DFIG. As in the previous analysis at page 28 the loops are now taken into consideration with three new conditions:

- the maximum R^r_{loop} must be under 0.5 ($P^r_{loop} < 50\%P$);
- the maximum R^m_{loop} must be under 0.5 ($P^m_{loop} < 50\%P$);
- the maximum R^{tot}_{loop} must be under 1 ($P^{tot}_{loop} < P$).

Fig. 3.27 shows the values that are in agreement with the imposed conditions. The range of possible rp is drastically reduced: the available values are only in the second half of the graph, beyond $rp = 0.5$, and under $s^r_1 = 0.3$. The maximum values s^r_1 of this area start from $rp = 0.55$ and decrease up to $rp = 0.66$. A possible, realizable, value of rp could be $rp = 0.6$, corresponding to $p_1 = 5$ and $p_2 = 3$, or $rp = 0.\bar{6} = 2/3$ which corresponds to $p_1 = 3$ and $p_2 = 2$. Multiple values of these pole pairs could also be accepted. Fig. 3.28 shows the power trends with the condition $rp = 0.\bar{6}$ and $s^r_1 = 0.25$. The maximum mechanical power is equal in both the machines. which leads to an equally shared torque and a closer physical dimension of the two machines.

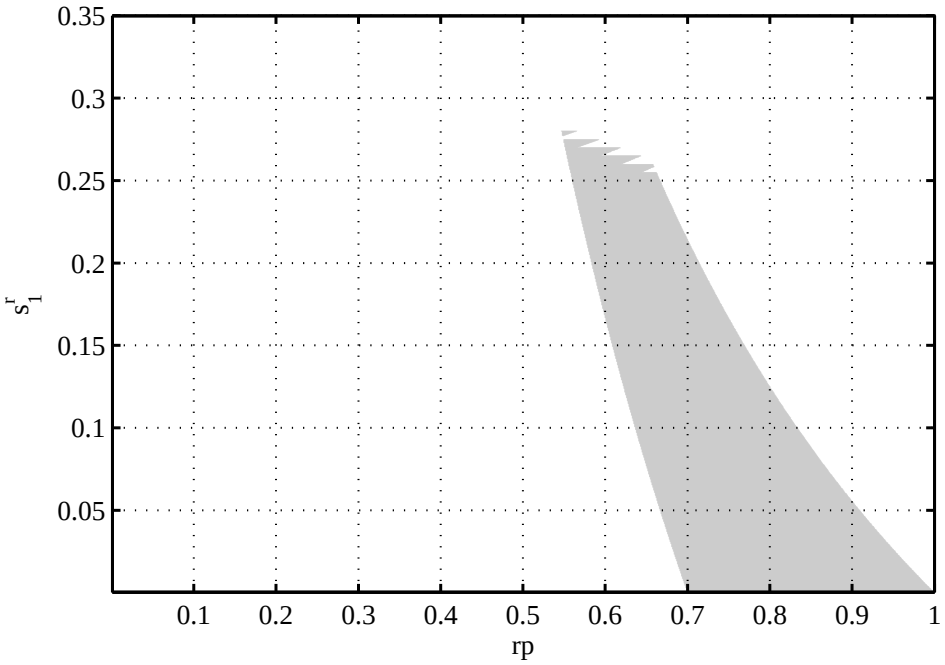

Fig. 3.27: Allowed values of rp and s^r_1 for the latest imposed conditions (the rotor power is limited with respect to the single stator powers).

3.4 Conclusions

This chapter analyses the possible poles pair values of the two machines in the D-DFIG configuration, with the corresponding slip range, considering also a wind power curve as

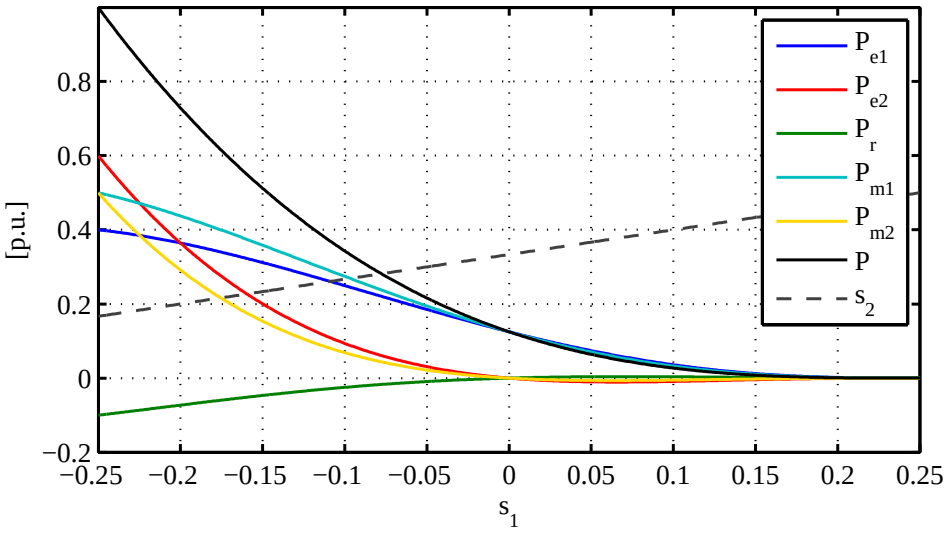

Fig. 3.28: Power flows with $s_1^r = 0.25$ and $rp = 0.\bar{6}$.

input. The analysis shows that several different values can be chosen to start a D-DFIG design, but that more condition must be set in order to obtain the required performances. The maximum slip ranges, for example, are very important to define rp.

The possibility of using positive and negative slip values for the first machine are limited by the powers loops in the system. This phenomena needs a deeper analysis in order to understand:

- if the machine stability is maintained in all the operating points;
- if the losses caused by the power loops are negligible or not;
- how much power is taken by the second machine at starting conditions, when the first machine is not delivering power.

On the other end, if only negative slip values for the first machine are used, no power loops are present but the range of available speeds is reduced.

A further limitation of P_r to be lower than $30\%P_N$ leads to a further limitation of the possible values for rp and s_1^r. This limitation was necessary in order to get closer to realizable DFIG designs.

Nevertheless, an interesting advantage of the D-DFIG configuration is that the power electronics rating is not proportional to the electrical nominal power P_N. It is possible to define P_r from the parameters rp and s_1^r, slightly decoupling it with respect to P_N and the maximum slip range. The range of slip, however, could be lower than a single DFIG configuration, in order to avoid over-sizing of the machines.

Chapter 4

THE D-DFIG DYNAMIC MODEL

The previous chapter was devoted to the analytical evaluation of the D-DFIG configuration, performing some simplifications in the formulation in order to obtain some easily readable results from a conceptual point of view. In this chapter, instead, the complexity of the analysis is increased because the D-DFIG is modelled in a dynamic way, using Simulink (part of Matlab®). The model is based on a set of equations closer to reality, although with some assumptions, but considering the energy required for the magnetisation of the DFIGs and the copper losses.

In addition to the dynamic model, a control strategy is required. The control strategy for a single DIFG is well known from the bibliography ([6],[7]), but the D-DFIG has not an already defined control strategy yet.

In short, the aim of the chapter is to build the model of the D-DFIG system and find a suitable control strategy. The analysis of the interesting operating points found in the previous chapters will be performed in the next chapter.

4.1 The dynamic model of a controlled DFIG system

The creation of a standard controlled DFIG system required different parts:

- a DFIG model;
- an A/D conversion for sampling the continuous machine signals into the digital domain;
- a block that estimates the stator flux position;
- a block that generates a PWM;
- PI controllers for the currents control;
- PI controllers for the power control.

The controllers include also voltage and current limitations, in agreement with the available DC-bus voltage and the maximum currents that can flow in the rotor windings. The schematic of the model is shown in Fig. 4.1, as described also in [8], [9], [10].

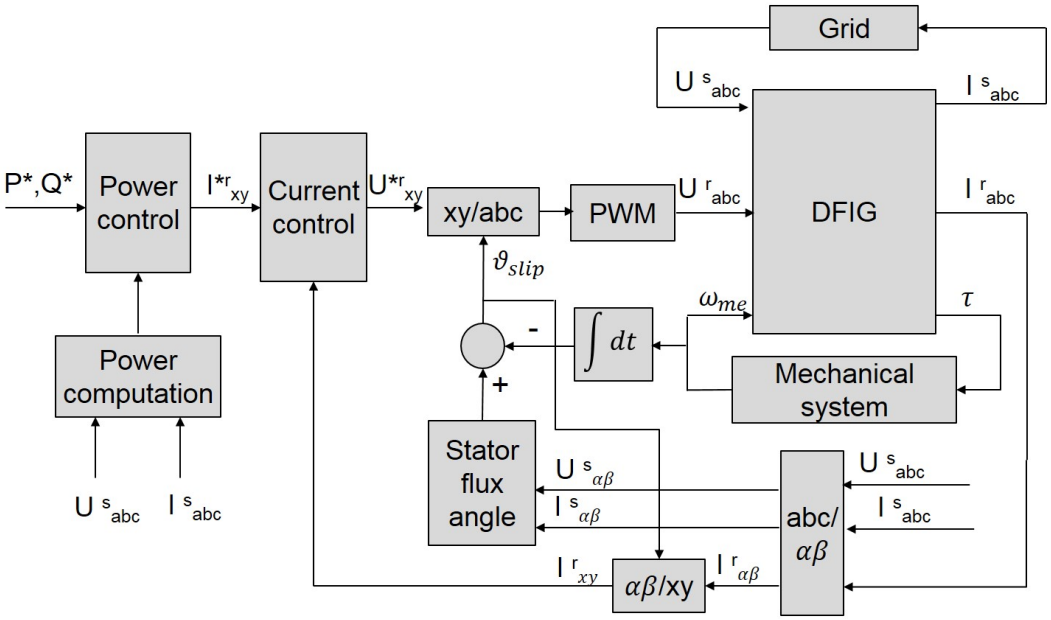

Fig. 4.1: The standard Field Oriented Control for the DFIG.

In this model, the decoupling of the d and q axis is not considered. The control of the rotor currents is performed through a Field Oriented Control strategy. The current references are generated through a power control block, which in the case of the D-DFIG system will be different with respect to the standard DFIG case.

Since the DFIG is connected to the grid and to a mechanical system, two blocks describing these systems are required. Those blocks will also be present in the D-DFIG model, with the correct electrical and mechanical connection models.

- the block that simulate the grid;
- the mechanical component of the machines.

The component that create the rotary electrical coupling is the DC-bs. Both the DFIG have a power converter for the modulation of the voltage applied on the rotor windings: in order to feed and to exchange energy between the two machine a component in DC voltage.

It is also worth underlining that several transformation blocks are necessary to convert the three-phase signals to the $\alpha\beta$ stationary reference frame and then to the dq rotating reference frame.

4.1.1 The single DFIG model blocks

The blocks are built considering the indications and suggestions of the technical bibliography [7], [8], [11] and [12].

Induction machine with wound rotor

The DFIG is modelled as an induction machine with wound rotor. The formulation is performed in a generic reference frame $d^x q^x$, obtained by using the Clarke and the Park

transformations, as described in the publication [13], where x means that the reference angle for the transformation is a generic angle θ_x imposed to the system. This formulation is similar to the equations (2.1) and (2.2), with the difference that the reference is on the $d^x q^x$ axes. Thus, the equations are:

$$\begin{aligned} v_{ds}^x &= r_s i_{ds}^x + \frac{d}{dt}\varphi_{ds}^x - \omega_x \varphi_{qs}^x \\ v_{qs}^x &= r_s i_{qs}^x + \frac{d}{dt}\varphi_{qs}^x + \omega_x \varphi_{ds}^x \\ v_{dr}^x &= r_r i_{dr}^x + \frac{d}{dt}\varphi_{dr}^x - (\omega_x - \omega_r)\varphi_{qr}^x \\ v_{qr}^x &= r_r i_{qr}^x + \frac{d}{dt}\varphi_{qr}^x + (\omega_x - \omega_r)\varphi_{dr}^x \end{aligned} \tag{4.1}$$

with ω_x the speed of the chosen reference frame and ω_r the electro-mechanical speed of the rotor. The flux linkage equations (2.3) are also valid in the generic reference frame:

$$\begin{aligned} \varphi_{ds}^x &= L_s i_{ds}^x + M i_{dr}^x \\ \varphi_{qs}^x &= L_s i_{qs}^x + M i_{qr}^x \\ \varphi_{dr}^x &= L_r i_{dr}^x + M i_{ds}^x \\ \varphi_{qr}^x &= L_r i_{qr}^x + M i_{qs}^x \end{aligned} \tag{4.2}$$

In the (4.1) and (4.2), the values of the rotor are not referred to the stator, and this is useful to directly compute the actual rotor currents. The choice of this reference frame has been made to achieve a higher degree of flexibility in the simulation models.

The inputs of the model 4.1 are the voltages of the stators windings, the voltages of the rotor windings and the speed of the rotor. The output are the currents of stator windings, the current of the rotor windings and the torque on the shaft, which is obtained as the cross-product of currents and fluxes. In order to keep the simulation as realistic as possible, the input and output connection of voltages and currents are realized by three-phase signals, and converted with the θ_x reference inside the machine block. A schematic of the machine model is showed in Fig. 4.2.

As in the real implementation, instead, the control works in a dq reference which might be different from the $d_x q_x$ reference. The digital control part is separated from the machine model by an inverter that converts a voltage space vector into a three-phase voltage sequence.The digital and the analog sides of the system are separated before and after the inverter.

Digital sampling and stator flux angle computation

An important aspect of the simulation is the digital sampling of the signals. The sampling time is defined as T_c and is equal to:

$$T_c = \frac{1}{4000} = 2,5 \cdot 10^{-3}\ [sec]$$

This value will also be used as the switching period of the inverter.

All the three-phase values of currents and voltages are sampled and converted in digital signals in order to be transformed by the application of the matrix $\boldsymbol{T}_{abc\to\alpha\beta}$ in the $\alpha\beta$ reference frame, or using the matrix $\boldsymbol{T}_{\alpha\beta\to xy}$ in order to get a reference for the control that allows to work with continuous signals [13]. The $\alpha\beta$ signals are used for the computation of the active and reactive power and for detecting the stator flux linkage position with the use of a phase-locked loop (PLL), which will be introduced in the next paragraph. The xy signals, instead, are used in the PI controls.

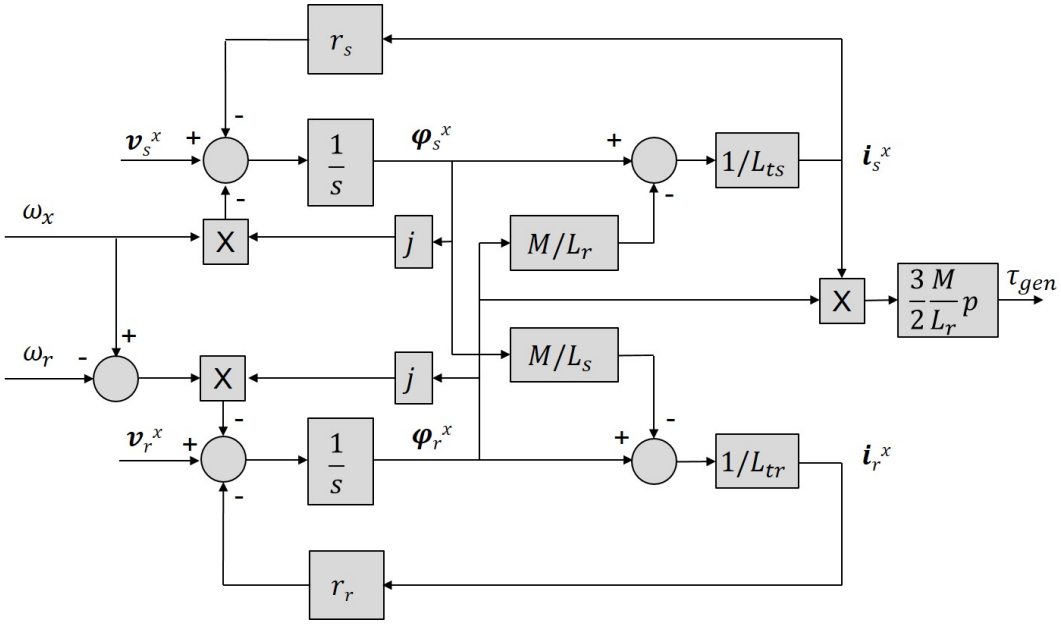

Fig. 4.2: Doubly-Fed induction generator model in the Laplace-transform domain.

Tranformations The following transformation matrices are used:

- $\boldsymbol{T}_{abc\to\alpha\beta0}$ and $\boldsymbol{T}_{\alpha\beta0\to abc}$ between the abc and the $\alpha\beta0$ reference frames:

$$\boldsymbol{T}_{abc\to\alpha\beta0} = \frac{2}{3}\begin{bmatrix} 1 & -\frac{1}{2} & -\frac{1}{2} \\ 0 & \frac{\sqrt{3}}{2} & -\frac{\sqrt{3}}{2} \\ \frac{1}{2} & \frac{1}{2} & \frac{1}{2} \end{bmatrix}$$

$$\boldsymbol{T}_{abc\to\alpha\beta0} = \begin{bmatrix} 1 & 0 & 1 \\ -\frac{1}{2} & \frac{\sqrt{3}}{2} & 1 \\ -\frac{1}{2} & -\frac{\sqrt{3}}{2} & 1 \end{bmatrix}$$

- $\boldsymbol{T}_{\alpha\beta0\to xy0}$ and $\boldsymbol{T}_{xy0\to\alpha\beta0}$ between the $\alpha\beta0$ and the $xy0$ reference frames, with θ_x the angle of the $xy0$ reference frame:

$$\boldsymbol{T}_{\alpha\beta0\to xy0} = \begin{bmatrix} cos(\theta_x) & sin(\theta_x) & 0 \\ -sin(\theta_x) & cos(\theta_x) & 0 \\ 0 & 0 & 1 \end{bmatrix}$$

$$\boldsymbol{T}_{xy0\to\alpha\beta0} = \begin{bmatrix} cos(\theta_x) & -sin(\theta_x) & 0 \\ sin(\theta_x) & cos(\theta_x) & 0 \\ 0 & 0 & 1 \end{bmatrix}$$

The value 0 of the $\alpha\beta0$ and the $xy0$ reference frames is not taken into consideration. The transformations are described in detail in [2] and [13].

The phase-locked loop The PLL computes the angle and the magnitude of a space vector $g_\alpha + jg_\beta$ defined by the signals in the $\alpha\beta$ reference frame. It is used in order to create the reference angle for the xy control reference frame. In this case, the control will align on the angle of the stator flux linkage vector.

This angle is initially calculated by calculating the back-electromotive force in the stator windings, which can be computed by knowing the value of R_s, $\mathbf{i}_{\alpha\beta s}$ and $\mathbf{v}_{\alpha\beta s}$. Since the angle refers to the back-electromotive angle, the stator flux linkage angle is obtained by subtracting $\pi/2$ to the calculated angle. In this way, an integrator of the back-electromotive force is avoided, removing possible issues with the output drift of the integrator in presence of small unwanted offsets in the input variables.

A schematic of the PLL is shown in Fig. 4.3. A transformation $\mathbf{T}^{\theta_s}_{\alpha\beta\to dq}$ converts the input variables into a fictitious dq reference frame, by using an angle θ_s which is initially unknown. In order to align the reference frame, the q axis component should be zero. A dynamic convergence to a correct alignment can be achieved by using a PI controller with the q axis component as input. The output of the PI regulator is the rotational speed of the reference frame, which can be further integrated to obtain the back-electromotive angle position. As mentioned earlier, the flux linkage angle is obtained by subtracting $\pi/2$. It is also worth to underline that in locked conditions the d axis component reveals the amplitude of the back-electromotive force, as the transformation is amplitude invariant. Therefore, by dividing the resulting d axis value by the calculated rotational speed of the reference frame, one can obtain an estimation of the stator flux linkage amplitude in steady-state conditions.

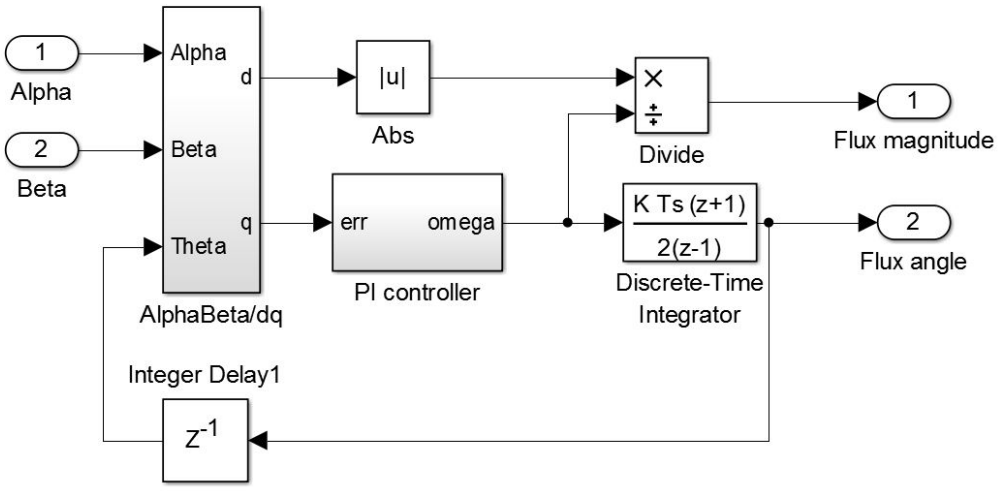

Fig. 4.3: Schematic of the PLL used in the system.

The inverter and the pulse-width modulation

The inverter translates the voltages defined by the controls into pulse-width-modulated signals through a proper modulation strategy. In this work, the inverter converters the digital signals from the control in voltages applied to the rotor windings.

The model of the inverter is composed by few blocks with different functions. A general

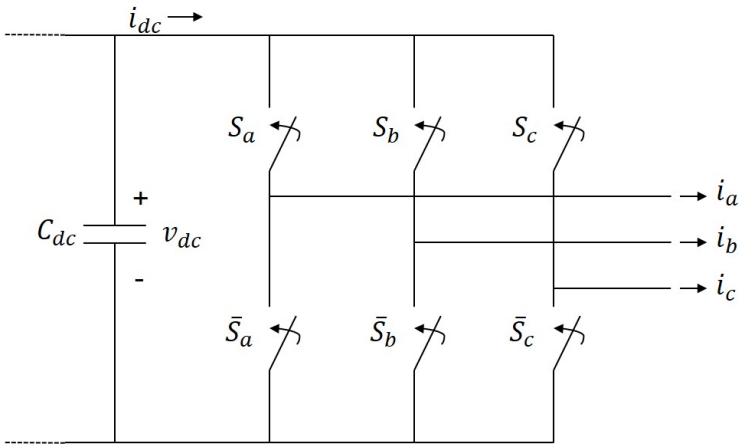

Fig. 4.4: The typical three phase inverter controled by PWM strategy.

schematic is shown in Fig. 4.5. The inputs are the voltage vectors in the xy reference coming from the control strategy, the angle θ of the rotating reference from and the DC-bus voltage V_{dc}. The outputs are represented by a sequence of voltages in the static abc reference of the rotor windings V_{abc}, a sequence of digital signals (0 or 1) for each IGBT in the inverter, indicating its status (open for 0 and close for 1), and two signals for the anti-windup process of the current control (not represented in Fig. 4.1 but used in the Simulink model as visible in Fig. 4.5 and described in the paragraph 4.1.1 at page 43).

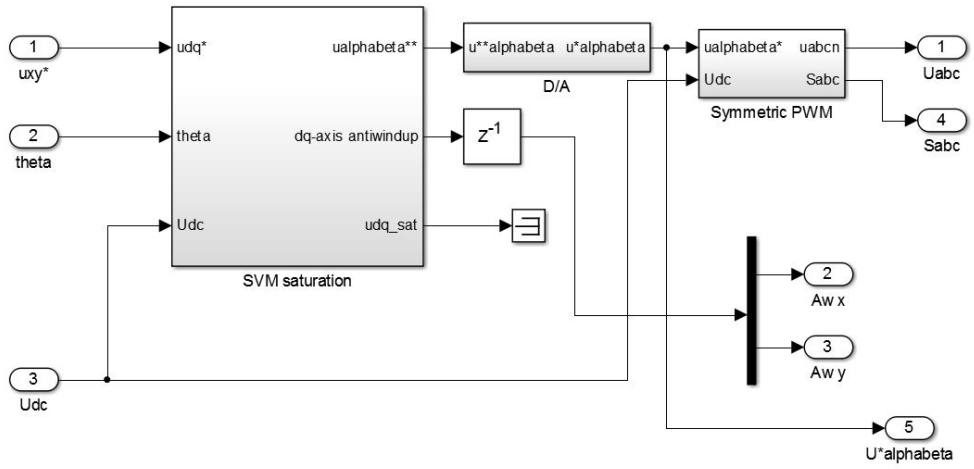

Fig. 4.5: Simulink blocks for the generation of the PWM signal.

The first block calculates the $\alpha\beta$ components from the xy ones. In case of voltage saturation, it is here that the anti-windup signals are generated for the current control.

The second block has the function of creating a delay of that simulates the delay of the computational time required by a real microprocessor. In absence of this block, the sampling of the current, the regulation and the new voltage outputs would be calculated at the same

time by Simulink. By introducing a small delay (of $T_c/2$ for example), and then sampling the signals again every T_c, the new output signals are not anymore applied at the same instants of the new sampled data, but only one control cycle after that as it happens in reality.

The third block processes the voltage vector $\mathbf{v} = v_\alpha + jv_\beta$ to generate a symmetric space-vector modulation in output. All timing calculations and the generation of the square wave signals is performed in this block. The output is represented by three square-wave signals representing the *abc* voltages, considering the calculated IGBT state (which is also brought in output as S_{abc} and the available DC-bus voltage.

As mentioned before, the PWM switching is kept at the same period of the sampling time T_c. For the sake of simplicity, the simulation does not include IGBT dead times used to avoid short circuit between the IGBTs on the same inverter leg.

The FOC applied to the DFIG

The field oriented control applied for the DFIG is the one that aligns to the stator flux linkage, also known as *PQ* control and well explained in the paper [7]. With this choice, the reference frame xy is such that the axis x is aligned with the stator flux linkage and does not contribute to the torque of the machine and thus the active power. On the contrary, acting on the y axis will change the reactive power Q_s. This is very useful since the machine is connected to the grid. A schematic of the implemented control is shown in Fig. 4.6.

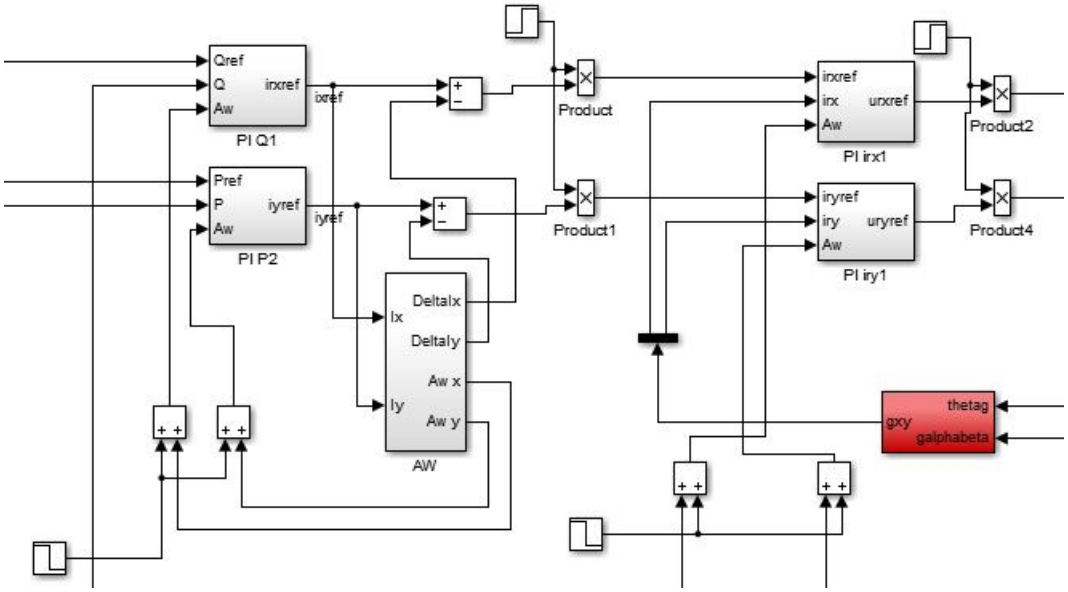

Fig. 4.6: The implemented control of the DFIG. The output signal is connected with the PWM. The Anti-windup sistem and the blocks for their activation are visible.

The current control The control of current is performed by a conventional proportional-integral action. Both x and y axes have their separate controller, as visible in Fig. 4.6. A schematic of the implemented current regulators is shown in Fig. 4.7.

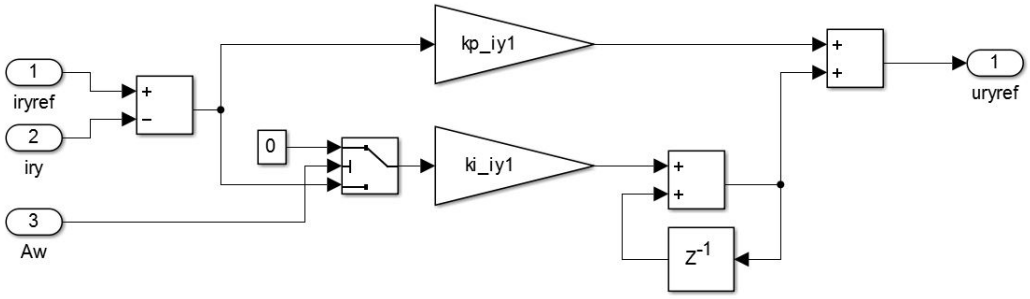

Fig. 4.7: The PI current control for the y axis (the x axis has the same structure).

Anti-Windup of current control The only interaction between the xy axis current controllers is given by the saturation of the PWM modulation and the consequent anti-windup action. This is because the saturation could induce a reduction of the voltage components on both axis.

The anti-windup start its action when the Aw signal, in Fig. 4.7, is equal to 1. As mentioned before, this signal comes from the PWM saturation block shown in Fig. 4.5. When equal to 1, the anti-windup stops the integrator to receive more input values, thus blocking the integral action until the anti-windup signal is turned back to zero. This is a simple and known method to avoid unnecessary overshoots and wind-up problems in the output of the PI regulator.

The power control The power control is composed by similar elements as the current control, using PI regulators. The inputs are the references for the active and reactive power, as well as the actual ones. The output are represented by the current references for the y axis (from the active power regulation) and for the x axis (from the reactive power regulation).

The other difference with respect to the current regulation is that the anti-windup approach needs a different approach. Fig. 4.6 shows how the active and reactive power controls deal with the anti-windup signal, and how the limitation of the current is implemented in the control system.

Limit of current and Anti-Windup of the power control The limitation of the current and the generation of the anti-windup signals for the power controllers is shown in Fig. 4.8.

The basic idea is that the current cannot exceed a certain predefined value, which can be split over the x and the y axes with the actual transformation angle. Those maximum allowed values are compared with the reference current outputs from the power controllers. In case one or both are exceeding the maximum allowed values, the anti-windup flag Aw_x and/or Aw_y is raised and sent to the power controllers. At the next available control cycle, as it was happening for the current regulation, the integral part of the controllers will be blocked, until the anti-windup flag will be turned back to zero.

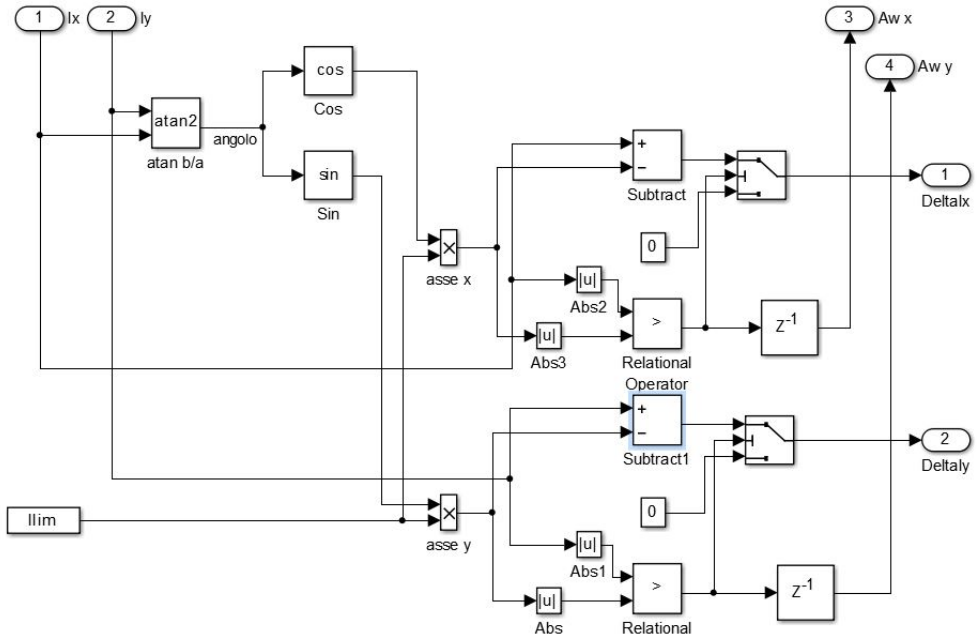

Fig. 4.8: Current limitation on the current reference signals from the power controllers, and generation of the anti-windup signals. This is the AW block of the Fig. 4.6.

Grid model

A grid model could be created in two ways, both described in [7]. One model used the voltages in the machine stator as input and the currents as output. This is the same one applied in [11]. The second model uses the currents as input and the voltages as output. This second option is chosen for this work.

The schematic of the model is shown in Fig. 4.9, which requires an estimation of the resistance R_{grid} and inductance L_{grid} of the grid side.

Mechanical system model

The literature discusses different ways of simulating mechanical systems for wind power applications. In [11] a mechanical dynamic model that consider mechanical losses, the inertial coefficient matrix and the stiffness matrix of the rotor is developed. This model can take into account the presence of a gear box and it is basically a multi-mass model. The model is also completed with the introduction of oscillations on the machine shafts due from the mechanical resonances of the wind tower system.

Another viable solution is the exploitation of a pre-made S-function block that computes the torque on the shaft obtained from the wind speed and the blade pitch. The National Renewable Energy Laboratory, and American institute for the research on renewable energy sources, developed the models for wind generation ([12] and [5]), making the Simulink block available to the interested people.

In this work, a simple single-mass mechanical dynamic model was created, considering that the major focus of the work is to understand the basic working principles of the D-DFIG system. The model is shown in Fig. 4.10. A speed reference is given to a PI controller

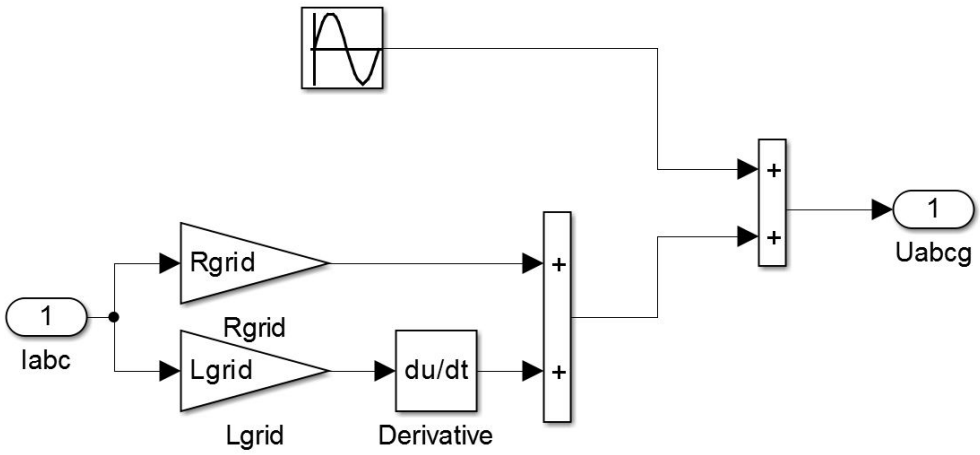

Fig. 4.9: Grid model used in the D-DFIG model

that simulates the energy delivered on the mechanical system from the wind rotor. The torque is added to the torque from the DFIG and the total torque is used to calculate the mechanical speed, through a transfer function that considers the inertia and viscous friction of the system.

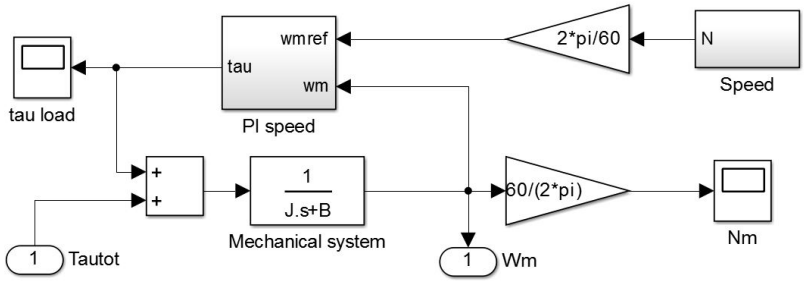

Fig. 4.10: Mechanical system model used in the D-DFIG simulations.

4.2 The dynamic model of a Double-DIFG configuration

After the creation of a DFIG model and the definition of a control system for the single machine, the D-DFIG configuration is taken in account. Since the D-DFIG is a new topology, there seems to be no available literature on the control of this configuration. The first important part to discuss relates to the coupling between the two machines.

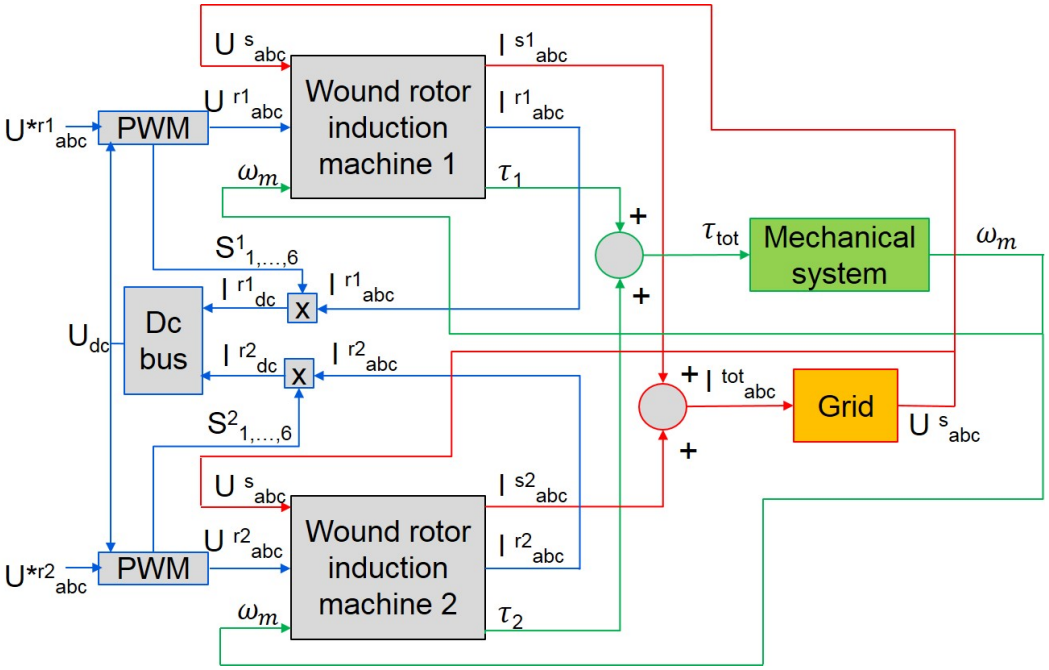

Fig. 4.11: Schematic of the couplings between the two DFIGs. Green colors represent mechanical connections, red colors represent grid connections, blue colors represent connections through power electronics on the rotor side.

4.2.1 Machines coupling

For understanding the coupling of the two machines, it is necessary to consider the D-DFIG topology in Fig. 3.1 at page 12. The topology has three connections where the energy flows: the connection through the grid connection and the shaft, the connection through the grid and the rotor electrical connection (the inverters) and the connection through the rotor connection and the shaft. Modeling these connections is required.

Two of these blocks are already present in the model of DFIG. The connection to the grid and the source of mechanical power are already defined by the blocks visible in Fig. 4.1 at page 38. The electrical connection between the machines is obtained by adding the stator currents in order to represent the parallel connection of the stator windings, while the sum of the torques represents the mechanical connection between the machines through the shaft. The remaining connection to be modeled from scratch takes care of the electrical connection through the inverters on the rotor side.

The Simulink blocks implementing the connections is shown in Fig. 4.11, where the green color is used for the mechanical connection, the red color for the grid connection and the blue color for the rotor windings/power electronics/DC-bus connection.

Dc Bus

Given that the inverter models are represented by the schematic in Fig. 4.4, the truly connection between the rotor windings of the two machines is made through the DC bus. The DC Bus block takes as input the currents from the rotor windings $I_{abc,r}$ and the command

signals of the IGBTs $S_{1,\dots,6}$, giving as output the DC voltage on the bus V_{dc}. The schematic of the block is shown in Fig. 4.12.

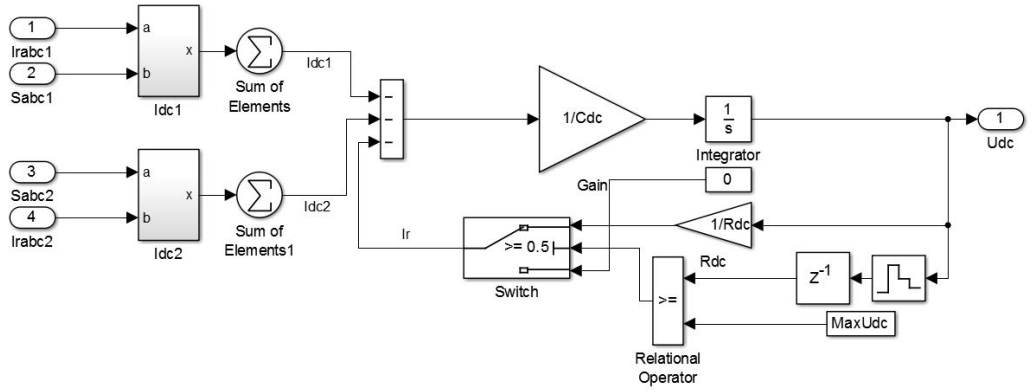

Fig. 4.12: DC-bus model with voltage limiter for avoiding overvoltages.

The opening and closing signal of each phase are multiplied with the rotor current of the same phase, in order to obtain a current signal which reflects the current flowing in the DC bus. $I_{dc,1}$ and $I_{dc,2}$ refer to the DC-bus current contributions from the two machines. The values are added (subtracted in Fig. 4.12 only for a pure convention choice) and fed to the model of a capacitor with a capacitance value of C_{dc} a. The value of U_{dc} represents the DC-bus voltage.

A limiter is applied on the DC-bus voltage, as visible in Fig. 4.12, in order to prevent overvoltages. The limiter is composed by a switch that shunts the current on a resistance when the capacitor voltage is over a limit $MaxU_{dc}$.

4.2.2 The complete control strategy for the D-DFIG configuration

The control of the D-DFIG is primarly composed by the separate current regulation for both machines, with an outer layer of control for the active power P.

The first analytical evaluation of this configuration, as described in the chapter 3, is carried out only for the active power. In the analytical considerations, the reactive power can not be taken in account, but in a dynamic simulation it is not negligible. However, for easiness of simulation, the reactive power of the two machines is kept to zero.

Fig. 4.13 shows a possible control strategy for the D-DFIG with two separate, parallel regulators for the power. This configuration needs the computation of the active and reactive power of the single machines and the references of power for both machines. The computation of the power does not represent an issue, while the creation of the correct references is a more difficult operation which would include a sharing map, accounting also for the losses in the windings.

The drawback of the schematic in Fig. 4.13 goes back to the formulation in the chapter 3, especially considering 3.1.1 at page 14. The rotor power is a function of the stator power and the slip, but since the machines are coupled there exists only one correct condition for splitting the power between the machines. In the real system, this means that the power flowing inside the DC bus is equal to the power flowing out from the DC bus, keeping the capacitor voltage at the same level. The analysis in the chapter 3 is performed for lossless

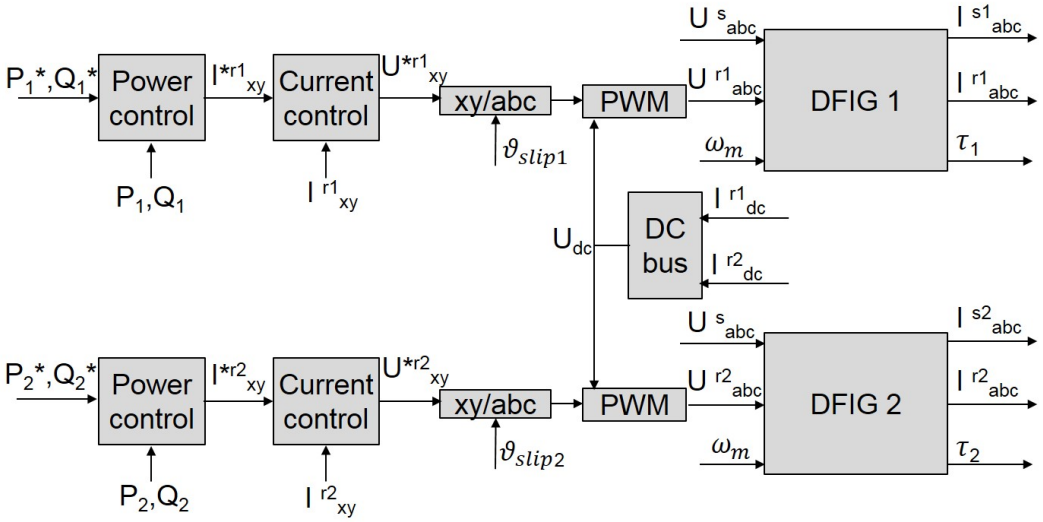

Fig. 4.13: First control solution for the D-DFIG topology.

conditions, but real operation include also the losses in the windings - and this should be taken into account when splitting the power references between the two machines, in order to keep the DC-bus charged in the correct way. However, computing the power references by considering the contribution of the losses (which may vary as function of the stator resistance, too), is not a robust way to approach the problem. An error in the computation of the power references would translate in a variation of the power flowing in the DC bus, with a consequent divergence of the DC-bus voltage towards zero or over the maximum voltage limits.

A possible solution is the creation of two different control loops, with different references. In this proposed case, the **first** machine is defined as the **master** machine, while the **second** machine is defined as the **slave** machine. The schematic of the proposed solution is shown in Fig. 4.14.

The master machine receives the total D-DFIG power as input, while the slave machine obtains its power reference from an outer DC-bus voltage controller which aims at the stabilization of the DC-bus voltage.

With the design conditions defined in the chapter 3, the first machine is the one with less pole pairs, and which works every time with the same sign of power flowing on the stator side. Thus, with the power flows defined as in Fig. 3.1, the power flowing out from the stator windings of the first machine is always positive in generation mode. By convention, this is selected as the master machine.

The second machine, instead, follows the total power reference by contributing to the DC-bus voltage control at a predefined voltage value. In this way, the power flowing from the master machine into the DC bus is also the power flowing out from the other side, towards the second machine (selected as slave), reaching the voltage equilibrium and finding the solution of the power flow problem.

Summarizing, the control solution for the D-DFIG system is composed by two control levels:

- a total power control for the first (master) machine;

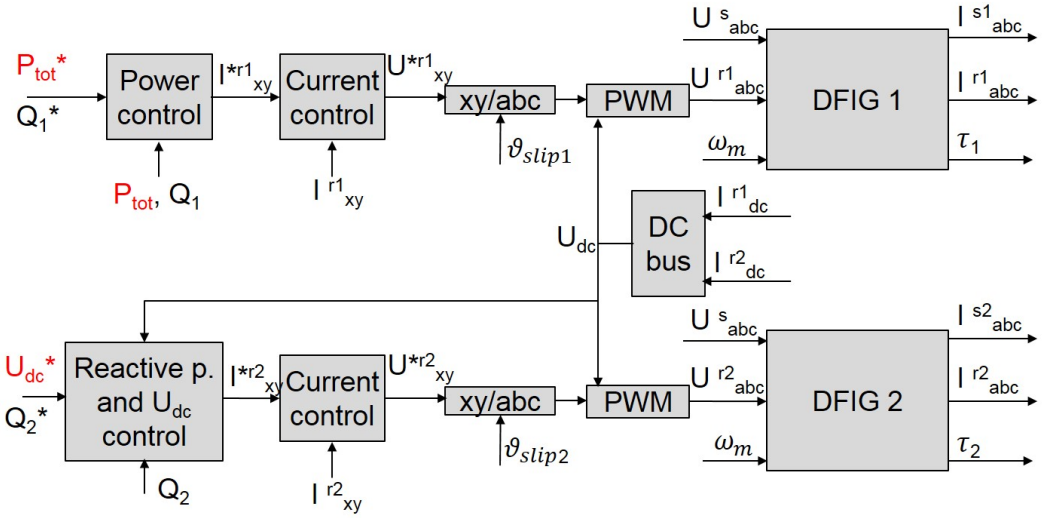

Fig. 4.14: Second control solution for the D-DFIG topology, with a master machine and a slave machine.

- a DC-bus voltage control for the second (slave) machine, which indirectly generates a power reference.

The total power reference generator

For the generation of the total power reference shown in Fig. 4.14, a Simulink block is created as in Fig. 4.15.

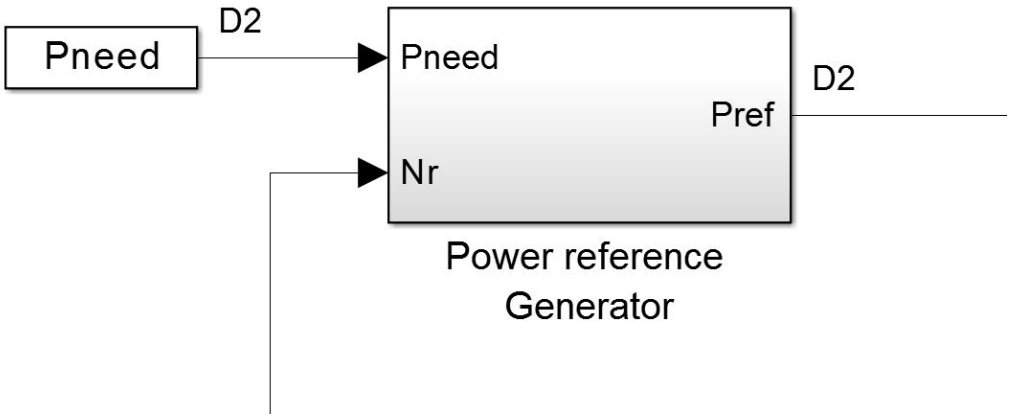

Fig. 4.15: The power reference generator.

The input is the rotor speed N_r and the grid power request P_{need}. The output is the active power reference for the PI control of the y axis of the master machine. The power reference is generated by following the typical wind power curve shown in Fig. 3.7 and

described in the paragraph 3.3 at page 19. The formulation used in the block is the one discussed in section 3.3.1 at page 20. Fig. 4.16 shows the process of the reference generation, controlled with respect to the cut-in speed N_{in} and the rated speed N_{rate}. The used equation is the 3.12 at page 20.

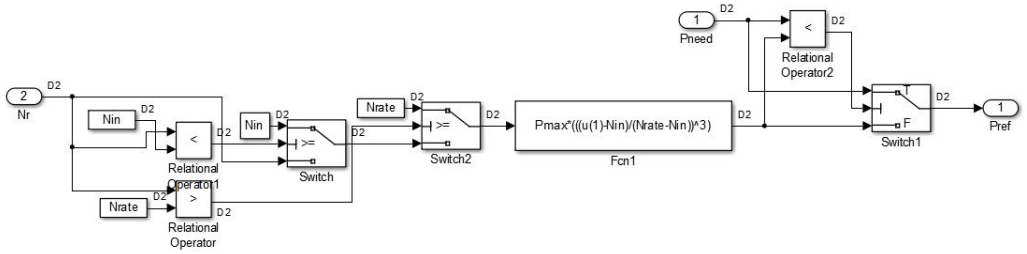

Fig. 4.16: Detailed schematic of the power reference generator.

DC-bus voltage regulation issues

Due to the variable source of voltage/power from the rotor windings, a stable DC-bus voltage regulation is challenging. It was found that the optimal PI parameters for a low-speed condition were not working well for high-speed conditions. Therefore, a dynamic PI regulation was applied, as shown in Fig. 4.17. The proportional coefficient $k_{pU_{dc}}$ is kept constant, while the integral coefficient is variable and inversely proportional to the slip of the master machine s_1.

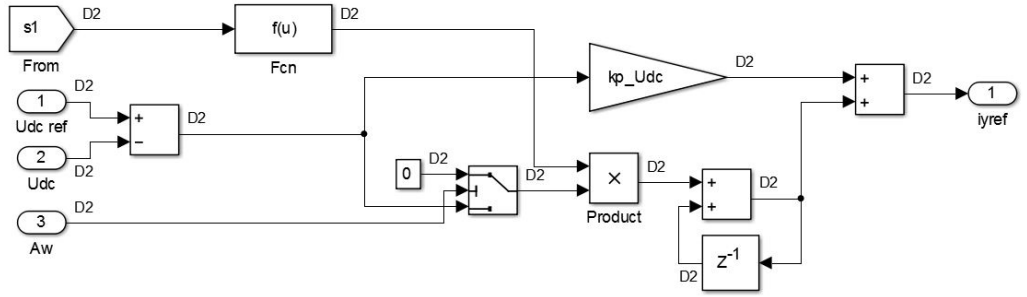

Fig. 4.17: The DC bus control for the y axis reference of the slave machine.

4.3 Conclusions

The Simulink model of the D-DFIG configuration was defined, starting from the model and control of a single DFIG. A control strategy that allows the simultaneous generation of power for the two DFIGs was described. The model was developed with the following simplifications:

- the mechanical system does not simulate a real wind rotor system but it keeps the rotor speed at a constant imposed reference;
- the mechanical system does not take in account the elasticity of the shaft, since it is a one-mass model;
- the inverters do not consider dead times and switching losses;
- the DC-bus does not contribute with losses.

In the following chapter, different simulations of the D-DFIG configuration are performed to validate both the analysis of the topology and the proposed control structure.

Chapter 5

SIMULATIONS OF THE D-DFIG TOPOLOGY

The simulation on the model described in the previous chapter is now carried in order to validate its theoretical analysis and the proposed control strategy.

5.1 The simulated D-DFIG configuration

The D-DFIG design values used in the simulation are reported in the last result of the Chapter 3, in Fig. 3.28 at page 36. The chosen design values are the following:

- $rp = 0.\bar{6}$;
- $s_1^r = 0.25$.

The rp value suggests the value of the pole pairs of the machine: a reasonable value of pole pairs are $p_1 = 3$ and $p_2 = 2$. As shown in Fig. 3.28 at page 36, the power on the machine shaft are the same for both machines, while the power on the stator windings of the second machine is higher than that of the first machine. The power through the rotors is the 10% of the D-DFIG maximum power, and is the 25% of the stator power of the second machine. It means that the second machine limits the possible range of slip of the first machine between the values of ± 0.25, following the law of the DFIG rotor power 2.10 at page 7.

5.1.1 Machine parameters

The power rating of the simulated total D-DFIG system is 5 MW, which is a common value for the analysis of offshore wind turbines. As a matter of fact, a 5 MW wind generator and turbine system analyzed by the NREL in [12] and [5] is typically used as a standard reference for the simulation of offshore wind turbines.

The chosen values for rp and s_1^r returns the nominal power of the single DFIGs. Therefore, the first machine 1 has a nominal power value of 0.4 $p.u.$ of the total D-DFIG system power, while the machine 2 is responsible for the 0.6 $p.u.$ of the D-DFIG nominal power. For a total nominal power of 5 MW, the machine 1 nominal power is therefore 2 MW and the machine 2 nominal power is 3 MW. The parameters of the chosen machines are shown in Tab. 5.1.

Tab. 5.1: Parameters of the machines.

Parameter	**Value machine 1**	**Value machine 2**	**Unit**
U_n	690	690	$[V]$
P_n	2	3	$[MW]$
p	3	2	$[-]$
R_s	$1.57e^{-3}$	$1.04e^{-3}$	$[\Omega]$
R_r	$2.94e^{-3}$	$2.51e^{-3}$	$[\Omega]$
$L_{\sigma s}$	$0.08963e^{-3}$	$0.0828e^{-3}$	$[H]$
$L_{\sigma r}$	$0.0695e^{-3}$	$0.0604e^{-3}$	$[H]$
L_m	$8.001e^{-3}$	$8.085e^{-3}$	$[H]$

5.1.2 DC-bus parameters

Fig. 4.12 at page 48 shows that several parameters in the DC-bus model need a value. These parameters are the value of the capacitance of the DC-bus capacitor, the resistance value of the shunt resistance for discharging the over-voltage and the voltage limit for the definition of the over-voltage condition and the starting of the shunt action. Moreover, the value of the voltage reference for the DC-bus voltage control is necessary, as shown in Fig. 4.14 at page 50. These values are reported in Tab. 5.2.

Tab. 5.2: Parameters of the DC-bus model.

Parameter	**Value**	**Unit**
U_{dc}	690	$[V]$
C_{dc}	$115e^{-3}$	$[F]$
R_{dc}	0.5	$[\Omega]$
U_{dc}^{max}	900	$[V]$

5.2 Simulation results

Several different simulations were carried out in order to evaluate the basic operation of the D-DFIG as well as the validation of the theoretical analysis. The following simulations were performed:

- the rotor speed is a ramp between 750 rpm and 1250 rpm, with the power that the turbine rotor can transfer on the electrical side following a cubic curve, as in figure 3.7, starting from zero at the cut-in speed. The power request from the grid is the maximum power deliverable by the system;

- the rotor speed is a ramp between 750 rpm and 1250 rpm, with the power that the turbine rotor can transfer on the electrical side following a cubic curve, as in figure 3.7, starting from 1% of the nominal power P_n at the cut-in speed. This variation of cut-in power is managed by the power reference generator described in the paragraph 4.2.2 at page 50. The power requested to the grid is the maxim power that deliverable by the system;

- three power step proofs where the rotor speed is kept constant. Initially the power request P_{need} from the grid is zero, at an instant $t_{step} = 5.5s$ the power request has a step and at $t_{step} = 7s$ the power request is even imposed null.

5.2.1 Speed ramp simulation

The applied speed ramp is shown in Fig. 5.1; the ramp starts at $t = 5\,s$ from $750\,rpm$, and ends at $t \approx 25\,s$ at $1250\,rpm$. Fig. 5.2 shows the variation of total power flows that the D-DFIG delivers to the grid. The speed ramp shows that the synchronous speed of the first machine is reached and passed at $t = 15\,s$.

Fig. 5.2 shows the total power flowing outside the D-DFIG P_{tot}, the power flowing outside the single machines, P_{e1} and P_{e2}, and the power through the rotors and the DC bus P_r. It is important to remember that the analytical evaluation was considering lossless machines, while the dynamic model takes in account also the copper losses in the stator and rotor windings (Fig. 4.2). Therefore, the the total mechanic power flowing inside the system is named P, while the total electric power flowing to the grid is named P_{tot}.

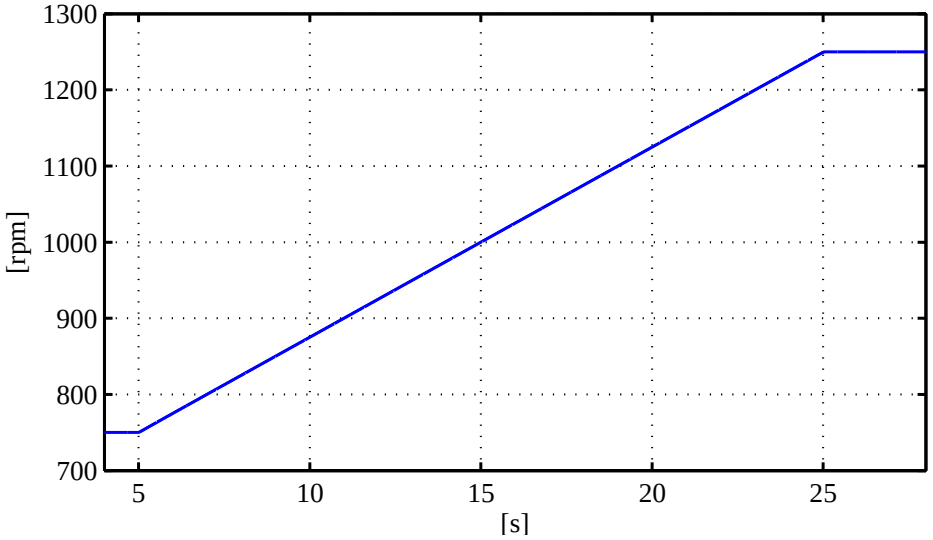

Fig. 5.1: Speed ramp, starting from $750\,rpm$ to $1250\,rpm$, applied in the simulations.

Fig. 5.2 shows that the power values of the single machine have large oscillations that added together return a low oscillation in P_{tot}. These oscillations are located at the starting point of the ramp at $t = 5\,s$ and after the rated speed point, where the rotor reaches $1250\,rpm$, therefore it is believed that the oscillations appear because of the rapid (instantaneous, in this simulation) reference variations. The rotor power P_r also presents an oscillation after reaching the rated speed, somehow caused by the power oscillation from the stator windings. The total power reaches the value of $5\,MW$ at $1250\,rpm$.

DC-bus voltage

Fig. 5.3 shows the variation of the DC-bus voltage U_{dc} during the speed ramp. At time $t = 5\,s$ the voltage on the DC-bus is $690\,V$. The instantaneous speed change produces a

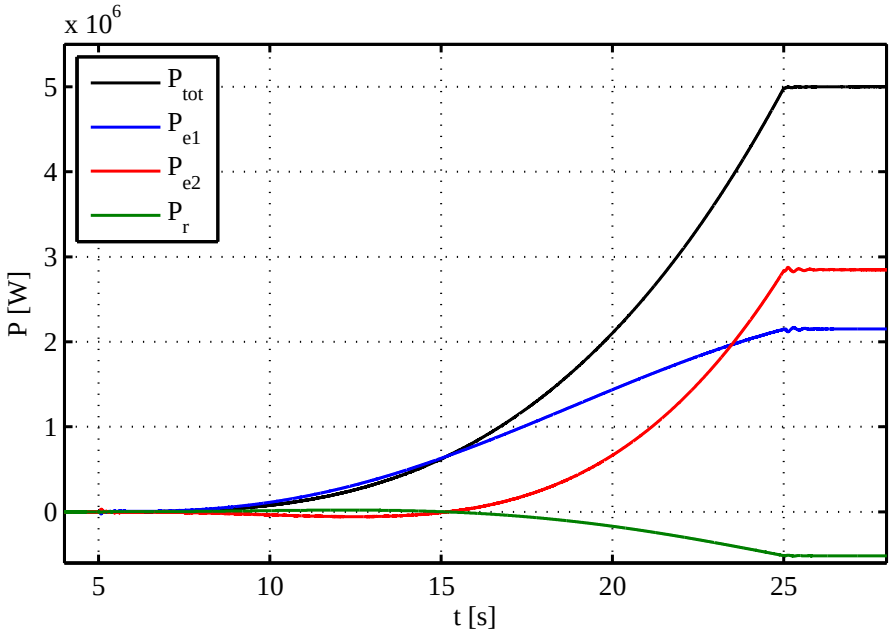

Fig. 5.2: Power curves in the time domain.

voltage drop mitigated by the controller. At $t = 25s$ the speed is kept constant and the DC-bus voltage goes back to 690 V, after some oscillations. It is important to observe that the DC-bus voltage goes to values lower than 690 V in the sub-synchronous mode of the first machine, while it goes to higher values when the first machine works in the super-synchronous mode. This is related to the rotor power flow: the first machine needs rotor power during sub-synchronous operation, while it delivers power in the super-synchronous mode. The voltage remains every time in the range between 660 V and 740 V and the overvoltage shunt system is never activated on in this simulation.

System losses

The losses in the machines are computed from the model in the time domain. Fig. 5.4 shows the value of the power losses during the simulation. The curves P_1^{lost} and P_2^{lost} are the sum of stator and rotor power losses in the machine 1 and the machine 2. These values are computed considering the square of the current magnitude in the windings, each multiplied by the corresponding resistance value. P_{tot}^{lost} is the total power lost in the D-DFIG system, $P_{tot}^{lost} = P_1^{lost} + P_2^{lost}$. The curve defined with $P - P_{tot}$ is the curve computed form the difference between the value of the mechanical power flowing through the shaft, defined as P, and the total electric power flowing to the grid, defined as P_{tot}.

It is worth to note that the losses P_1^{lost} and P_2^{lost} of the first and second machine follow the variation of the stator powers. The lost power in the machine 2 is higher than that of the machine 1.

In order to better validate the computation of the lost power, the total lost power is also computed in a different way. In Fig. 5.4, the light blue curve represents the values of $P - P_{tot}^{lost}$, where P is the total mechanic power. This value combines different powers flows: the mechanical losses loss due to friction and, the total electric losses and the DC bus losses.

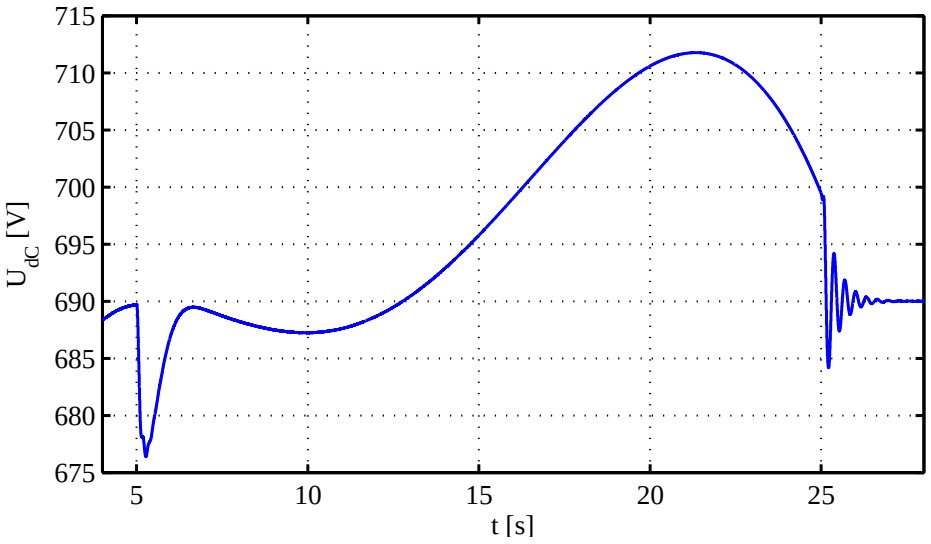

Fig. 5.3: U_{dc} variation between $t = 4\ s$ and $t = 15\ s$.

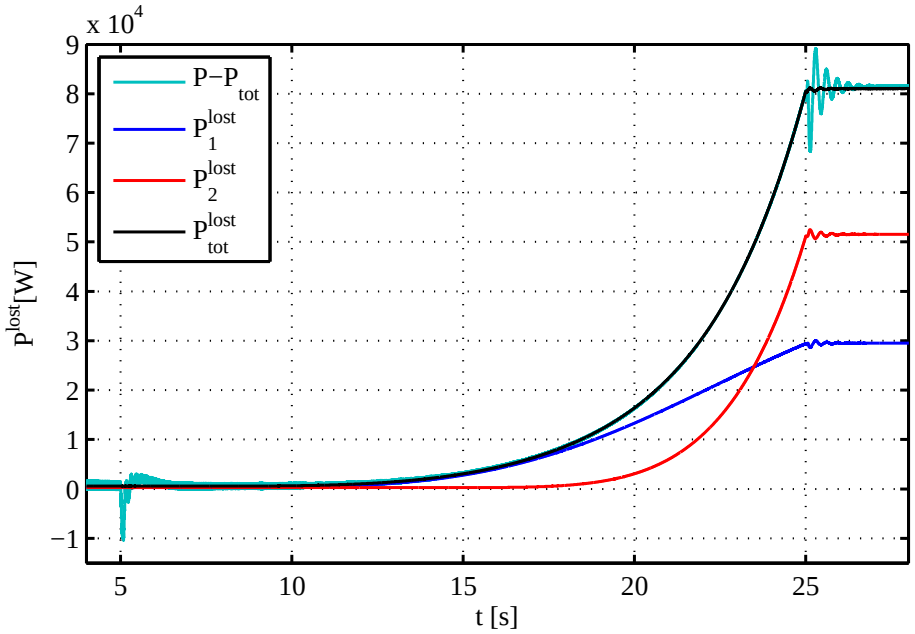

Fig. 5.4: System losses in the D-DFIG configuration.

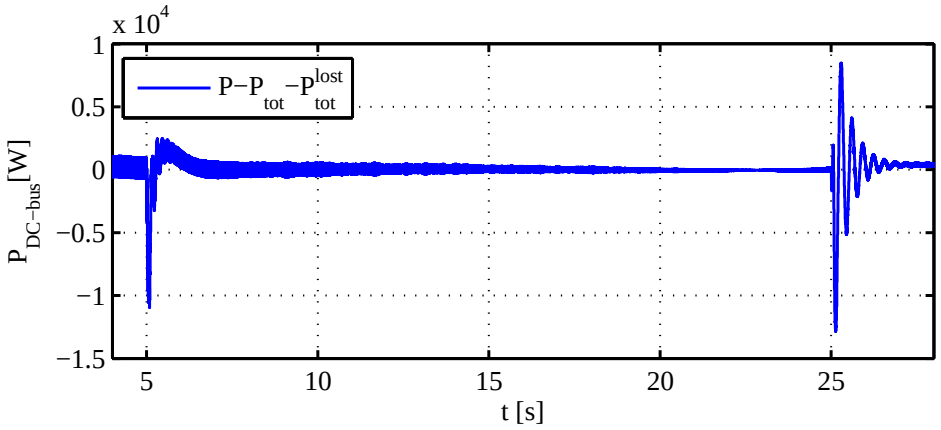

Fig. 5.5: Power flowing inside the DC-bus.

Since the mechanical losses are negligible and the DC bus is modeled as a lossless system, the value of $P - P_{tot}^{lost}$ is practically overlapping to the electrical losses calculated from the resistive contributions, confirming the correct computation.

DC-bus power losses

Considering a negligible contribution of mechanical losses, it is possible to calculate the power losses in the DC bus, as shown in Fig. 5.5. The curve is always around zero, meaning that the controller keeps an equilibrium between the incoming and the outgoing power.

Power curves in the slip domain

The above reported graphs are in the time domain, while the analytical evaluation was performed in the slip domain. It is possible to transfer the curves in the slip domain to compare the analytical results, as done in Fig. 5.6 and Fig. 5.7. The continuous curves are from the simulated model, while the dashed curves are obtained from the analytical approach of the equations (3.7), (3.8) and (3.9) at page 14, with $P = P_{tot}$.

Fig. 5.6 shows that there is a slight difference between the analytical and simulated curves. The simulated electrical power P_{e1} is higher in the simulated version, while the value of P_{e2} is higher in the analytical version. In both cases, anyway, the total power respects the value of P_{tot}. The power flowing through the DC bus looks similar in both cases.

Fig. 5.7 considers only the values of the rotor power. The graph shows that the simulated value has a very little difference with respect to the analytical curve. The values are equal when the stator windings of the two DFIG deliver the same power to the grid, around $s_1 = -0.2$. The simulated values near $s_1 = 0.25$ have a large oscillation due to the system oscillations, also visible in other graphs. The maximum value of power through the rotor, computed in the simulation, is $10.32\% P_n$.

Fig. 5.8 reports the difference between the analytical and simulated power curves. The values with the * are from the analytical curves. Although the first and the second machine curves present errors of different sign, these two curves have the same sign for the entire the slip working range. The maximum error is approximately $\sim 150kW$ for the first machine and $\sim -150kW$ for the second machine. The difference of the rotor power curves $P_r - P_r^*$ is very

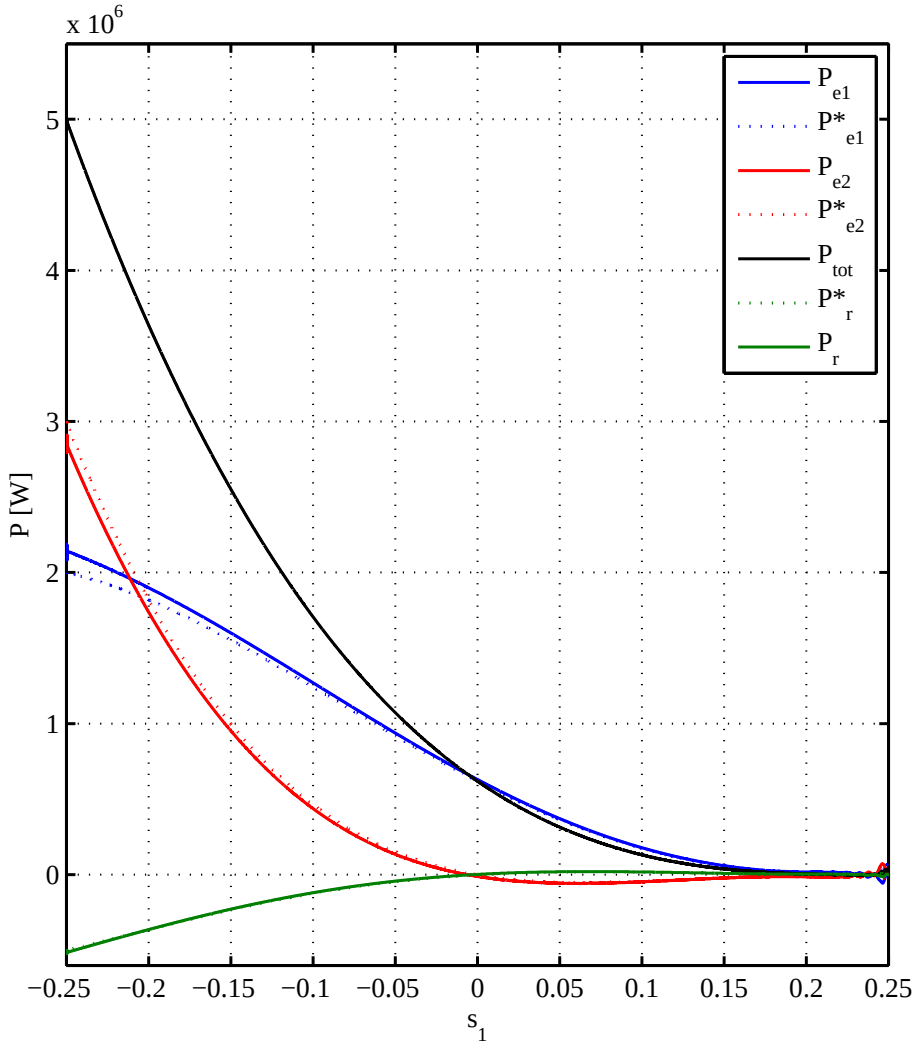

Fig. 5.6: Power curves in the slip domain.

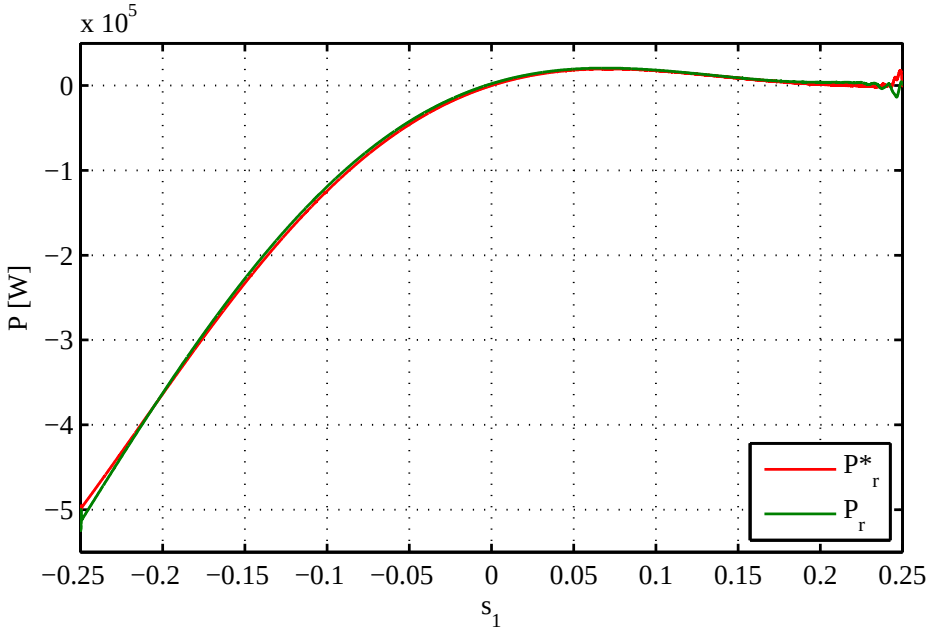

Fig. 5.7: Rotor power curves in the slip domain.

low and has a sign change for $s_1 \approx -0.2$. The maximum value of $P_r - P_r^*$ is approximately $\sim -15kW$.

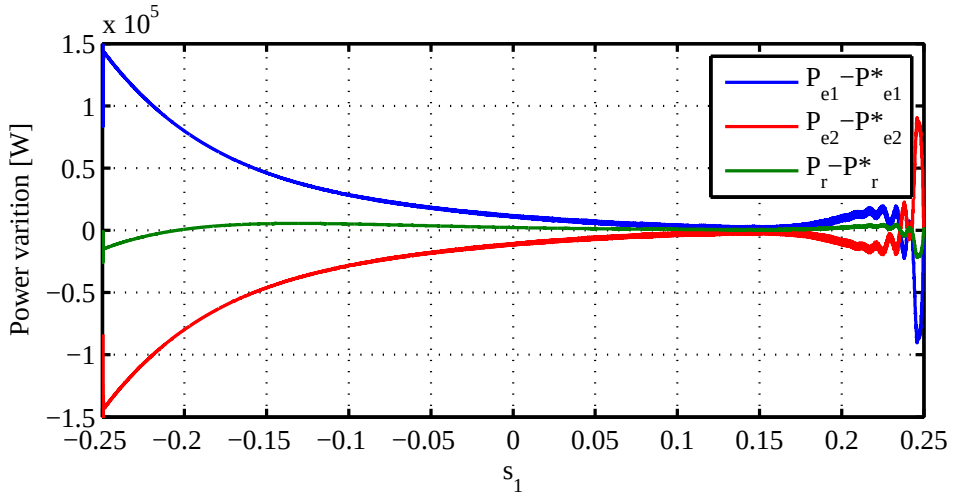

Fig. 5.8: Difference between the analytic and the simulated power curves.

Power loops

As discussed in the section 3.3.1 at page 25, for high values of slip s_1, when both machines works in sub-synchronous mode, there are two loops in the machine, described in Fig. 3.17.

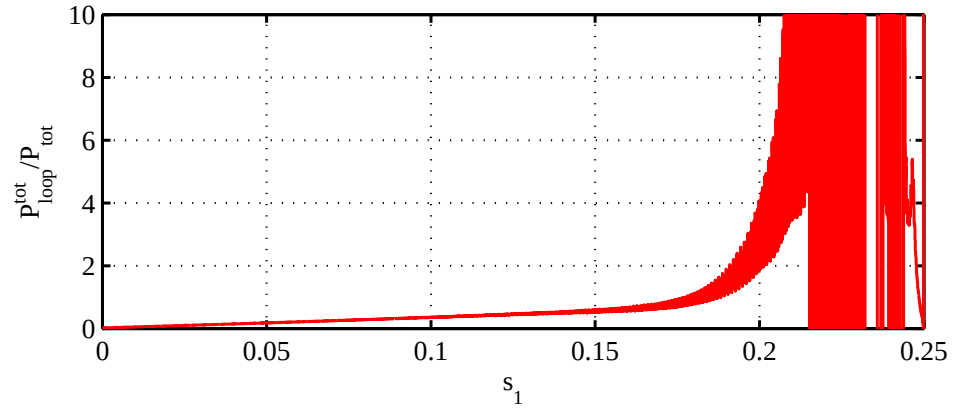

Fig. 5.9: Total loop normalized with respect to the total power flowing to the grid.

In Chapter 3, the analysis was performed with the assumption of lossless machines. In the simulation, at least copper losses are present and their impact can be analyzed.

The total power loop is shown in Fig. 5.9 in the slip domain. The data extracted from the model suffers of noise for high slip ranges, which is related to the cut-in speed speed of the generator (which is subjected to non-negligible oscillations, as shown before), but the average trends of the curve shows that the loop reaches values higher than P_{tot}beyond $s_1 \approx 1.75$.

Efficency of the D-DFIG system

The efficiency of the system is affected by the loop power and its related losses. Fig. 5.10 shows the calculated efficiency, with some noise issues related to the oscillations at cut-in speed. In any case, the rapid drop of efficiency after $s_1 = 0.15$ is the effect of the increase of loop power with respect to the total power towards the grid. On the other hand, the efficiency value for slips between -0.25 and 0.15 is higher.

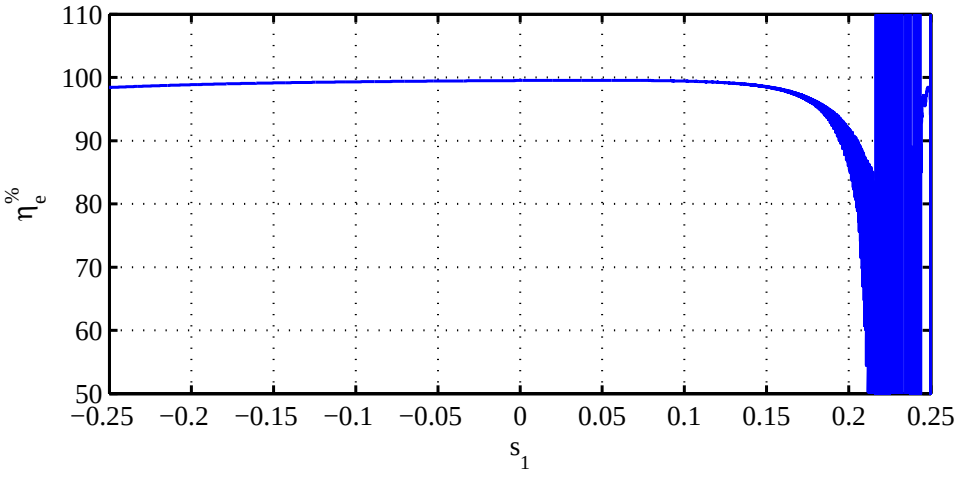

Fig. 5.10: Efficiency of the D-DFIG configuration.

The zoom of the efficiency region between 95% and 100% is shown in Fig. 5.11: there is a large region of slips where the efficiency is over 98%. The highest efficiency $\eta_e^{\%}$ is reached around $s_1 = 0.05$ with a value of 99.5%. For slips lower than $s_1 = 0.05$, the efficiency decreases to $\eta_e^{\%} = 98.5\%$ at $s_1 = -0.25$.

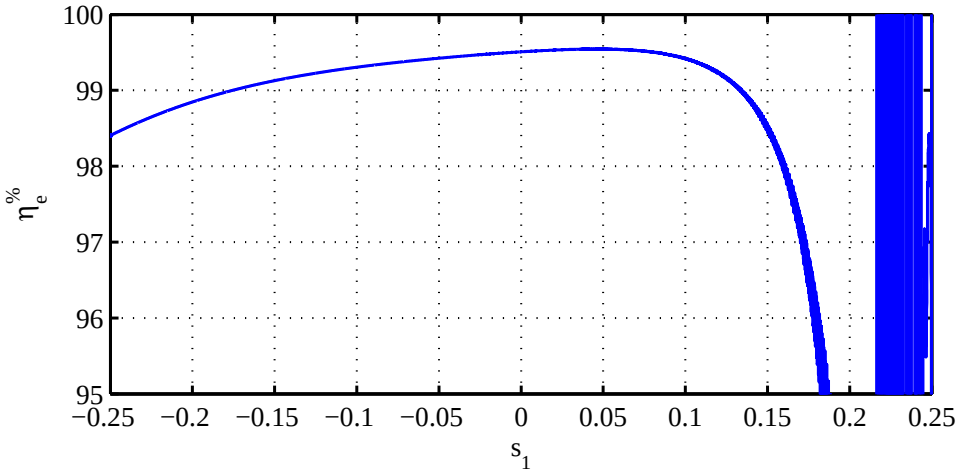

Fig. 5.11: Efficiency of the D-DFIG, zoomed between 95% and 100%.

5.2.2 Speed ramp simulation with initial power P_{cut-in}

From the description in 3.3.1 at page 25, it is clear that the power loops might be a source of troubles if not properly analysed. One problem with the previous simulation is that the power on the shaft is zero for the cut-in speed: in this condition, the calculation of the ratio between the loop power and the output power suffers of numerical singularities. Since in real conditions the wind turbine rotor will start at the cut-in speed with a non-zero power on the shaft, a power step is added to the wind power curve, solving at the same time the singularity issues. The power step is set to be $1\%P_n = 50\,kW$ is carried out.

Fig. 5.12 shows the results in the time domain. The values of power at maximum speed are the equal to the values of the precedent simulation. Some oscillations are visible at the cut-it speed. in the starting instants are visible, oscillation even due to the acceleration changing.

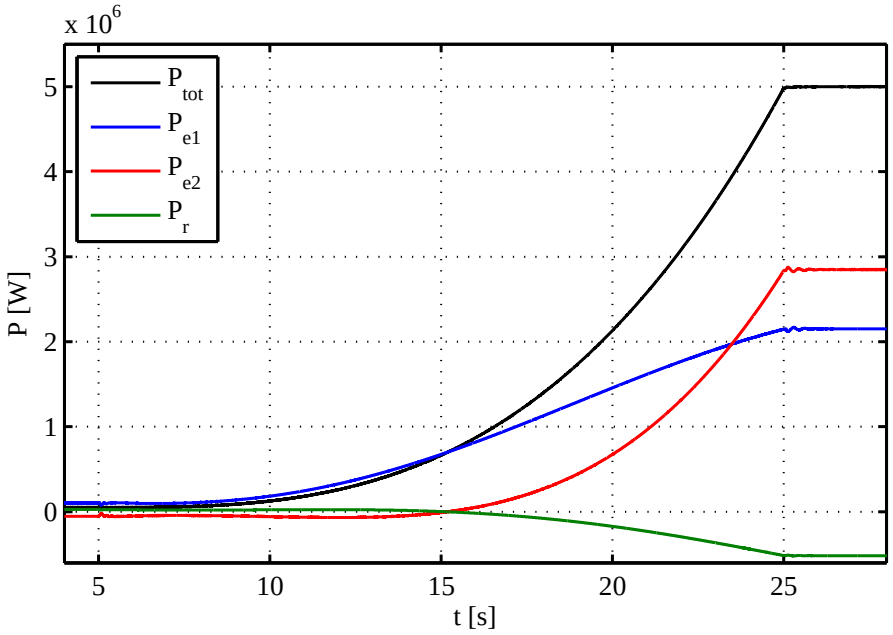

Fig. 5.12: Power curves of the D-DFIG, with an initial power of $1\%P_n$ at cut-in speed.

Fig. 5.13 shows the curve of the DC-bus voltage during the simulation. There are not sensible differences with respect to the other DC-bus curve at page 57, rather than the controller seem to work slightly more efficiently because the power through the second machine is higher with respect to the first simulations, thus there is more rotor power for the DC-bus control.

The power curves in the time domain are converted in the domain of the first machine slip s_1 in Fig. 5.14, in order to have a clear comparison with the analytical power curves. The curves show the same difference as in the previous simulations. For slip values near 0.25, similar oscillations are present.

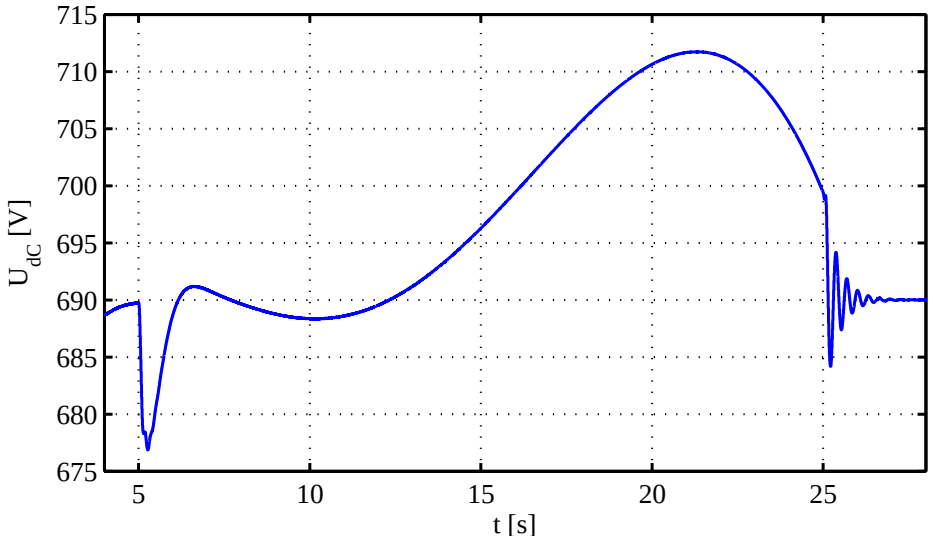

Fig. 5.13: DC-bus voltage curve.

Power loops

The power loops seem to have less influence on the system when $P_{cut-in} \neq 0$. In Fig. 5.15, it is possible observe that the ratio between the total loop P_{loop}^{tot} and the total power flowing out the machine P_{tot} is kept under 1.5 and there is a large range where $\frac{P_{loop}^{tot}}{P_{tot}}$ is under 1. In this condition, the loop has a lower impact from the efficiency point of view, but it is not negligible.

Efficiency of the D-DFIG system

Fig. 5.16 reports the efficiency of the D-DFIG system with the new power curve. The high slip values are affected by oscillations but the value of efficiency is over 98.5% for every s_1 value. The maximum efficiency point is still obtained for s_1 around 0.05, and for lower slip values $\eta_e^{\%}$ starts to decrease because of the increased power through the stator windings.

$\mathbf{P_{cut-it}}$ optimal value

As it was found that the efficiency of the D-DFIG system is affected by the value of the cut-in power, different simulations with different values of the cut-in power were performed, plotting the total system efficiency in the s_1 working range in Fig. 5.17. The values in the legend are related to the value of P_{cut-in} in percentage of the nominal power P_{nom}. It is worth to note that with a value of $P_{cut-in} = 0.5\%P_{nom} = 25\,kW$ the efficiency is over 97.5% in the complete slip range. The efficiency increases for higher percentages and starts to decrease beyond $2.5\%P_{nom} = 125\,kW$.

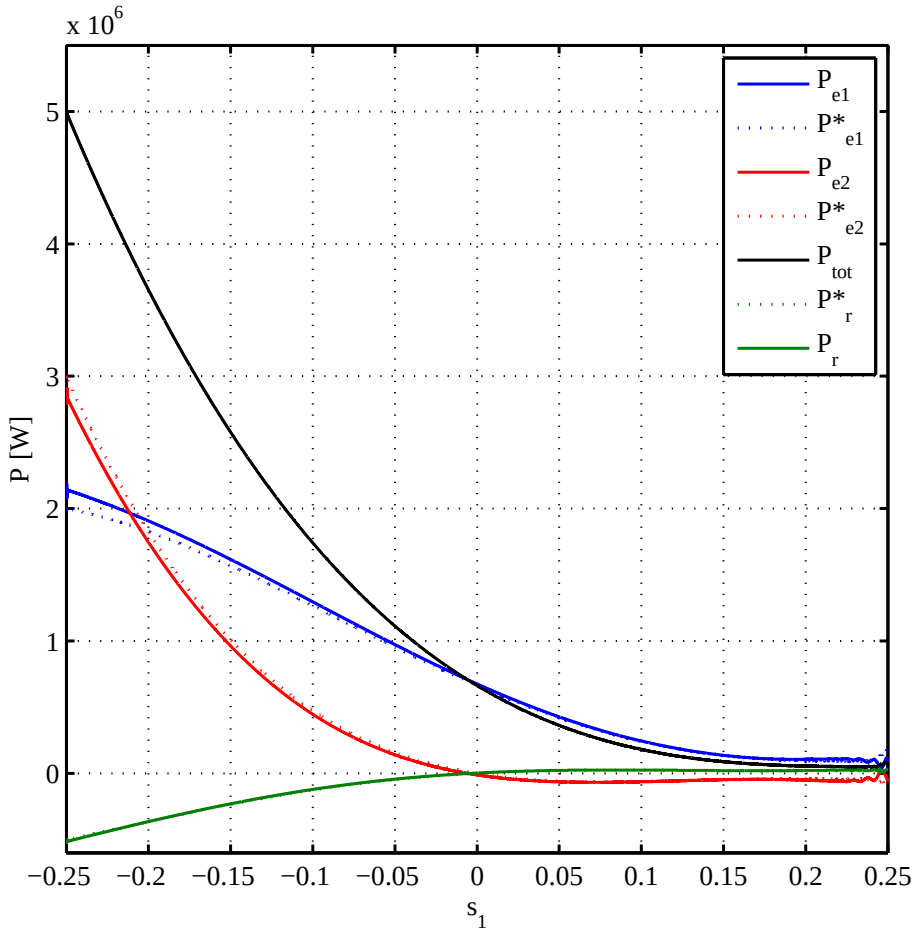

Fig. 5.14: Power curves of the D-DFIG in the slip domain, with an initial power of 1%P_n at cut-in speed.

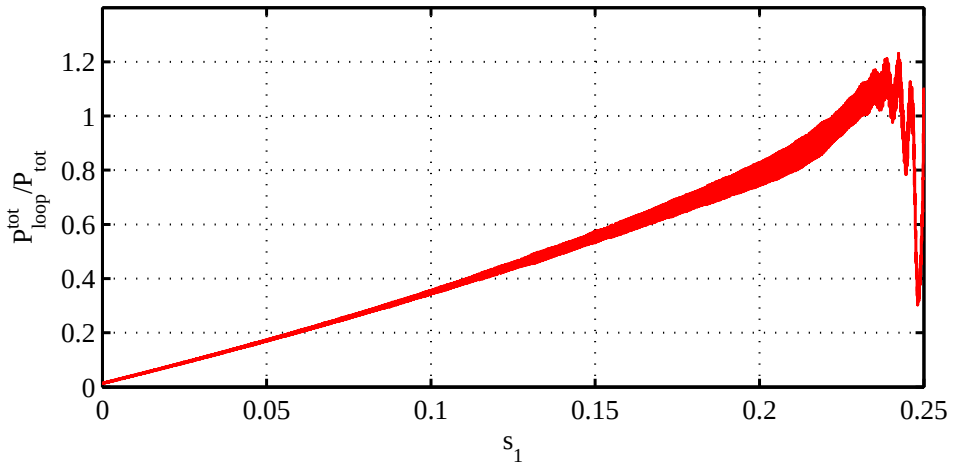

Fig. 5.15: Loop ratio of the D-DFIG, with an initial power $1\%P_n$ at cut-in speed.

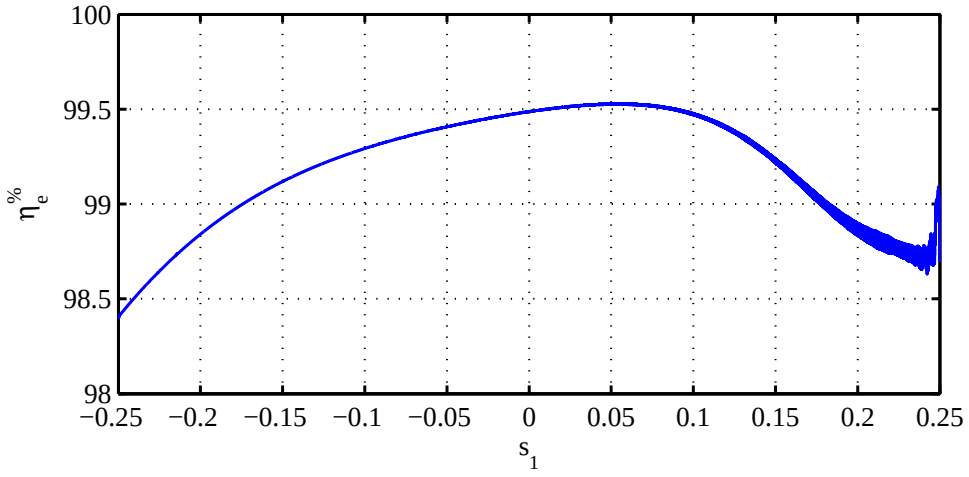

Fig. 5.16: Efficiency of the D-DFIG, with an initial power $1\%P_n$ at cut-in speed.

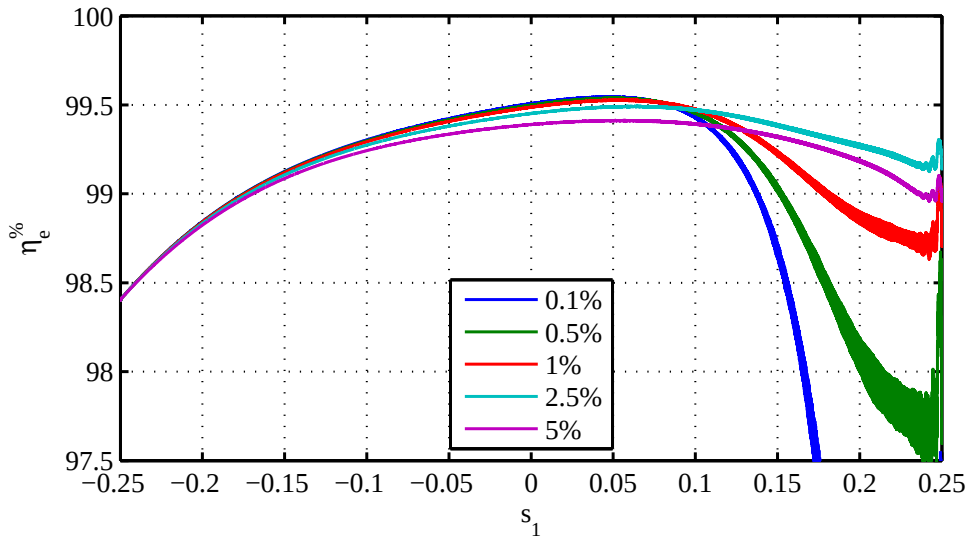

Fig. 5.17: Efficiency curves for different P_{cut-in} in percentage of P_{nom}.

5.2.3 Power step

The last simulation investigates the step response of the system. Three power steps are tested: one in sub-synchronous mode, one in super-synchronous mode (referred to the slip s_1) and the last one with the slip condition that allows $P_r = 0$. Obviously, in the sub-synchronous mode the shaft power is lower with respect to the one in super-synchronous mode. The reaction of the DC-bus controller is also different. The shaft speed however is kept constant (but different for the two modes) during the complete simulation.

Power step: sub-synchronous mode for s_1

The first power step simulation is performed at $N = 950\,rpm$, where the slip of the first machine is kept constant at $s_1 = 0.05$ and the the slip of the second machine is $s_2 = 0.3$. Both s_1 and s_2 are positive, so power loops are present and the stator powers have different signs, as shown in Fig. 5.18 (the first machine works as a generator and the second machine as a motor).

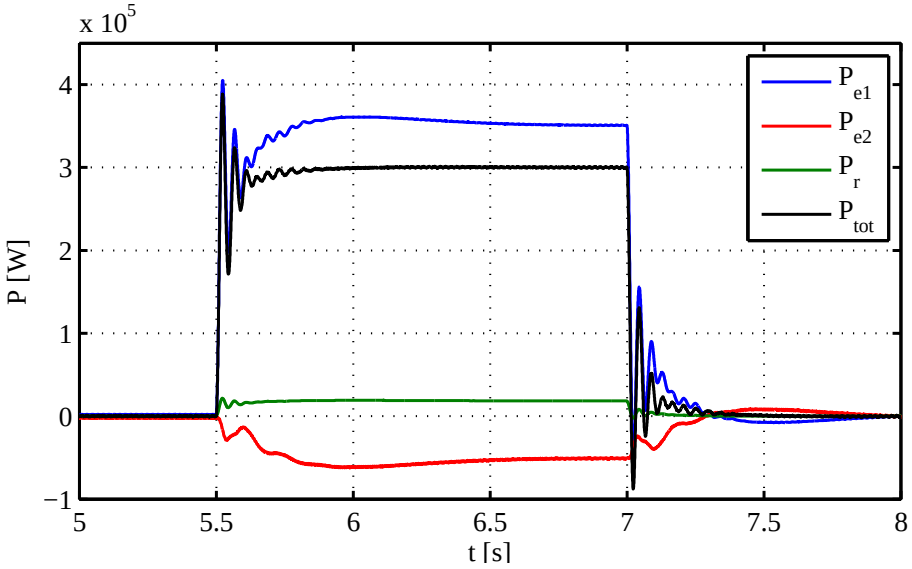

Fig. 5.18: Power-step response of the system in sub-synchronous mode.

The power request is $300\,kW$ at $t = 5.5\,s$ and returns t zero at $t = 7\,s$. The machine 1 is the faster than the machine 2, because the latter follows the regulation of the DC-bus voltage. The total power P_{tot} is stable in less than $0.5\,s$. The power delivered from the single machines is stable after $1\,s$, and their sum gives a stable P_{tot} but P_{e1} and P_{e2} are involved in a few oscillations.

The DC-bus oscillation during the power step is shown in Fig. 5.19. When s_1, $s_2 > 0$ the power through the rotor is flowing outside the machine 2 and inside the machine 1, which is considered as positive following the convention defined in Chapter 3. When the power has a rapid increase, the machine 1 need power from the rotor and the DC-bus voltage decreases, as visible in Fig. 5.19 after $t = 5.5\,s$. After the reduction of the DC voltage, the action of the machine 2 starts and the DC-bus voltage increases. When the P_{tot} goes back to zero the opposite conditions occur, where the DC-bus voltage is increased by the machine 1, and controlled and kept to $690\,V$ by the machine 2.

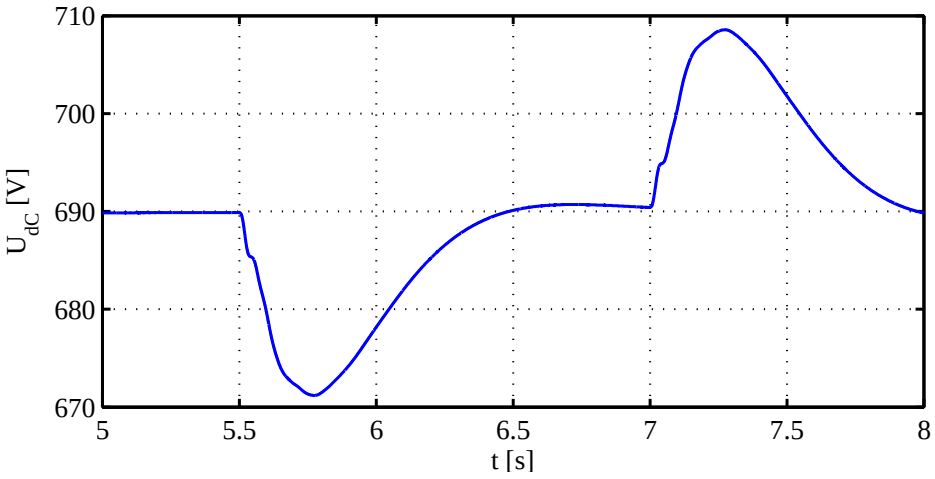

Fig. 5.19: Power-step response of the DC-bus in sub-synchronous mode.

Power step: super-synchronous mode for s_1

The simulation with s_1 in super-synchronous mode is performed at $N = 1200\,rpm$. The power available on the shaft is more than half of P_{nom}, and the chosen power step is 2.5 MW. The step is applied at $t = 5.5\,s$ and the power turns back to zero at $t = 7\,s$. Fig. 5.20 shows the curves of this simulation.

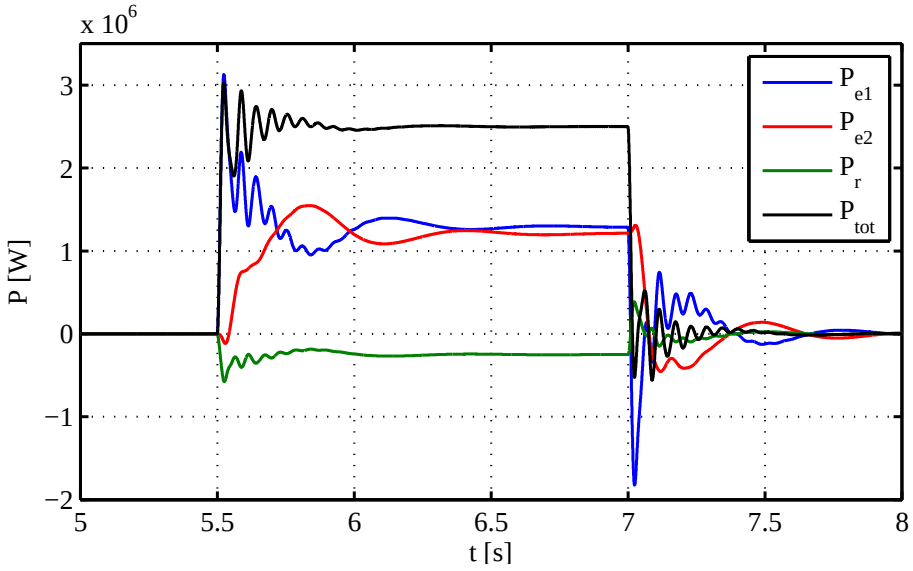

Fig. 5.20: Power-step response of the system in super-synchronous mode.

As in the previous simulation, P_{e1} is the fastest growing power. The slips have a different sign now, as $s_1 < 0$ and $s_2 > 0$, thus both DFIGs work as generators and the power P_r is defined as negative.

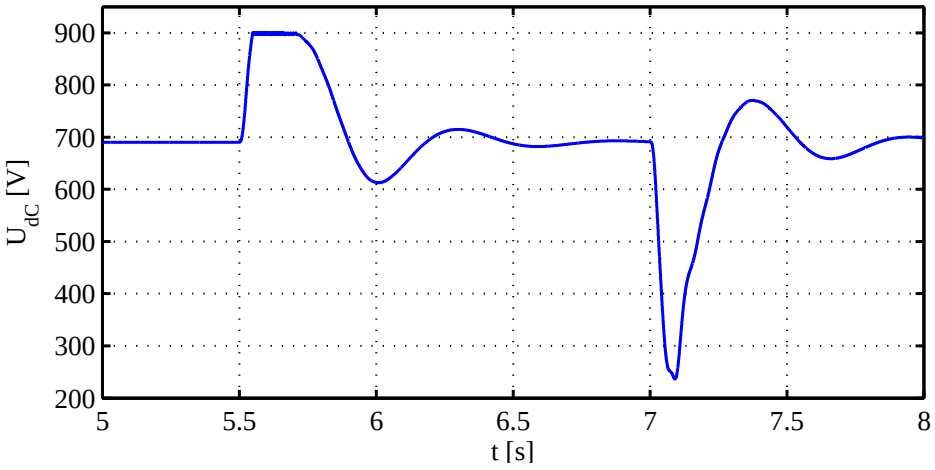

Fig. 5.21: Power-step response of the DC-bus in super-synchronous mode.

The total power reaches the requested value in less than 0.5 s, but P_{e1} and P_{e2} need more time in order to reach an equilibrium. It is interesting to observe that when the power request goes to zero, P_{e2} is positive since the machine 2 control is slower then the machine 1 control. P_{e1} gets negative for the time required for the DC-bus voltage control to activate the machine 2, in order to keep P_{tot} around zero.

Another interesting aspect is shown in Fig. 5.21, which reports the DC-bus voltage curve. During the power step, the power flowing outside the rotor of the DFIG 1 is positive. Because of the large step value, the power flowing out of the rotor is enough to increase the DC voltage over 900 V. The voltage limitation system is activated and the excess power is discharged the on a resistance, keeping the maximum voltage at 900 V. Even in this condition, the DC-bus voltage control is able to reduce the voltage back to the reference. Another important point is the DC voltage drop during the negative step of power. The DC voltage reaches $\approx 250\,V$: despite the very low value, the machine is excited and it can manage to bring the DC-bus voltage back again to 690 V.

Power step: $\mathbf{P_r = 0}$

The last simulation is carried with $P_r = 0$. This is obtained for $s_1 = 0$ assuming a lossless machine. In a simulation that takes into account the copper losses, the rotor excitation needs a bit of power. By looking the previous simulations, it is found that the the condition $P_r = 0$ is obtained at $t = 15.1516s$ in Fig. 5.2 and for $s_1 = -3.6037e^{-3}$ in the slip domain. The corresponding rotor speed is 1003.6037 rpm.

Fig. 5.22 show that the stator power of the first machine, P_{e1}, follows the P_{tot} since it is the only DFIG power contribution when the rotor power is zero. The second machine is turned on as a motor, in order to temporarily compensate from the DC-bus the transients on the first machine rotor power for its instantaneous variation of magnetization. It is possible to observe the DC-bus voltage profile in Fig. 5.23, where the voltage is first charged in order to manage the power from the rotor 1, and then back to the reference value with a slight oscillation.

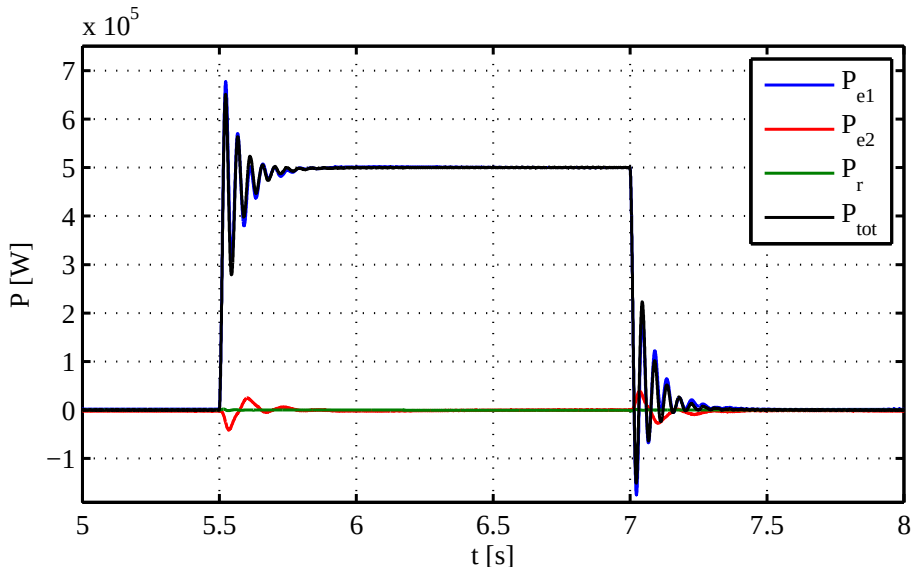

Fig. 5.22: Power-step response of the system in the condition of $P_r = 0$.

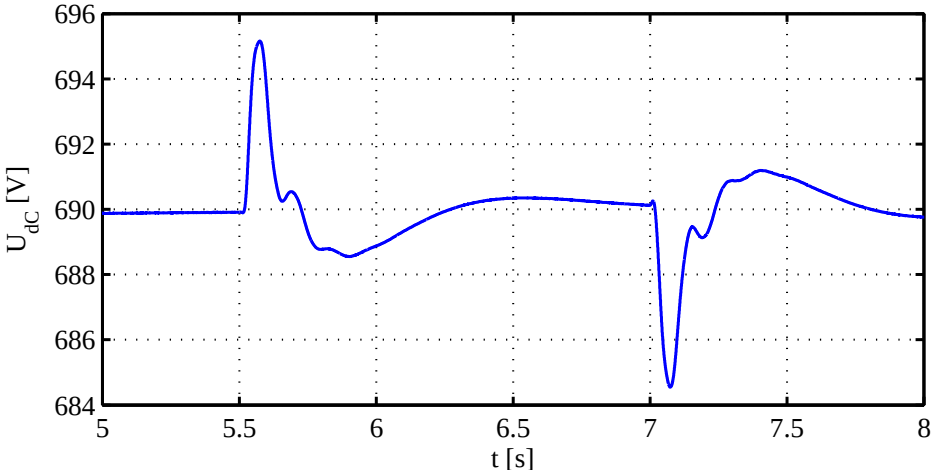

Fig. 5.23: Power-step response of the DC-bus in the condition of $P_r = 0$.

5.3 Conclusions

This chapter dealt with a control strategy suitable for the D-DFIG system. It is shown that the control strategy opereates correctly and allows a good DC-bus voltage control, while providing a good control of the active power delivered to the grid as well. The DFIGs follow the equilibrium operating points for every slip value. The second machine is controlled indirectly through the DC-bus voltage control, and for this reason is responding slightly slower than the first machine, but the total power requested from the grid is always satisfied with a rising time lower than 0.02 s, and a settle time lower than 0.5 s. The system presents some large overshoots and a damped oscillation at 0.05 s. This behaviour can be corrected

by a better tuning of the PI regulators of the control algorithm.

The reactive power control has not been taken in account, but it is an important aspect that should be considered as the reactive power is important when considering the grid connection and the grid codes during fault conditions.

Chapter 6

CONCLUSIONS

This work has dealt with several aspects of a new machine topology for wind power applications, composed by two DFIGs connected on the same shaft and sharing the rotor power through a rotating frequency converter. The topology, called D-DFIG, was shown in [3].

The first part of the work dealt with the analysis of the considerations and the data in [3]. From the voltage balance equations and the definition of active and reactive power, the possible values of rp and s_1^r were found under certain assumptions and constraints found in the paper [3]. In addition, further constraints were imposed in order to meet the practicability of the D-DFIG.

The analysis shows some limits of the D-DFIG configuration. One of the limits is the presence of power loops, either of electrical or mechanical origin. In particular, according to the given definitions of slip for the two machines, when both the slips s_1 and s_2 are positive (sub-synchronous operating mode) the power loops in the machine reach a non negligible value with respect to the available power. Reducing the power loops by design narrows the possible design range of the machine parameters rp and s_1^r. A way to by-pass the problem is to allow a speed range variation such that the sub-synchronous mode is used as little as possible, although this will limit the total speed range of operation of the D-DFIG.

The further evaluation of the power flows through the machine paths (described in Chapter 3) shows that the power flowing through the power electronic is function of of the rp and not only of the maximum slip with respect to the maximum machine power. Naturally, not all possible combinations of rp and s_1^r are acceptable, as some of them bring too high values of rotor power which affects the rating of the power electronics.

Therefore, according to this analysis, it seems that the machine limits defined in [3] are not realistic, but the D-DFIG is still interesting for the possibility of reducing the rating of the power electronics.

In order to further confirm the evaluation of Chapter 3, a dynamic model of the D-DFIG configuration was built, and a control strategy to deal with the active power flow in the grid was proposed. The machine model is built with the software Simulink and the definition of its parts is described in Chapter 4.

The feasibility of the proposed D-DFIG control is confirmed. The strategy uses a FOC in the reference frame of the stator flux linkage for controlling the currents in the two parallel DFIGs. However, only one DFIG receives the power reference, while the second DFIG adjusts automatically its power reference as a consequence of the DC-bus voltage regulation. It is shown that reaching an equilibrium in the DC-bus voltage implies that the correct equilibrium between the two DFIG is reached, and the correct power flow is established.

The DC-bus control is the most problematic part of the control, though, because of the non-linear dynamics involved in the loop. A possible solution applied in this work is the exploitation of a dynamic PI, where the parameters of the PI regulator change as function of the operating point. The DC-bus voltage variation during a speed ramp, as shown in Fig. 5.3 and Fig. 5.13, shows that a more advanced solution might be required.

The analytical power curves are confirmed by the simulations. A small difference occurs when the power flow is substantial. This difference is shown in Fig. 5.8. The reason is not completely clear, but it might be related to the presence of rotor losses.

An efficiency curve was created using different sets of realistic machine parameters.The efficiency curves in the report are sufficiently good for a feasible D-DFIG, although this was true mostly for a configuration with $rp = 2/3$ and $s_1^r = 0.25$. Other configurations might have different efficiency trends, and it could be a topic for future studies. However, an important aspect was that the efficiency was also dependent on the amount of the initial available power reference at cut-in speed P_{cut-in}, becoming higher for higher values of available power.

A last consideration on the D-DFIG regarding the dynamic response to step references in power. The simulations showed that the system is able to respond correctly to a step power reference, although the second machine (the one indirectly controller through the DC-bus voltage regulation) is slower than the first one. The variations of voltage in the DC-bus showed in the simulations must be further investigated, in order to understand whether they could be kept at lower levels with a better control or whether there is something intrinsic in the D-DFIG and the definition of the control.

Overall, the D-DFIG seems to show the advantage of reducing the power electronics rating. Tab. 6.1 shows that a D-DFIG system defined by $rp = 2/3$ and $s_1^r = 0.25$ has a slightly smaller speed range than a conventional DFIG, but that the rating of the power electronics could be as small as 1/3 of that on a conventional DFIG system with maximum slip $s = 0.3$. Considering a reference turbine of 5 MW, this would mean that the rotor power in the conventional DFIG would be 30% of P_n; while in the D-DFIG the rotor power would be 10% of P_n.

Tab. 6.1: Comparison between a D-DFIG and a conventional DFIG, with nominal power $P_n = 5\,MW$.

Value	**Pole pairs**	$\mathbf{N_{min}}$ **[rpm]**	$\mathbf{N_{max}}$ **[rpm]**	$\mathbf{P_n^{converter}}$ **[MW]**
Double DFIG	$p_1 = 3,\ p_2 = 2$	750	1250	0.5
Conventional DFIG	$p = 3$	700	1300	1.5

Chapter 7

FUTURE WORK

Several starting points and ideas for future activities on the D-DFIG configuration are given below.

A D-DFIG transfer function A transfer function of the overall D-DFIG configuration might allow a rapid tuning of the regulators. In this work, the PI were tuned following practical rules explained in [8], but the definition of a transfer function that takes in account the coupling between the machines can be of significant help for the simulation of machines with different parameters.

Differences between the analytical curves and the simulated curves Another interesting aspect is the cause of the differences between the curves in the slip domain computed in Chapter 3 and the curves in the slip domain simulated in 5. This difference is documented in Fig. 5.8 and it increases for high speed and power.

Parametric sensitivity The machine simulation just described in the report is carried out without any variation of the parameters described in Tab. 5.1 and Tab. 5.2. Therefore, the effect of a parametric variation on the D-DFIG and on the control is unknown. An analysis on the parametric sensitivity could be useful.

Control development The control strategy developed in this work addresses only the active power control. An interesting future work could consider the development of a strategy for the reactive power control.

Power and speed references In the main part of the analysis, and in all the simulations, the wind power curve is the one used in [3]. A possible evolution of the model could consider the application of a real wind power curve. The effects of the modification of the synchronous speed (following the considerations in Chapter 3), in order to use different slip region, might be useful to evaluate the overall efficiency of the D-DFIG.

Topology variation *Other combinations of machines and power electronics are certainly possible, limited only by the human imagination.*

REFERENCES

[1] A. SACE, "Technical application papers no.13, wind power plants," ABB SACE, Via Baioni, 35 24123 Bergamo - Italy, Tech. Rep., 2011.

[2] G. Martinelli and A. Morini, *Lezioni di teoria unificata delle macchine elettriche*, 1st ed. Padova, Italy: ServiziGraficiEditoriali, 1992.

[3] N. Kusuno, M. Hori, D. Kawamura, D. Satoh, and M. Kimura, "Investigations into optimum design rules for new brushless doubly-fed induction generator: Rotary converter generation system i," *IEEE*, pp. 1730–1735, mar 2014.

[4] N. U. R. Malik, "Analysis and control aspects of brushless induction machines with rotating power electronic converters," Ph.D. dissertation, Laboratory of Electrical Energy Conversion (E2C), Royal Institute of Technology (KTH), Teknikringen 33, 100 44 Stockholm, SWEDEN, September 2012.

[5] Y.-H. Wan, E. Ela, and K. Orwig, "Development of an equivalent wind plant power-curve," National Renewable Energy Laboratory, Institute of Energy Technology, Tech. Rep., Jun. 2010.

[6] R. Pena, J.C.Clare, and G. M. Asher, "Doubly fed induction generator uising back-to-back pwm converters and its application to variablespeed wind-energy generation," *IEE Puoc.-Electr. Power Applications*, vol. 143, no. 3, pp. 231–241, may 1996.

[7] F. Iov, A. D. Hansen, P. Sørensen, and F. Blaabjerg, "Wind turbine blockset in matlab/simulink general overview and description of the models," Aalborg University, Institute of Energy Technology, Tech. Rep., March 2004.

[8] M. A. Snyder, "Development of simplified models of doubly-fed induction generators (dfig)," Ph.D. dissertation, Department of Energy and Environment, Division of Electric Power Engineering, CHALMERS UNIVERSITY OF TECHNOLOGY, Göteborg, Sweden, 2012.

[9] S. Soter and R. Wegener, "Development of induction machines in wind power technology," in *2007 IEEE International Electric Machines & Drives Conference (IEMDC)*, vol. 2, Antalya, Turkey, May 5-7 2007, pp. 1490–1495.

[10] S. Shao, E. Abdi, F. Barati, and R. McMahon, "Stator-flux-oriented vector control for brushless doubly fed induction generator," *IEEE Trans. Ind. Electron.*, vol. 56, no. 10, pp. 4220–4228, Oct. 2009.

[11] L. Peretti, "Modelling of wind turbines system for complete mechanical and electrical simulations," ABB SECRC, Tech. Rep., november 2011.

[12] J. Jonkman, S. Butterfield, W. Musial, and G. Scott, “Definition of a 5-mw reference wind turbine for offshore system development,” National Renewable Energy Laboratory, Institute of Energy Technology, Tech. Rep., February 2009.

[13] S. Bolognani, “Azionamenti elettrici - azionamenti con motore a induzione,” unpublished.